POLITECNICO DI TORINO

Master's Degree in Energy and Nuclear Engineering

Master's Degree Thesis

Modified point kinetic code for molten salt liquid fuel applied to the Thorizon One reactor

Supervisor
Prof. Sandra DULLA
Tutor
Dr. Giulia RUSSO

Candidate
Andrea VIECELI

November 2025

Abstract

The Molten Salt Reactor (MSR) is a concept whose feasibility was demonstrated in the 1960s with the Molten Salt Reactor Experiment (MSRE), which operated for five years at Oak Ridge National Laboratory (ORNL). Subsequently, research on this type of reactor slowed down due to a lack of investment, but recently interest in MSR has grown, with several startups around the world working on the development of this technology, which is recognised by the Generation IV International Forum (GIF). The aim of this work is to develop in Python a multiphysics code to perform point kinetic calculations and sensitivity analyses of relevant parameters of the Thorizon One reactor. Thorizon One is a cutting-edge MSR concept developed by the startup Thorizon. The developed code couples fuel flow and neutronics to help better understand the behaviour of the Thorizon One reactor in transient scenarios, studying its performance and providing support for reactor optimisation during the design phase. The code was verified by comparing its results with those of high-fidelity models applied to the Molten Salt Fast Reactor (MSFR) concept. The study on the Thorizon One focused primarily on transients due to Reactivity Initiated Accidents (RIA). During this type of transient, a strong negative reactivity feedback is rapidly triggered due to the Doppler effect and salt expansion. The latter acts on the same time scale as the Doppler effect, since salt is assumed to be incompressible, a hypothesis justified by verification of compliance with a criterion. It has been found that reactor power peaks in RIA events are much more pronounced when the initial reactor power level is low. Furthermore, it is important to study reactor behaviour starting from low power levels and subjected to fuel-pump driven transients, such as pump start-up or pump shutdown, which cause a decrease and an increase in power, respectively. Finally, preliminary sensitivity results show that the impact of core length (and therefore the volume of fuel salt contained inside) is significant during RIA.

Table of Contents

List of Figures

List of Tables

Nomenclature

Greek symbols

α	Salt thermal expansion coefficient	[K^{-1}]
α_T	Total feedback coefficient	[pcm K^{-1}]
$\alpha_{r,i}$	Local weighted feedback coefficient	[pcm K^{-1}]
β	Total delayed neutron fraction	[-]
$\tilde{\beta}$	Total effective delayed neutron fraction	[-]
β_i	Delayed neutron fraction for the i-th group	[-]
$\tilde{\beta}_i$	Effective delayed neutron fraction for the i-th group	[-]
β_{circ}	Effective delayed neutron fraction in a circulating fuel system	[-]
Γ	Numerical solution of the considered parameter in the Grid Convergence Analysis	[-]
Γ_{ext}	Extrapolated solution of the considered parameter in the Grid Convergence Analysis	[-]
ε_i	Delayed emissivity for the i-th delayed neutron precursor group	[m^{-3} s^{-1} eV^{-1} sr^{-1}]
ϵ	Relative error	[-]
θ_j^{upwind}	Scalar quantity in the upwind scheme	[-]
κ_T	Isothermal compressibility of the fuel salt	[Pa^{-1}]
λ_i	Decay constant for the i-th delayed neutron precursor group	[s^{-1}]
λ_c	Inverse of core transit time	[s^{-1}]

Λ	Prompt neutron generation time	[s]
ν	Average number of neutrons produced per fission	[-]
ρ	Reactivity	[-]
ρ_0	Reactivity compensation for the drift of delayed neutron precursors	[-]
ρ_E	External provided reactivity	[-]
$\rho_{feedback}$	Reactivity feedback	[-]
Σ	Total macroscopic cross section	[m^{-1}]
Σ_f	Macroscopic fission cross section	[m^{-1}]
Σ_s	Macroscopic scattering cross section	[m^{-1}]
τ_c	Core transit time	[s]
τ_e	External (out-of-core) transit time	[s]
φ	Angular neutron flux density	[m^{-2} s^{-1} eV^{-1} sr^{-1}]
Φ	Scalar neutron flux density	[m^{-2} s^{-1} eV^{-1}]
$\varphi^\dagger$	Adjoint angular neutron flux density	[m^{-2} s^{-1} eV^{-1} sr^{-1}]
ψ	Shape function	[m^{-2} s^{-1} eV^{-1} sr^{-1}]
χ_i	Delayed neutron emission spectrum for the i-th group	[eV^{-1}]
$\chi_{p,i}$	Prompt neutron emission spectrum	[eV^{-1}]
$\vec{\Omega}$	Direction of travel	[-]

Latin symbols

a	Linear coefficient of variation of density with temperature	[K^{-1}]
A	Amplitude function	[-]
$A_{cross,core}$	Core cross sectional area	[m^2]
$A_{cross,HX}$	Heat exchanger cross sectional area	[m^2]
$A_{cross,legs}$	Legs cross sectional area	[m^2]
A_{HX}	Total heat exchanger surface area	[m^2]
AR	Asymptotic range	[-]

b	Observed order of convergence	[-]
c	Speed of sound in the salt	[m s^{-1}]
C_i	Concentration of the i-th delayed neutron precursor group	[m^{-3}]
c_p	Specific heat capacity	[J kg^{-1} K^{-1}]
CR	Convergence ratio	[-]
E	Neutron kinetic energy	[eV]
f_s	Differential scattering probability function	[-]
F	Feedback transfer function	[-]
F_s	Safety factor	[-]
$\hat{F}_{d,i}$	Delayed fission operator for the i-th group	[-]
$\hat{F}_p$	Prompt fission operator	[-]
$\hat{F}_{tot}$	Total fission operator	[-]
GCI	Grid convergence index	[-]
H	Overall transfer function	[-]
$\hat{H}$	Total transport operator	[-]
$\hat{L}$	Leakage operator	[-]
l_d	Mean generation time with delayed neutrons	[s]
l_p	Prompt neutron lifetime	[s]
l_i	Mean lifetime of a delayed neutron for the i-th group	[s]
k_{eff}	Effective multiplication factor	[-]
L_{core}	Core length	[m]
L_{HX}	Heat exchanger length	[m]
L_{legs}	Hot and cold legs length	[m]
$\dot{m}_f$	Fuel salt mass flow rate	[kg s^{-1}]
$\dot{m}_{cool}$	Intermediate salt mass flow rate	[kg s^{-1}]
$\dot{m}^{(r)}_{core,i}$	Fuel salt mass flow rate in the core sub-channel r and sub-cell i	[kg s^{-1}]

$\dot{m}_{core,j}^{(r)}$	Fuel salt mass flow rate in the core sub-channel r and at junction j	[kg s^{-1}]
$\dot{m}_{he,i}$	Fuel salt mass flow rate in the heat exchanger sub-cell i	[kg s^{-1}]
$\dot{m}_{he,j}$	Fuel salt mass flow rate at the heat exchanger junction j	[kg s^{-1}]
$\dot{m}_{HL,i}$	Fuel salt mass flow rate in the hot leg sub-cell i	[kg s^{-1}]
$\dot{m}_{HL,j}$	Fuel salt mass flow rate at the hot leg junction j	[kg s^{-1}]
$\dot{m}_{CL,i}$	Fuel salt mass flow rate in the cold leg sub-cell i	[kg s^{-1}]
$\dot{m}_{CL,j}$	Fuel salt mass flow rate at the cold leg junction j	[kg s^{-1}]
p	Pressure	[Pa]
P	Thermal power	[W]
q_i	Heat power exchanged in the sub-cell i of the heat exchanger	[W]
Q	Thermal energy	[J]
$\vec{r}$	Position vector	[m]
R	Reactor kinetic component	[-]
rho	Fuel salt density	[kg m^{-3}]
rho_0	Reference fuel salt density	[kg m^{-3}]
$rho_{core,i}^{(r)}$	Fuel salt density in the core sub-channel r and sub-cell i	[kg m^{-3}]
$rho_{he,i}$	Fuel salt density in the heat exchanger sub-cell i	[kg m^{-3}]
$rho_{HL,i}$	Fuel salt density in the hot leg sub-cell i	[kg m^{-3}]
$rho_{CL,i}$	Fuel salt density in the cold leg sub-cell i	[kg m^{-3}]
t	Time	[s]
T	Temperature	[K]
$\hat{T}$	Scattering operator	[-]
t_c	Characteristic time	[s]
T_0	Reference salt temperature for density law	[K]

$T_{1/2}$	Half-life	[s]
$\bar{T}_{core}$	Average core temperature	[K]
$T_{cool,inlet}$	Intermediate coolant temperature at the heat exchanger inlet	[K]
$T_{cool,outlet}$	Intermediate coolant temperature at the heat exchanger outlet	[K]
$T_{CL,i}$	Fuel salt temperature in the cold leg sub-cell i	[K]
$T_{CL,j}$	Fuel salt temperature at the cold leg junction j	[K]
$T_{core,i}^{(r)}$	Fuel salt temperature in the core sub-channel r and sub-cell i	[K]
$T_{core,j}^{(r)}$	Fuel salt temperature in the core sub-channel r and at junction j	[K]
$T_{HL,i}$	Fuel salt temperature in the hot leg sub-cell i	[K]
$T_{HL,j}$	Fuel salt temperature at the hot leg junction j	[K]
$T_{he,i}$	Fuel salt temperature in the heat exchanger sub-cell i	[K]
$T_{he,j}$	Fuel salt temperature at the heat exchanger junction j	[K]
$T_{he,inlet}$	Fuel salt temperature at the heat exchanger inlet	[K]
$T_{he,outlet}$	Fuel salt temperature at the heat exchanger outlet	[K]
$T_{ref,i}^{(r)}$	Reference salt temperature in the core sub-channel r and sub-cell i for reactivity feedback calculation	[K]
ΔT_{LM}	Logarithm mean temperature difference	[K]
u_i	Fuel salt velocity in the sub-cell i	[m s^{-1}]
u_j	Fuel salt velocity at the junction j	[m s^{-1}]
$\vec{U}$	Fluid velocity vector	[m s^{-1}]
U_{HX}	Overall heat transfer coefficient	[W m^{-2} K^{-1}]
v	Neutron speed	[m s^{-1}]
$V_{core,i}$	Volume of the core sub-cell i	[m^3]

Chapter 1

Introduction

The growing global demand for energy, combined with concerns about climate change, requires a transition to sustainable, low-carbon energy sources. Among the various options, nuclear energy can be a key component of a diversified and sustainable energy mix. It is an energy source characterised by high reliability and low greenhouse gas emissions. Most current nuclear power plants use Light Water Reactors (LWRs), which, however, have several inherent disadvantages. The water used as a coolant operates at very high pressures (up to 15–16 MPa), resulting in design limitations and structural constraints. The relatively low temperatures that can be achieved limit the thermodynamic efficiency. In addition, new fuel must be added every 1-3 years due to the poor fissile breeding capacity of ^{238}U, and the spent fuel contains plutonium and actinides that require long-term disposal solutions [1].

Research and development on nuclear reactor systems continues, focusing also on Generation IV reactors [2], which aim to ensure greater safety and sustainability than the reactors currently in operation. Among the most promising concepts recognised by the Generation IV International Forum (GIF) is the molten salt reactor, a technology whose feasibility was demonstrated in the 1960s. An 8 MW_{th} molten salt reactor prototype, called the Molten Salt Reactor Experiment (MSRE), was built at Oak Ridge National Laboratory (ORNL) and operated for five years (from 1965 to 1969). However, research on molten salt reactors slowed down in the mid-1970s due to a lack of funding. Current research aims to overcome the

engineering challenges posed by MSR thanks to new technologies developed since the 1960s and new reactor designs [1].

The MSR concept offers several advantages that overcome the limitations of LWRs. Liquid-fuel molten salt reactors are distinguished by the fact that the nuclear fuel is dissolved in a molten salt matrix that circulates in the primary loop, thus performing both the functions of coolant and fuel. Low-pressure operation eliminates the risk of pressure boundary failure and steam or hydrogen explosions. Furthermore, thanks to high operating temperatures, MSR achieve thermodynamic efficiencies of more than 44 % [1].

Despite their various advantages, the unique physical and operational characteristics of these liquid-fuel reactors require dedicated research and modeling. The safety and dynamics analyses of a circulating fuel system require re-evaluation and adaptation compared to traditional systems [1]. This includes understanding the complexity of coupled physical phenomena between neutronics and thermal-hydraulics, particularly during transient and accident conditions. However, accurate simulations are often computationally intensive and require significant time and resources. Therefore, a key aspect also lies in optimizing computational efficiency without compromising accuracy.

1.1 Worldwide Startups on Molten Salt Reactors

In addition to institutions and research centers [3], a growing number of startups are contributing to the development of MSR concepts. This section presents MSR designs of some of these startups, with the aim of providing an overview of the technological context in which the Thorizon One reactor fits. The latter is a concept proposed by the startup Thorizon and analysed in this work.

1.1.1 Stellarium

The Stellarium reactor is a fast molten salt reactor currently being developed by French startup Stellaria, based in Grenoble [4]. The reactor is designed

to provide both electricity and high-temperature steam, and a 250 MW_{th} version is being investigated, along with a scalable concept capable of providing up to 500 MW_{th}. The fuel salt intended for use contains a mixture of uranium, plutonium, thorium, and, optionally, minor actinides. The active region of the core is located at the bottom of the reactor vessel, while a plate heat exchanger is housed at the top. The upper region of the reactor vessel contains neutron-absorbing material to decrease neutron flux and activation of surrounding structures. The flow of fuel salt, driven by natural convection, rises from the center and descends toward the periphery of the reactor vessel, as shown in Figure 1.1. The power delivered by the reactor is directly regulated by the power extracted from the turbine, allowing rapid load following capability [5].

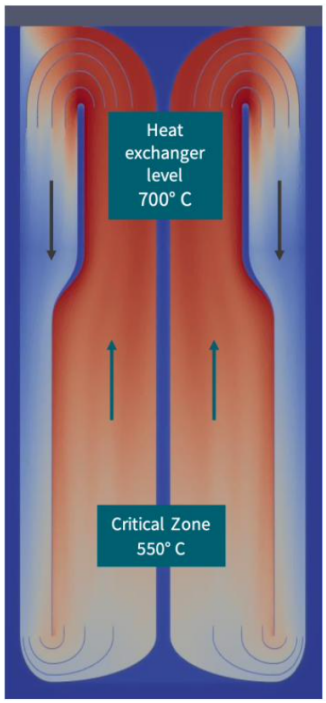

Figure 1.1: Schematic view of the Stellarium reactor vessel [5].

The first safety barrier is the reactor vessel, which is surrounded by a second container and second barrier that, in the event of molten salt leaks, drains the salt into dedicated drain tanks. The reactor building houses several reactor cells, each sealed with a steel cladding, which forms the third barrier.

The reactor building itself serves as the fourth and final containment barrier [5].

The Stellarium design aims at ensuring a homogeneous mixture of fissile and fertile materials in the fuel salt. This aspect results in a nearly constant reactivity throughout the fuel cycle, and allows for long operating periods of up to 20 years without refueling. Although the fuel can be used for at least 20 years, the reactor vessel must be replaced every 10 years. The reactor includes control rods, but relies primarily on passive safety mechanisms such as the negative feedback from the fuel salt temperature [5].

Table 1.1: Characteristics of the Stellarium reactor [5].

Parameter	**Value**
Thermal/electrical capacity, MW_{th}/MW_e	250 MW_{th} (scalable up to 500 MW_{th})
Fuel circuit circulation	Natural convection
Fuel type	Mixture of U, Pu, Th, and minor actinides
Online reprocessing	None
Refuelling Cycle	Up to 20 years without refueling
Vessel replacement cycle	10 years
Reactivity control mechanism	Slow-acting control rods, negative temperature feedback
Fuel cycle	Plutonium and minor actinides burning
Distinguishing features	Natural convection for heat transport
Design status	Finalized conceptual design

1.1.2 XAMR

The XAMR (eXtra small Advanced Modular Reactor) is a fast-spectrum modular reactor with a reference nominal power of 80 MW_{th} [6]. The XAMR, developed by NAAREA in Nanterre, France, is a molten salt reactor fueled and cooled by chloride salts, which aims to burn transuranic elements derived from Uranium Oxide (UOX) and Mixed Oxide (MOX) nuclear fuel cycles. The NAAREA reactor is designed with three (fuel, secondary coolant, and tertiary coolant) salt circuits. The tertiary circuit supplies heat directly to the customer or to a supercritical CO_2 power conversion system, thus enabling the production of heat and/or industrial electricity [5].

Both the core and the reflector are made of silicon carbide composite (SiC-SiC), chosen for its low neutron absorption rate and high resistance to temperature and corrosion. Fuel circulation is based on forced convection, and gaseous and volatile fission products are extracted from the expansion tank of the fuel circuit. The fuel circuit can be drained by a siphon system if necessary, and residual heat then removed from the fuel through two independent circuits, one active and one passive. Reactivity control is based on mechanisms such as rotating control drums and gravity-driven shutdown rods made of enriched boron carbide [5].

Table 1.2: Characteristics of the XAMR reactor [5].

Parameter	**Value**
Thermal/electrical capacity, MW_{th}/MW_e	80 / up to 40 MW_e gross
Fuel circuit circulation	Forced circulation
Fuel type	NaCl-(U,Pu)Cl_3
Online reporcessing	None
Refueling Cycle	3.2 Equivalent Full Power Years
Reactivity control mechanism	Control drums and Shutdown rods
Fuel cycle	Plutonium and minor actinides burning
Distinguishing features	Heat exchanger core
Design status	Basic design

1.1.3 Thorizon One

The Thorizon One reactor is a fast or epithermal molten salt reactor developed by Thorizon, a startup based in Amsterdam and Lyon [7]. The reactor is designed to provide 100 MW_e of base load electricity and high-temperature heat up to 550 C for industrial processes. The Thorizon One concept burns plutonium from light water reactors, while future versions will include uranium breeding capabilities and closed fuel cycles. The fuel salt contains a mixture of NaCl with uranium, thorium, and plutonium chlorides. A key patented feature of Thorizon One is its modular core design, consisting of replaceable cartridges. These cartridges use containment materials that are already qualified for nuclear applications and are replaced during the plant lifetime [8]. Each cartridge is equipped with a pump, a heat exchanger and a plenum gas. The heat generated by the fuel salt is removed by a

secondary salt cooling system, then transferred to a tertiary salt circuit which is connected to thermal storage tanks outside the nuclear island [5].

Under operating conditions, criticality is only reached in the upper region of the cartridges. Without active pumping, passive shutdown occurs due to the gravitational fall of the fuel salt, which leads to subcriticality in the core. The primary system operates at low pressure in all operating modes and hypothetical accident scenarios. The reactor is characterised by a large negative fuel temperature coefficient, which allows for rapid self-regulating power adjustment in response to changes in heat extraction [5].

Table 1.3: Characteristics of the Thorizon One reactor [5].

Parameter	**Value**
Thermal/electrical capacity, MW_{th}/MW_e	250/100
Fuel circuit circulation	Forced circulation
Fuel type	NaCl + (U,Th,Pu)Cl_x
Online reprocessing	None
Refuelling Cycle	Continuous operation for at least 5 years
Design life	5-10 for each cartridge, 60 for the whole plant
Reactivity control mechanism	Control rods adjustment, temperature feedback
Fuel cycle	LWRs spent fuel, depleted U in future breeding scenario's
Distinguishing features	Modular and replaceable core, passive reactor shutdown
Design status	Finalized conceptual design

1.2 Thesis Scope and Outline

The main objectives of this thesis include the development and verification of a Python-based numerical tool and its application to the study of reactor accident scenarios, with particular attention to the Thorizon One molten salt reactor. The code involves the use of revised point kinetic equations for liquid-fuel reactors, coupled with a simplified thermal-hydraulic description. This work aims to investigate the behaviour of the reactor when perturbed and, ultimately, to perform a preliminary sensitivity analysis to identify key parameters that most influence reactor performance.

Chapter 2 will focus on presenting the design and features of the Thorizon

One reactor, highlighting the design advantages of this concept.

Chapter 3 will explain the fundamental principles of reactor physics, covering the distinct behaviours of prompt and delayed neutrons and their essential role in the control and stability of nuclear reactors, together with the key concepts of reactor reactivity and criticality. It will delve into the Point Kinetic Model (PKM), describing its applicability and highlighting the crucial adaptations required for its application to liquid-fuel reactors, then addressing the key approximations that support the developed model. The nature of various dynamic codes developed for the simulation of MSR systems will also be presented and analysed.

Based on the notions introduced in Chapter 3, Chapter 4 will introduce the principles and assumptions underlying the developed model, with particular attention to the architecture and the logic of integration of thermal-hydraulic and neutronic modules. This chapter will present the approaches adopted to analyse reactor dynamics in transient states.

Chapter 5 deals with model verification through solution verification and numerical benchmarking with other simulation codes. The reference reactor will be the MSFR. This chapter introduces the MSFR concept and the parameters used in the simulation model, including fuel compositions and key physical properties. This chapter aims to demonstrate the accuracy, reliability and predictive capability of the developed tool.

Chapter 6 summarizes the results obtained for specific transients in the Thorizon One reactor using the developed code. The main aspects of the reactor will be studied and described, thanks to the system responses such as power excursions and temperature evolution. Chapter 6 will also focus on identifying influential parameters affecting the reactor behaviour during transients.

Chapter 2

The Thorizon One reactor

The Thorizon One reactor [7] is an innovative concept developed by Thorizon, a company based in the Netherlands and France, with headquarters in Amsterdam and Lyon. Thorizon's reactor can be either a fast or epithermal system, as both concepts can be realized using the same technological basis.

A key feature and patented concept of Thorizon One is its modular core design, which consists of multiple replaceable modules, known as cartridges. Each cartridge contains a specific volume of fuel salt, consisting of a mixture of NaCl with uranium, thorium, and plutonium chlorides [5]. These cartridges are designed to be replaced every 5-10 years, using containment materials that are already qualified for nuclear applications [8]. Although conventional molten salt reactors face difficulties in obtaining licenses for reactor materials capable of withstanding more than 60 years of operation under conditions of corrosion, high temperatures, and irradiation, Thorizon's solution is innovative. Dividing the fuel volume into modular cartridges facilitates replacement, as well as the transport and handling of spent molten salt.

The strategy adopted by Thorizon allows for flexible and modular implementation with variable number of modules, ensuring good integration into modern electrical networks [5].

Table 2.1 presents a comparative analysis between molten salt reactors and other nuclear technologies. Although more traditional technologies still

have limitations in terms of safety, waste management, or flexibility, the Thorizon One concept addresses these challenges comprehensively. The technology effectively combines inherent safety, design modularity, and spent fuel recovery. Thorizon's engineering approach has resulted in a project recognised at European level for its excellence and ambition; this motivated me to apply to Thorizon for a thesis project on these topics.

Table 2.1: Competitor analysis of the Thorizon One concept [9].

Criteria	Gen II–III Existing nuclear power plants *(light water)*	Gen III Small modular reactors *(light water)*	Gen IV Liquid metal cooled, solid fuel *(sodium, lead)*	Gen IV High temp. gas cooled *(HTR)*	Gen IV Molten salt reactors *(all variants)*	Thorizon One
Carbon free energy Stable baseload, small energy footprint	✓	✓	✓	✓	✓	✓
Modular design Reduced construction costs, series production	**X**	✓	∼	∼	∼	✓
Industrial use cases High outlet temperature, deliver industrial heat	**X**	**X**	∼	✓	✓	✓
Fuel circularity Valorizing spent fuel and reducing long-lived waste	**X**	**X**	∼	**X**	✓	✓
Low operating pressure Lower risks, lighter construction, lower costs	**X**	**X**	✓	**X**	✓	✓
Inherent safety No escalation, self-regulating capabilities	**X**	**X**	**X**	✓	✓	✓

2.1 Technical overview

The Thorizon One is designed to provide 100 MW_e of base load electricity and high-temperature heat (up to ≈ 550 C) for industrial processes, all while burning plutonium from light water reactors, while future versions will include uranium reproduction capabilities and closed fuel cycles [5].

The reactor core consists of 19 cartridges, located inside a cylindrical cavity of the reactor. The core cavity has a cooling system for all irradiated elements, consisting of a low-pressure CO_2 gas circulation system that dissipates energy through a series of gas/water heat exchangers. This system, together with an emergency core cavity cooling system, is designed to manage decay heat under transient operating conditions and in design basis accident scenarios [5].

The heat generated by the fuel salt inside the cartridges is removed by a secondary salt cooling system. The heat is then transferred to a tertiary salt circuit located outside the nuclear island, connected to thermal storage tanks. Finally, for electricity generation, thermal energy is transferred to water within a steam/water Rankine cycle system [5].

The reference design includes control rods used for reactor startup, shutdown, and normal operation. A sketch of the plant layout is presented in Figure 2.1.

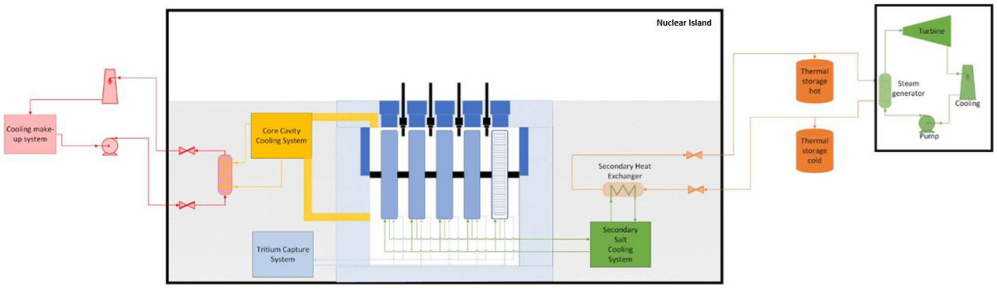

Figure 2.1: Schematic representation of the Thorizon One plant [5].

Each cartridge is equipped with a pump and a heat exchanger located at the bottom, and also includes a plenum gas to manage pressure fluctuations and the accumulation of gaseous and highly volatile fission products. As far as the primary heat exchanger is concerned, shell-tube heat exchangers are

used, with the fuel salt flowing in the shell side and the secondary cooling salt inside the tubes. Each individual cartridge is a closed system without any purification or online refueling system, contrary to other molten salt reactor concepts, such as the Molten Salt Breeder Reactor (MSBR) [10] and the MSFR [11]. In any case, the loss of reactivity associated with the purification process is compensated for by the specific composition of the salt and is limited thanks to the fast spectrum of the reactor [5].

Under operating conditions, criticality is only reached in the upper part of the core due to the circulation of the fuel salt and the arrangement of neutron reflecting and absorbing material [5]. This configuration is shown in Figure 2.2.

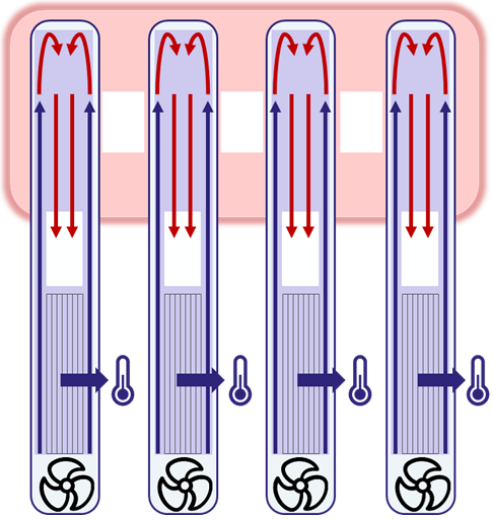

Figure 2.2: Schematic of the reactor core in full operating condition [5].

Without active pumping, passive shutdown occurs by gravity-driven drainage of the fuel salt in the cartridges, and the core becomes subcritical, with the gas pocket inside the cartridge that naturally rises to the top (Figure 2.3).

The primary system consisting of each individual cartridge operates at low pressure, guaranteed by design in all operating phases and in hypothetical accident scenarios, reducing stress on the primary components. Furthermore, the system is characterised by a negative reactivity coefficient for the salt void that enhances safety and contributes to flexibility in load following. In fact, the strong negative feedback from the fuel salt temperature allows for

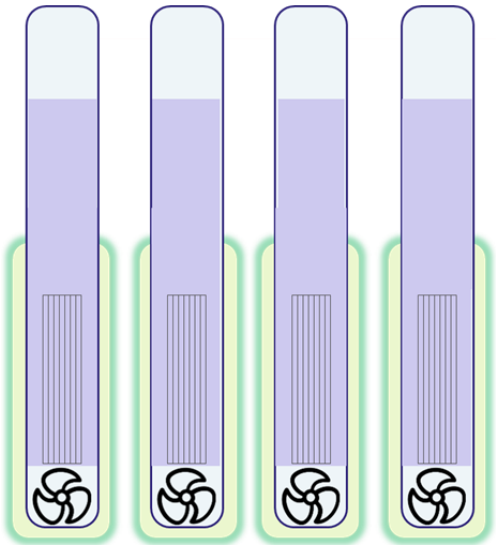

Figure 2.3: Schematic of the reactor core in shutdown conditions with pumps off [5].

rapid self-regulating power adjustment in response to possible variations in heat extraction, ensuring operational flexibility without the need for control rod intervention [5].

Core damage scenarios are mitigated by the synergy of engineered active safety systems, intrinsic passive reactivity control mechanisms, and a secondary containment barrier. These features effectively reduce the probability of off-site release.

Chapter 3

Theoretical foundations and literature review

3.1 Background on Nuclear Reactor Kinetics

The operating principle of a nuclear reactor is based on sustaining a controlled nuclear fission chain reaction. To control this chain reaction, it is necessary to study the equilibrium between the rate of neutron production (primarily from fission) and the rate of neutron loss (due to absorption and leakage from the core). Equilibrium is achieved when the neutron production rate is exactly equal to the removal rate. Under these conditions, the total neutron population and power level remain constant.

Nuclear reactor dynamics, however, includes the study of how the neutron population and related quantities (such as reactivity) change over time (kinetics), along with the factors responsible for this dependence (such as feedback mechanisms) [12]. This topic concerns the study of scenarios in which the reactor deviates from a time-independent configuration. These scenarios are of fundamental importance for analyzing the stability of a reactor, both under normal operating conditions and in abnormal situations. This knowledge is essential for defining appropriate control measures and analyzing reactor characteristics, ultimately ensuring safe operation and good design.

The behaviour of a nuclear reactor is governed by the distribution in space, energy, and time of the neutrons. When a system perturbation occurs, the neutron flux evolves over time, causing corresponding variations in the reactor power. An accurate description of nuclear reactor kinetics is therefore of crucial importance, as it focuses on the transient behaviour of neutron flux and reactor power [13].

This chapter explores the complexities of nuclear reactor kinetics and the models used to study it. The role of prompt and delayed neutrons in sustaining and controlling the fission chain reaction is emphasized. Furthermore, the main similarities and differences between solid-fuel and liquid-fuel reactors are highlighted.

3.1.1 Distinction and importance of prompt and delayed neutrons

It is essential to distinguish between prompt neutrons and delayed neutrons to study the time-dependent behaviour of a nuclear reactor. The former are neutrons that are emitted almost instantaneously after fission, in about 10^{-14} s, while the latter are neutrons generated after a finite time interval that depends on the decay of certain fission fragments known as Delayed Neutron Precursors (DNP) [1]. Delayed neutrons originate in the decay by neutron emission of nuclei produced following the β-decay of the DNP. The decay process is characterised by the half-life $T_{1/2}$, which represents the time interval required for the quantity of the decaying substance to be reduced by half. For reactor kinetic calculations, delayed neutron precursors are divided into several groups, each defined by a specific half-life ranging from a few milliseconds to about 55 s for standard fissile isotopes such as ^{235}U and ^{239}Pu. Each group of DNP has its own decay constant λ_i, which is inversely proportional to the half-life according to the relationship $\lambda = ln(2)/T_{1/2}$ [14].

The difference between the characteristic times of prompt neutrons and delayed neutrons plays a fundamental role in terms of reactor control. If only prompt neutrons were involved, the chain reaction would respond

proportionally to the prompt neutron lifetime, making the reactor uncontrollable. The prompt neutron lifetime is the average time between the generation of a prompt neutron and its absorption, and is of the order of 10^{-4} s for thermal reactors and 10^{-7} s for fast reactors. Delayed neutrons significantly increase the mean generation time, defined as the time between the birth of a neutron and its subsequent absorption leading to another fission. The mean generation time l_d accounts for both prompt and delayed neutrons, and can be expressed, under conditions close to criticality, as [15]:

$$l_d = (1 - \beta)l_p + \sum_i l_i \beta_i \tag{3.1}$$

where l_p is the prompt neutron lifetime, β_i is the fraction of delayed neutrons in the i-th group, β is the total delayed neutron fraction (equal to the sum of all β_i), l_i is the mean lifetime of a delayed neutron in the i-th group, and $(1 - \beta)$ represents the fraction of neutrons emitted promptly. When the contribution of delayed neutrons is included, the mean generation time in a thermal reactor increase to approximately 0.1 s [14].

To accurately reflect the impact of delayed neutrons on reactor dynamics, the key parameter to study is the effective fraction of delayed neutrons ($\tilde{\beta}_i$) for each i-th group. The latter differs from physical fractions since it takes into account the effective role of delayed neutrons in sustaining the chain reaction, which is referred to as 'importance' [14].

In liquid-fuel MSR, the importance of delayed neutrons is altered by the circulating nature of the fuel. Unlike solid-fuel reactors, where delayed neutron precursors remain inside the core until they decay, in liquid-fuel reactors the precursors are transported and can decay outside the core region. This phenomenon is known as 'DNP drift' and has strong implications for the dynamics of MSR. In fact, since some of the delayed neutrons are emitted outside the critical region, DNP drift results in a reduction in the total effective fraction of delayed neutrons $\tilde{\beta}$, defined as the sum of the individual effective fractions for each precursor group $\tilde{\beta}_i$ [1].

DNP drift in circulating fuel reactors creates a strong coupling between neutronics and thermal-hydraulics, as the fuel circulation time in the fuel

circuit directly influences the kinetics. The result is unique dynamic behaviour of these kind of reactors that requires accurate models, especially when describing DNP transport.

3.1.2 Key Kinetic parameters: reactivity and feedback mechanisms

To understand the time-dependent behaviour of the neutron population (and therefore of the reactor), it is necessary to define appropriate kinetic parameters. One of these is the reactivity parameter ρ. Reactivity is related to the effective multiplication factor k_{eff}, which accounts for neutron leakage in a real, finite reactor and is defined as the ratio between the neutron production rate from fission in one generation and the neutron loss rate (absorption and leakage) in the preceding generation [16]:

$$\mathrm{k}_{eff} = \frac{\text{neutron production from fission in one generation}}{\begin{array}{c}\text{neutron absorption in the} \\ \text{preceding generation}\end{array} + \begin{array}{c}\text{neutron leakage in the} \\ \text{preceding generation}\end{array}} \tag{3.2}$$

The condition in which the neutron chain reaction is self-sustaining, with the neutron population remaining constant, is referred to as the critical state, corresponding to $k_{eff} = 1$. Deviations from this value, where k_{eff} is greater or lower than one, correspond to supercritical or subcritical states, respectively [17].

The relationship between reactivity and effective multiplication factor is expressed as [16]:

$$\rho = \frac{k_{eff} - 1}{k_{eff}} \tag{3.3}$$

Reactivity is a measure of the reactor's departure from criticality and is intrinsically dimensionless [1]. However, for practical reasons, reactivity is commonly expressed in various units: $\Delta k/k$, *pcm* (part per hundred thousand), and dollars (\$). By definition, the reactivity value calculated by Equation (3.3) is in units of $\Delta k/k$, representing the relative deviation of the effective multiplication factor from unity [16]. The conversion between

the value in $\Delta k/k$ and *pcm* is:

$$1\ pcm = 0.00001\ \frac{\Delta k}{k}$$

Reactivity can also be expressed in dollars (\$), where one dollar corresponds to the effective delayed neutron fraction, $\$ = \tilde{\beta}$. A reactor that contains one dollar of positive reactivity enters in a prompt criticality regime. Since the prompt critical condition is closely related to the dynamic response of the reactor, the dollar has been defined as a specific unit of reactivity, particularly useful for analyzing this condition.

In this work, reactivity will be expressed in *pcm*, as this is advantageous for quantitative relationships in the framework of the equations used for transient analysis.

The criticality of a reactor is defined exclusively by its intrinsic properties and does not depend on the absolute neutron flux or power level, while the flux distribution must be calculated to verify criticality [18]. Maintaining reactor criticality and regulating power levels require effective reactivity control systems, which are essential elements of any reactor design. In this context, a substantial difference between conventional solid-fuel reactors and liquid-fuel reactors lies in the different nature of the reactivity control mechanisms, which is closely linked to the different phase of the fuel.

Reactivity control strategies differ significantly between conventional solid-fuel reactors and liquid-fuel reactors. In conventional solid-fuel reactors, such as pressurised water reactors (PWRs), the fuel is isolated in fuel elements consisting of uranium dioxide (UO_2) pellets contained in fuel rods, whose cladding is typically made of Zircaloy. The solid fuel and the coolant (usually light water) are therefore physically separated within a heterogeneous assembly. In contrast, molten salt reactors use circulating liquid fuel, where the fuel salt flows through the primary circuit while also acting as a coolant. This fundamental difference in fuel configuration introduces unique dynamics that alter reactivity management and control strategies [17].

In conventional solid-fuel reactors, reactivity control is based on the use

of control rods, along with soluble poisons and burnable poisons. Control rods are movable rods composed of neutron absorber materials, such as boron carbide (B_4C) or hafnium, providing reactivity control for normal adjustments and SCRAM (rapid shutdown). Soluble poisons (typically boric acid) and burnable poisons (such as gadolinium) are used in the coolant and in the fuel, respectively, to compensate for reactivity over time. These control methods are essential during the operating cycle [17]. In this type of reactor, variations in the temperature and density of the fuel and coolant are dictated by the transfer of fission heat from the solid fuel matrix to the nearby coolant. The reactivity feedback provided by the moderator void, due to the latter expanding when the temperature rises, acts in PWRs with a time delay related to the heat transfer that must reach the cooling water acting as a moderator. Since the void coefficient often provides the greatest negative feedback, this thermal inertia delays the insertion of reactivity that mitigates a perturbation.

In a MSR, the presence of circulating fuel introduces unique dynamics that alter reactivity management. A distinctive feature of a liquid-fuel MSR is that delayed neutron precursors are transported in and out of the core by the salt circulation. This results in a reduction of delayed emissions effectiveness because some of the precursors decay in a region that can be outside of the core. The speed with which the fuel salt circulates within the primary circuit affects criticality and can be used for power control. The strategy often involves using control bars only to compensate for the loss of DNP during pump start-up (by inserting positive reactivity) and for DNP accumulation during shutdown (by inserting negative reactivity). These control methods are essential during the operating cycle [17].

Another feature that distinguishes molten salt reactors from conventional reactors is the fact that the fuel is not isolated in fuel elements. The feature of circulating fuel allows for the management and removal of gaseous fission products such as xenon (Xe) and krypton (Kr). This eliminates the complexities associated with the intensive use of soluble poisons and burnable poisons, which are common in solid-fuel reactors.

A peculiar aspect of the control and safety of liquid-fuel molten salt reactors

is related to a strong reactivity feedback mechanism. Figure 3.1 illustrates the feedback mechanism using a block diagram and the formalism of transfer functions in the Laplace domain. Transfer functions are mathematical constructs used in the Laplace domain (s-domain) that convert the time-dependent differential equations governing reactor kinetics into simpler algebraic equations. The total reactivity perturbation is the input for the kinetic equations and consists of the externally imposed reactivity variation ($\delta\rho_{ex}(s)$) and internal reactivity feedback. The reactor's response to the perturbation is represented by the zero-power transfer function ($P_0R(s)$), which defines the resulting power variation ($\delta P(s)$) based on the steady-state power (P_0) and the reactor kinetic component ($R(s)$). The zero-power transfer function represents the purely kinetic behaviour of the reactor, neglecting any feedback effects. The reactor kinetic component $R(s)$ depends exclusively on the properties of prompt and delayed neutrons. The power variation, $\delta P(s)$, is coupled to the reactivity input through the feedback transfer function $F(s)$, which models the internal physical influences on reactivity. Therefore, the dynamic response of the reactor can be represented by the overall transfer function $H(s)$, defined as [12]:

$$H(s) = \frac{\delta P(s)}{\delta\rho_{ex}(s)} = \frac{P_0R(s)}{1 - P_0R(s)F(s)} \tag{3.4}$$

The overall transfer function, $H(s)$, represents the ratio of the Laplace-transformed output (response) to the Laplace-transformed input (perturbation). If the feedback is absent or negligible ($F(s) = 0$ or $P_0 \to 0$), the denominator can be approximated to 1, and the system is governed only by zero-power kinetics. In contrast, if the feedback is active, its interaction with the kinetics closes the loop and determines the stability of the system. The transfer function approach is useful for studying the stability of the dynamic system. Instead of solving the complete set of coupled differential equations, the analysis is simplified and related to the position of the roots (poles) of the characteristic equation, which are derived from the denominator of $H(s)$ set equal to zero.

The strong negative reactivity feedback of MSR concepts is mainly due to:

- Doppler effect: An increase in fuel temperature causes greater movement

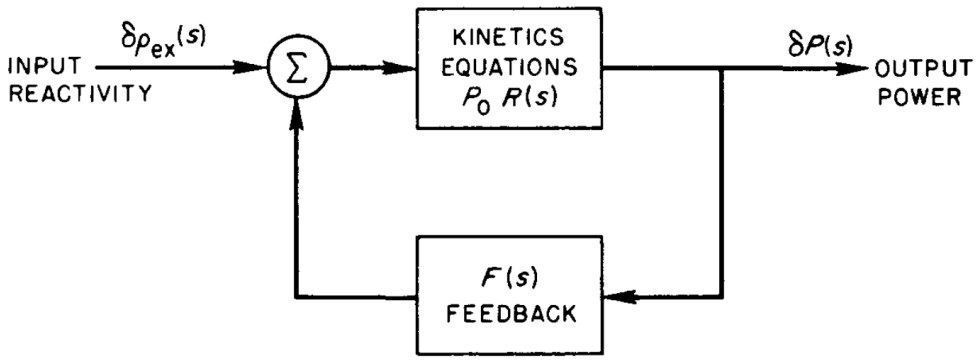

Figure 3.1: Schematic illustration of feedback mechanism in a reactor [12].

of fissile atoms, which broadens and flattens the neutron resonance cross-section curves. This phenomenon, known as Doppler broadening, introduces negative reactivity feedback.

- Density/void feedback: When the fuel salt heats up, it expands, causing its density to decrease. A decrease in fuel density means that there is less fissile material per unit volume, introducing negative reactivity feedback.

A fundamental difference between liquid-fuel reactors and solid-fuel reactors is this: in the former, heating and density variations occur directly in the fuel medium, resulting in strong negative reactivity feedback that plays a key role in ensuring the intrinsic stability of the reactor [17]. Temperature and density variations occur almost instantaneously throughout the medium, with density changes propagating at speeds up to the speed of sound in the salt. Thermal expansion directly changes the fuel density and thus the fissile concentration (increasing neutron leakage) throughout the core immediately upon heating. The high negative reactivity coefficient of the fuel salt temperature is a distinctive feature of these systems. Since heat and density changes occur directly throughout the fuel medium, delays associated with heat transfer from solid fuel elements to a separate coolant, as seen in conventional reactors, are avoided.

3.2 Point Kinetics Model

As discussed earlier, the neutron flux in a nuclear reactor is sensitive to perturbations. These perturbations are not generally uniform in space, but because of the relatively large migration distance and relatively short lifetime of neutrons, local disturbances propagate rapidly [19]. Under certain conditions, particularly if the neutron diffusion length is large and the disturbance is not strong, the time-dependent behaviour of the reactor can be accurately described using a simplified model known as the point kinetics model. This approach allows the evolution of the total reactor power to be predicted assuming that the distribution of neutrons within the core remains unchanged from the initial steady-state distribution and that only the total neutron population changes over time. In other words, the entire reactor core is considered as a single point, ignoring the spatial dependence of the variables [19].

Historically, interest in the use of simplified kinetic models arose because solving full transient problems requires large computational resources. The detailed, deterministic solution of the neutron field involves the Maxwell-Boltzmann neutron transport equation, which is an integral-differential equation with seven independent variables (three spatial, two angular, energy, and time). By ignoring the spatial dependence of the variables, it is possible to reduce the equations governing the system to a set of coupled ordinary differential equations, avoiding the complicated solution of the complete transport equation. Specifically, the system of equations includes an equation for the total number of neutrons in the core (or the reactor power) and separate equations for each group of delayed neutron precursors [1]. For a traditional solid-fuel nuclear reactor with N delayed neutron groups, the point kinetic equations are generally expressed as shown in Equation (3.5) [12].

$$\begin{cases} \dfrac{dP(t)}{dt} = \dfrac{\rho(t) - \tilde{\beta}}{\Lambda} P(t) + \displaystyle\sum_{i=1}^{N} \lambda_i C_i(t) \\ \dfrac{dC_i(t)}{dt} = \dfrac{\tilde{\beta}_i}{\Lambda} P(t) - \lambda_i C_i(t) \quad for \quad i = 1, 2, \ldots, N \end{cases} \tag{3.5}$$

where Λ is the prompt neutron generation time, P is the instantaneous

system power, and C_i is the delayed neutron precursor concentration of group i-th.

Point kinetics is widely used in reactor control due to its simplicity. Reactivity feedback is incorporated into Equation (3.5) thanks to the fact that the reactivity ρ is influenced by the externally applied reactivity, for example from control rods, and the feedback reactivity.

The PKM can be applied to the study of both planned operating transients, such as power adjustments in response to load variations, and potential transients resulting from abnormal or accidental conditions, such as uncontrolled control rod ejection or loss of heat sink. However, its validity is based on the assumption that the spatial distribution of neutron flux remains constant. When this assumption is violated, as in cases involving localized disturbances, such as the asymmetric withdrawal of a single control rod, the application of the PKM becomes less accurate.

3.2.1 Derivation and physical interpretation of the point kinetic equations

The purpose of this section is to review the derivation and interpretation of the point kinetic equations, one of the algorithms developed to deal with time-dependent problems in nuclear reactors. This allows interpretable definitions of reactivity, prompt neutron generation time, and effective delayed neutron fractions to be given. The first step is to derive the conventional form of kinetic equations, for reactors in which the fuel is stationary, from the time-dependent transport equation. Point kinetic equations then represent the simplest approach to the solution of these equations.

The behaviour and distribution in time of neutrons in a solid-fuel reactor is given by the time-dependent neutron balance, which can be expressed in

the following form [20]:

$$\begin{aligned}\frac{1}{\mathrm{v}(E)}\frac{\partial\varphi(\vec{r},\vec{\Omega},E,t)}{\partial t} &= -\vec{\Omega}\cdot\nabla\varphi(\vec{r},\vec{\Omega},E,t) - \Sigma(\vec{r},E,t)\varphi(\vec{r},\vec{\Omega},E,t) \\ &+ \oint d\vec{\Omega}' \int dE'\,\Sigma_s(\vec{r},E'\to E) f_s(\vec{r},\vec{\Omega}'\cdot\vec{\Omega},t)\varphi(\vec{r},\vec{\Omega}',E',t) \\ &+ (1-\beta)\frac{\chi_p(E)}{4\pi}\int dE'\,\nu(\vec{r},E')\Sigma_f(\vec{r},E',t)\Phi(\vec{r},E',t) \\ &+ \sum_{i=1}^{N}\frac{\chi_i(E)}{4\pi}\lambda_i C_i(\vec{r},t)\end{aligned} \tag{3.6}$$

where the notation is described in Table 3.1

Table 3.1: Notation used in the neutron transport equation.

Symbol	**Description**
$\varphi(\vec{r},\vec{\Omega},E,t)$	Angular neutron flux density: neutrons per unit area, time, solid angle, and energy
$\Phi(\vec{r},E,t)$	Scalar neutron flux density: integral of the angular flux density over all solid angles
$\mathrm{v}(E)$	Neutron speed as function of energy
$\Sigma(\vec{r},E,t)$	Total macroscopic cross section: probability of any neutron interaction per unit path length
$\Sigma_s(\vec{r},E'\to E)$	Macroscopic scattering cross section: probability per unit path length that a neutron scattering collision changes the energy from E' to E
$\Sigma_f(\vec{r},E',t)$	Macroscopic fission cross section: probability of fission reaction per unit path length
$f_s(\vec{r},\vec{\Omega}'\cdot\vec{\Omega},t)$	Differential scattering probability function: probability of scattering from direction $\vec{\Omega}'$ to $\vec{\Omega}$
$\nu(\vec{r},E')$	Average number of neutrons produced per fission event
$\chi_p(E)$	Prompt neutron emission spectrum: energy distribution of prompt neutrons released from fission
$\chi_i(E)$	Delayed neutron emission spectrum (group i): energy distribution of delayed neutrons
N	Number of delayed neutron groups

Basically, Equation (3.6) represents the conservation of neutrons within an infinitesimal element of phase space, which refers to an infinitesimal volume within the dimensional space used to describe the state of neutrons. This space includes the position of the neutron, represented by $\vec{r}$, its energy E, the direction of travel $\vec{\Omega}$, and time t.

Each member of Equation (3.6) has a physical meaning. Specifically:

- $\mathrm{v}^{-1}(E)\partial\varphi(\vec{r},\vec{\Omega},E,t)/\partial t$: Represents the time variation of the neutron angular density $n(\vec{r},\vec{\Omega},E,t)$ being $\varphi(\vec{r},\vec{\Omega},E,t) = \mathrm{v}(E)n(\vec{r},\vec{\Omega},E,t)$.
- $\vec{\Omega}\cdot\nabla\varphi(\vec{r},\vec{\Omega},E,t)$: This is the streaming term, which describes the rate of entry and exit of neutrons from a differential volume of phase space, due to their motion without interaction. In particular, it takes into account the variation in the population of neutrons that do not collide and cross the boundaries of the volume element.
- $\Sigma(\vec{r},E,t)\varphi(\vec{r},\vec{\Omega},E,t)$: This term quantifies the rate at which neutrons are removed from a specific infinitesimal volume in phase space due to any type of nuclear interaction.
- $\oint d\vec{\Omega}' \int dE'\Sigma_s(\vec{r},E' \rightarrow E) f_s(\vec{r},\vec{\Omega}'\cdot\vec{\Omega},t)\varphi(\vec{r},\vec{\Omega}',E',t)$: Represents the total neutron production rate at point $\vec{r}$ at time t, with energy E and direction $\vec{\Omega}$, due to scattering interaction from all possible initial energies and directions.
- $(1-\beta)\frac{\chi_p(E)}{4\pi}\int dE'\nu(\vec{r},E')\Sigma_f(\vec{r},E',t)\Phi(\vec{r},E',t)$: It represents the rate of production of prompt neutrons from fission reactions.
- $\sum_{i=1}^{N}\frac{\chi_i(E)}{4\pi}\lambda_i C_i(\vec{r},t)$: Describes the rate of delayed neutron production due to the decay of precursors of all N groups.

The delayed neutron source term ($\sum_{i=1}^{N}\frac{\chi_i(E)}{4\pi}\lambda_i C_i(\vec{r},t)$) in Equation (3.6) is linked to the delayed neutron precursor concentrations (C_i), which evolve via their own differential equations:

$$\begin{aligned}\frac{\partial C_i(\vec{r},t)}{\partial t} &= -\lambda_i C_i(\vec{r},t) \\ &\quad + \beta_i \int dE'\,\nu(\vec{r},E')\Sigma_f(\vec{r},E',t)\Phi(\vec{r},E',t), \qquad i=1,\ldots,N\end{aligned} \tag{3.7}$$

The terms in Equation (3.7) have the following meanings:

- $\partial C_i(\vec{r},t)/\partial t$: Express the rate of change over time of the concentration (or atomic density) of the i-th group of delayed neutron precursors

- $\beta_i \int dE' \nu(\vec{r},E')\Sigma_f(\vec{r},E',t)\Phi(\vec{r},E',t)$: Production rate of precursors from group i due to fissions

- $\lambda_i C_i(\vec{r},t)$: Decay rate of precursors, releasing delayed neutrons

To simplify the notation used so far, it is useful to define the following operators:

Scattering operator $\hat{\mathbf{T}}(\mathbf{t})$

$$\hat{T}(t) = \oint d\vec{\Omega}' \int dE' \Sigma_s(\vec{r},E' \to E) f_s(\vec{r},\vec{\Omega}' \cdot \vec{\Omega},t)\cdot$$

Leakage operator $\hat{\mathbf{L}}(\mathbf{t})$

$$\hat{L}(t) = \vec{\Omega} \cdot \nabla \cdot + \Sigma(\vec{r},E,t)\cdot$$

Prompt fission operator $\hat{\mathbf{F}}_\mathbf{p}(\mathbf{t})$

$$\hat{F}_p(t) = (1-\beta)\frac{\chi_p(E)}{4\pi} \int dE' \nu(\vec{r},E')\Sigma_f(\vec{r},E',t)\cdot$$

Delayed fission operator $\hat{\mathbf{F}}_{\mathbf{di}}(\mathbf{t})$

$$\hat{F}_{di}(t) = \beta_i \frac{\chi_i(E)}{4\pi} \int dE' \nu(\vec{r},E')\Sigma_f(\vec{r},E',t)\cdot$$

Now the complete set of equations for neutron kinetics can be written in compact form as:

$$\begin{cases} \dfrac{1}{\mathrm{v}(E)}\dfrac{\partial \varphi(\vec{r},\vec{\Omega},E,t)}{\partial t} + \hat{L}(t)\varphi(\vec{r},\vec{\Omega},E,t) \\ \quad = \hat{T}(t)\varphi(\vec{r},\vec{\Omega},E,t) + \hat{F}_p(t)\Phi(\vec{r},E,t) + \displaystyle\sum_{i=1}^{N} \varepsilon_i(\vec{r},E,t) \\ \dfrac{\partial \varepsilon_i(\vec{r},E,t)}{\partial t} = -\lambda_i\, \varepsilon_i(\vec{r},E,t) + \hat{F}_{d,i}(t)\Phi(\vec{r},E,t), \quad i = 1,\ldots,N \end{cases} \tag{3.8}$$

where $\varepsilon_i(\vec{r}, E, t)$ is the delayed emissivity, defined as:

$$\varepsilon_i(\vec{r}, E, t) = \frac{\chi_i(E)}{4\pi}\lambda_i C_i(\vec{r}, t)$$

To convert Equation (3.8) into a more tractable form, the angular flux of neutrons $\varphi(\vec{r}, \vec{\Omega}, E, t)$ is factorised into a time-dependent amplitude function, $A(t)$, and a phase space function, $\psi(\vec{r}, \vec{\Omega}, E; t)$, traditionally referred to as shape function. The factorisation is valid with infinite forms for shape and amplitude functions. The primary physical justification for this mathematical process is that in many practical reactor transients, the spatial, angular, and energy distribution of neutrons (namely, the shape of the flux) changes relatively slowly compared to the overall neutron population (namely, the amplitude). This allows most of the time dependent phenomena to be captured by $A(t)$, while $\psi(\vec{r}, \vec{\Omega}, E; t)$ is treated as time-independent or as a slowly varying function (expressed by the semi-colon before the time variable).

Thanks to factorisation, it is possible to rewrite the system of equations (3.8) as:

$$\begin{cases} A(t)\dfrac{1}{\mathrm{v}}\dfrac{\partial\psi(\vec{r}, \vec{\Omega}, E; t)}{\partial t} + \psi(\vec{r}, \vec{\Omega}, E; t)\dfrac{1}{\mathrm{v}}\dfrac{dA(t)}{dt} + A(t)\hat{L}(t)\psi(\vec{r}, \vec{\Omega}, E; t) \\ \quad = A(t)\hat{T}(t)\psi(\vec{r}, \vec{\Omega}, E; t) + A(t)\hat{F}_p(t)\Psi(\vec{r}, E; t) + \displaystyle\sum_{i=1}^{N}\varepsilon_i(\vec{r}, E, t) \\ \dfrac{\partial\varepsilon_i(\vec{r}, E, t)}{\partial t} = -\lambda_i\,\varepsilon_i(\vec{r}, E, t) + A(t)\hat{F}_{d,i}(t)\Psi(\vec{r}, E; t), \quad i = 1, \ldots, N \end{cases} \tag{3.9}$$

Equation (3.9) expresses the equilibrium problem to be solved in order to obtain information on the evolution of the shape over time, but with the amplitude unknown.

To obtain a model for the amplitude function, an additional step is required. First, a reference reactor in steady-state conditions (denoted by the subscript '0') is considered, which corresponds to the initial critical configuration of the reactor before any perturbation occurs. The neutron balance in this

configuration can be written as:

$$\hat{L}_0\varphi_0(\vec{r},\vec{\Omega},E) = \hat{T}_0\varphi_0(\vec{r},\vec{\Omega},E) + \frac{1}{k_{\text{eff}}}\hat{F}_{tot,0}\Phi_0(\vec{r},E) \tag{3.10}$$

where $\hat{F}_{tot}$ is the total fission operator defined as:

$$\hat{F}_{tot} = \hat{F}_p + \sum_{i=1}^{N}\hat{F}_{d,i}$$

Since the reference reactor is critical, $k_{eff} = 1$, it is possible to re-write Equation (3.10) as:

$$\left(-\hat{L}_0 + \hat{T}_0 + \hat{F}_{tot,0}\right)\varphi_0(\vec{r},\vec{\Omega},E) = \hat{H}_0\varphi_0(\vec{r},\vec{\Omega},E) = 0 \tag{3.11}$$

where $\hat{H}_0$ is the total transport operator. Then, the fundamental step in the derivation relies in the weighted integration process, in which the multidimensional neutron balance equation is projected onto a selected weighting function. The weighting function is the adjoint angular flux of neutrons $\varphi_0^\dagger$, which can be demonstrated to be mathematically equivalent to the importance function. This feature provides physical meaning to the weighted integration process. In this process, the neutron balance equation is multiplied by the adjoint flux and integrated over the entire phase space (volume, energy, angle). The result is a time-dependent amplitude weighted according to the significance of neutrons at different points in phase space.

The weighting integration process is applied to Equation (3.9), so that it is possible to write:

$$\begin{cases} A(t)\langle\varphi_0^\dagger|\frac{1}{\mathrm{v}}\frac{\partial\psi(t)}{\partial t}\rangle + \langle\varphi_0^\dagger|\frac{1}{\mathrm{v}}\psi(t)\rangle\frac{dA(t)}{dt} + A(t)\langle\varphi_0^\dagger|\hat{L}(t)\psi(t)\rangle \\ \quad = A(t)\langle\varphi_0^\dagger|\hat{T}(t)\psi(t)\rangle + A(t)\langle\varphi_0^\dagger|\hat{F}_p(t)\Psi(t)\rangle + \sum_{i=1}^{N}\langle\varphi_0^\dagger|\varepsilon_i(t)\rangle \\ \langle\varphi_0^\dagger|\frac{\partial\varepsilon_i(t)}{\partial t}\rangle = -\lambda_i\langle\varphi_0^\dagger|\varepsilon_i(t)\rangle + A(t)\langle\varphi_0^\dagger|\hat{F}_{d,i}(t)\Psi(t)\rangle, \quad i = 1,\ldots,N \end{cases} \tag{3.12}$$

where $\langle\varphi_0^\dagger|\cdot\rangle$ indicates integration over phase space and projection onto the adjoint angular flux $\varphi_0^\dagger$. Considering the adjoint angular flux $\varphi_0^\dagger$ constant

in time:

$$\langle\varphi_0^\dagger|\frac{1}{\mathrm{v}}\frac{\partial\psi(t)}{\partial t}\rangle = \frac{\partial}{\partial t}\langle\varphi_0^\dagger|\frac{1}{\mathrm{v}}\psi(t)\rangle \tag{3.13}$$

By setting Equation (3.13) equal to zero, the factorisation of the neutron angular flux $\varphi(\vec{r},\vec{\Omega},E,t)$ becomes unique and the corresponding term appearing in Equation (3.12) can be eliminated.

At this point, dividing all the terms of Equation (3.12) by $\left\langle\varphi_0^\dagger,\hat{F}_{tot,0}\psi\right\rangle$ leads to the form:

$$\begin{cases}\dfrac{\langle\varphi_0^\dagger|\frac{1}{\mathrm{v}}\psi(t)\rangle}{\langle\varphi_0^\dagger|\hat{F}_{tot,0}\psi\rangle}\dfrac{dA(t)}{dt} = \dfrac{\langle\varphi_0^\dagger|(\hat{T}(t)-\hat{L}(t)+\hat{F}_{tot}(t))\psi(t)\rangle}{\langle\varphi_0^\dagger|\hat{F}_{tot,0}\psi\rangle}A(t)+\displaystyle\sum_{i=1}^{N}\frac{\langle\varphi_0^\dagger|\varepsilon_i(t)\rangle}{\langle\varphi_0^\dagger|\hat{F}_{tot,0}\psi\rangle} \\ \dfrac{\partial}{\partial t}\dfrac{\langle\varphi_0^\dagger|\varepsilon_i(t)\rangle}{\langle\varphi_0^\dagger|\hat{F}_{tot,0}\psi\rangle} = -\lambda_i\dfrac{\langle\varphi_0^\dagger|\varepsilon_i(t)\rangle}{\langle\varphi_0^\dagger|\hat{F}_{tot,0}\psi\rangle}+\dfrac{\langle\varphi_0^\dagger|\hat{F}_{d,i}\Psi(t)\rangle}{\langle\varphi_0^\dagger|\hat{F}_{tot,0}\psi\rangle}A(t), \quad i=1,\dots,N\end{cases} \tag{3.14}$$

The term $\left\langle\varphi_0^\dagger,\hat{F}_{tot,0}\psi\right\rangle$ can be physically interpreted as the importance of fission neutrons distributed according to the shape ψ. It acts as a normalisation factor and provides a physical interpretation for the following kinetic parameters:

Effective generation time of prompt neutrons $\boldsymbol{\Lambda}$

$$\Lambda(t) = \frac{\left\langle\varphi_0^\dagger,\frac{1}{\mathrm{v}}\psi(t)\right\rangle}{\left\langle\varphi_0^\dagger,\hat{F}_{tot,0}\psi\right\rangle}$$

This parameter provides essential information on the time scale of the reactor's response when a perturbation is introduced.

Effective delayed neutron fraction $\boldsymbol{\tilde{\beta}_i}$

$$\tilde{\beta}_i(t) = \frac{\left\langle\varphi_0^\dagger,\hat{F}_{d,i}\Psi(t)\right\rangle}{\left\langle\varphi_0^\dagger,\hat{F}_{tot,0}\psi\right\rangle}$$

This parameter represents the importance-weighted contribution of delayed neutrons from group i-th to the total fission neutron production.

Effective delayed neutron emission $\boldsymbol{\tilde{C}_i}$

$$\tilde{C}_i(t) = \frac{\langle\varphi_0^\dagger|\varepsilon_i(t)\rangle}{\langle\varphi_0^\dagger|\frac{1}{\mathrm{v}}\psi(t)\rangle}$$

This parameter appears in the amplitude equations and governs the coupling between the neutron population and the precursor concentrations during transients.

Reactivity ρ

Noting that $\hat{T}(t) - \hat{L}(t) + \hat{F}_p(t) = \hat{H}(t) - \sum_i \hat{F}_{d,i}(t)$, the reactivity term ρ can be defined as:

$$\rho(t) = \frac{\langle \varphi_0^\dagger | \hat{H}(t)\psi(t) \rangle}{\langle \varphi_0^\dagger | \hat{F}_{tot,0}\psi \rangle}$$

The sign and magnitude of the reactivity, particularly in relation to the effective delayed neutron fraction $\tilde{\beta}$, are fundamental in understanding the time-dependent behaviour of the reactor.

The definition of these kinetic terms leads to the standard formulation of the amplitude equations written as:

$$\begin{cases} \dfrac{dA(t)}{dt} = \dfrac{\rho(t) - \bar{\beta}(t)}{\Lambda(t)} A(t) + \displaystyle\sum_{i=1}^{R} \lambda_i \tilde{C}_i(t) \\ \dfrac{\partial}{\partial t}\tilde{C}_i(t) = -\lambda_i \tilde{C}_i(t) + \dfrac{\bar{\beta}_i(t)}{\Lambda(t)} A(t), \quad i = 1, \ldots, N \end{cases} \tag{3.15}$$

The amplitude equations can be solved once the kinetic parameters are known, but these depend on the shape ψ, which in turn evolves over time.

The PKM represents the simplest approach to the solution of the non-linearly coupled amplitude equations (3.15) and shape equations (3.9). The fundamental assumption is to assume that the shape function does not evolve during the transient and corresponds to that of the initial state of the system, i.e. $\psi(\vec{r}, \vec{\Omega}, E; t) \approx \psi(\vec{r}, \vec{\Omega}, E; t = 0)$. This assumption is equivalent to saying that the entire temporal dynamic is captured by the amplitude function $A(t)$, which describes the evolution of the overall power level. Since the shape function ψ remains constant over time, it is possible to define all kinetic parameters, and Equation (3.15) reduces to the point kinetic equations shown in Equation (3.5), a set of solvable ordinary differential equations.

3.2.2 Point kinetics formulations for Liquid-Fuel reactors

The traditional point kinetic model, described by Equation (3.5), assumes a fixed value for the effective fraction of delayed neutrons ($\tilde{\beta}$) and does not take into account DNP movement, making it unsuitable for circulating fuel reactors. This subsection introduces various methods based on the traditional PKM and used for research studies on liquid-fuel reactors.

- **Corrected Point Kinetics:** Corrected Point Kinetics (CPK) is a simple approach in which conventional PKM equations (3.5) are solved with a fixed corrected $\tilde{\beta}$ to account for DNP displacement. This method can predict the final results, but is inadequate to represent the overall behaviour of transients and the effects of the circulation [21].

- **"I" Point Kinetics:** "I" Point Kinetics (IPK) methods use a fixed mesh for neutron calculations and a moving mesh to track the movement of DNP and fluid properties [21]. The approach allows precursors to be tracked during a transient, with fuel salt circulation modeled via the moving cells according to a piston motion. In this scheme, the variables of the moving cells are projected onto the cells of the fixed grid and, after solving the point kinetic equations, the variables of the moving grid are updated based on the fixed cells [22].

- **Decay Point Reactor Kinetics:** Decay Point Reactor Kinetics (DPK) models use source and sink terms added to the precursor balance equations to account for the flow of precursors leaving the core and returning to it through the external circuit [21]. The resulting system of coupled equations for the reactor power ($P(t)$) and precursors of group i ($C_i(t)$) can be expressed as:

$$\begin{cases} \dfrac{dP(t)}{dt} = \dfrac{\rho(t) - \tilde{\beta}}{\Lambda} P(t) + \displaystyle\sum_{i=1}^{N} \lambda_i C_i(t) \\ \dfrac{dC_i(t)}{dt} = \dfrac{\tilde{\beta}_i}{\Lambda} P(t) - \lambda_i C_i(t) - \lambda_c C_i(t) \\ \qquad\qquad + \lambda_c C_i(t - \tau_e) e^{-\lambda_i \tau_e} \quad for \quad i = 1, 2, \ldots, N \end{cases} \tag{3.16}$$

In Equation (3.16), the treatment of the precursor concentrations differs from the classical approach for solid-fuel reactors (Equation (3.5)) by incorporating two additional terms on the right-hand side of the precursor balance equation [23]. These terms capture the dynamic effects inherent in circulating fuel reactors:

- Core Leakage: The term $-\lambda_c C_i(t)$ represents the rate at which precursors of group i leave the core region due to the continuous flow of fuel. λ_c is defined as the inverse of the core transit time (which can be denoted as τ_c), which is the characteristic time a fluid element spends inside the core (calculated as L_{core}/u, where L_{core} is the height of the core and u is the velocity of the fuel).
- Return to the core: The term $+\lambda_c C_i(t-\tau_e)e^{-\lambda_i \tau_e}$ quantifies the rate at which precursors of group i re-enter the reactor core after circulating through the external-core region, with τ_e representing the external-core transit time. The exponential factor $e^{-\lambda_i \tau_e}$ accounts for the probability of precursors surviving radioactive decay (λ_i) during the time that they spend outside the active region. This term recognizes that only precursors that had left the core at time $(t-\tau_e)$ and survived during circulation can contribute as a source to the DNP balance.

These extended point-based kinetic models provide a more physically accurate representation of the role of delayed neutrons specific to liquid-fuel reactors, which is essential for reliable transient analysis and reactor design optimisation. The code developed in this work implements a DPK-based approach for the neutronic module.

3.3 Dynamic codes for molten salt reactors

Computational tools developed during academic research or in research centers have already been used for dynamic simulations focused on MSR concepts. Although these codes share the goal of showing the dynamics of the reactors analyzed and conducting a preliminary safety assessment, it should be noted that they often differ in the approaches implemented.

The suitability of a given code for a given task is a case-by-case evaluation, taking into account computational costs and the nature of the transients to be modeled [21].

Below, a classification based on the level of detail and complexity of the physics incorporated in these codes:

- **Simplified or Lumped-Parameter Models:** These tools are based on PKM approximations and one-dimensional (1D) spatial thermal-hydraulic description. They generally require short computation times, making them suitable for preliminary analyses and parametric studies.
- **Comprehensive Multiphysics Codes:** These codes are based on multidimensional spatial analyses (2D or 3D), combining detailed thermal-hydraulic description with advanced neutronic models. They are designed for careful analysis of transients, some including fuel compressibility.

In order to provide a more detailed overview of some of these codes and to justify the choices made during the development of the code for the Thorizon One reactor, some computational tools found in the literature are now summarized.

Cinsf1D

The Cinsf1D code, developed by D. Lecarpentier and V. Carpentier at Electricité de France (EdF) Research and Development, uses a two-energy-group diffusion model in an axial spatial dimension and takes into account six groups of delayed neutron precursors. The circulation of delayed neutrons required the development of a numerical scheme that implements the discretisation of the finite difference method, the stability of which has been verified. The neutron equations are coupled with those governing axial thermal-hydraulics to take into account thermal feedback effects, which are considered using effective cross sections calculated at numerous reference points. Specifics of the code and the governing equations can be found in [24].

MOSAICS

The MOSAICS (MOlten SAlt Incompressible Calculation System) code was developed during a CEA (Commissariat à l'énergie atomique et aux énergies alternatives) PhD. This tool uses an MPK model, applied locally with precursor tracking through spatial discretisation of the system. The code integrates a 1D thermal-hydraulic model, which extends to multi-1D in the core, assuming a dilatable and incompressible flow. The core is discretized with parallel axial channels without mass exchange between them. Reactivity feedbacks are calculated by summing the weighted cell-by-cell feedback contributions. Further details on the code are provided in [25].

LiCore

The LiCore tool was developed during Axel Laureau's doctoral thesis, where it was originally called CPZ (Cinétique Point par Zone) [11, 26]. Thermal-hydraulics is solved using a Lagrangian method, which means that the cells follow a defined fluid volume in the fuel circuit. The cells move along the modeled circuit (fuel or intermediate) and their volume varies when the salt is heated or cooled. The flow in the various circuits is 1D uniaxial, and the critical region features a radial mesh, i.e., multi-1D with parallel channels. Compressibility is not modeled in this calculation tool. Neutronics is modeled by solving modified point kinetic equations to account for DNP transport and residual power in the moving meshes. Reactivity feedbacks are calculated by summing the cell-by-cell weighted feedback contributions. LiCore has been verified by comparison with the TFM-OpenFOAM approach. A complete description of the code and the main equations is given in [11, 26].

DYN3D-MSR

Developed by the Forschungszentrum Rossendorf (FZR), DYN3D-MSR is a spatial dynamics code for graphite-moderated channel type MSR based on the internal DYN3D code for light water reactors. This computational tool allows transients simulation by 3D neutronics and parallel channels thermal-hydraulics. The model solves the neutron diffusion equation for two

energy groups and an arbitrary number of delayed neutron precursor groups. The code validation was performed mainly on experimental data from the MSRE experiment conducted at Oak Ridge National Laboratory. The code can simulate transients in which space-dependent effects are relevant, such as local obstructions of fuel channels. Further information on the code can be found in [27].

TFM-OpenFOAM

The TFM-OpenFOAM approach is a computational tool based on an innovative approach to kinetic calculations called Transient Fission Matrix (TFM) and on the OpenFOAM code for the thermal-hydraulic solution. The goal is to accurately solve coupled multiphysics calculations with reduced computation times. The thermal-hydraulics module can use an RANS (Reynolds Average Navier-Stokes [28]) approach or an LES (Large Eddy Simulation [28]) approach paying attention to turbulence phenomena. The TFM is based on a matrix resolution of neutron dynamics equations obtained from stochastic neutron calculations (MCNP, SERPENT), allowing the characterization of the entire spatial and temporal response of reactor neutrons. The fission matrices are precalculated for distinct values of temperature and density and interpolated to take into account the impact of temperature variations and therefore, reactivity feedback. Since it is not necessary to recalculate the matrices during the transient, a relatively rapid neutron resolution is obtained before the thermal-hydraulic calculations. The TFM-OpenFOAM tool allows the behaviour of a reactor in steady-state or transient conditions to be modeled with an accuracy close to that of reference Monte Carlo calculations. This approach is described in detail in [11].

Table 3.2 shows a comparison of the dynamic codes presented, highlighting their physical approaches, thermal-hydraulic models, and integrated feedback mechanisms.

Table 3.2: Overview of dynamic codes presented.

Code	**Neutronics**	**Thermal-hydraulics**	**Reactivity Feedback**
Cinsf1D	1D diffusion equation	Incompressible 1D	Temperature-dependent cross-sections
MOSAICS	Improved point kinetics (DPK)	Incompressible 1D (multi-1D core)	Sum of weighted cell-by-cell feedback
LiCore	Improved point kinetics (IPK)	Incompressible Piston 1D (multi-1D core)	Sum of weighted cell-by-cell feedback
DYN3D-MSR	3D diffusion equation	Incompressible 1D	Temperature-dependent cross-sections
TFM	TFM (fission matrices)	Incompressible, RANS/LES	Fission matrix interpolation

Chapter 4

Multi-Physics Modeling of Liquid-Fuel reactors

As introduced in the previous chapters, analysis of any circulating fuel system involves a strong coupling between neutronics and thermal-hydraulics, since variations in fluid properties and flow directly influence neutronics and vice versa. The codes used in this context must therefore capture the behaviour of the fuel salt in each region of the system through which it flows.

Taking inspiration from the tools summarized in Table 3.2, the objective is to develop a Python-based code that allows rapid kinetics studies of the Thorizon One reactor presented in Section 2. The developed model was implemented by combining some of the main features of the MOSAICS and LiCore codes. Specifically, a DPK module, based on the equations introduced in subsection 3.2.2, is coupled with a simplified thermal-hydraulics description that focuses on the energy balance in the molten fuel salt.

The flow of the primary circuit outside the core is modeled as unidirectional, while for the critical zone it is possible to choose whether to consider it as a single channel or divide it into radial meshes considering parallel channels without heat and mass transfer between them.

The flow is assumed to be dilatable but incompressible. This means that although the density of the fluid varies due to temperature changes, it is

assumed that the density does not change in relation to pressure. As a result, the model does not take into account the pressure distribution in the primary circuit and phenomena such as pressure wave propagation.

The thermal-hydraulic module is based on the finite volume method, with discretisation of the flow domain using a staggered grid [28]. The staggered grid allows vector quantities (such as velocity or mass flow rate) to be defined at the interfaces of the discretized volumes, indexed as $j-1$, j, and $j+1$ in the interpretive Figure 4.1. This feature ensures robustness and stability for the calculation of enthalpy flows for the energy balance Equations (4.2)-(4.6).

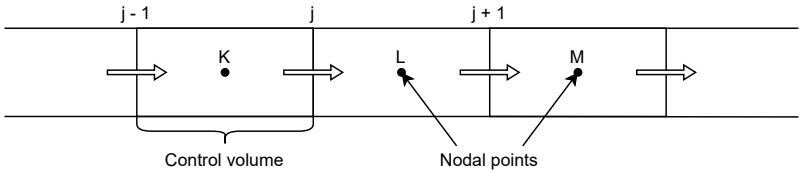

Figure 4.1: Schematic diagram of the staggered mesh.

The velocity of the molten salt fuel within each subvolume is defined as the arithmetic mean of the velocities at the corresponding upstream and downstream interfaces. Referring to Figure 4.1, this can be expressed as:

$$u_K = \frac{u_{j-1} + u_j}{2} \tag{4.1}$$

The ratio between the geometric length of the cell and the velocity of the fluid within it defines the transit time for each individual cell. By summing the transit times of the sub-cells of a component, the transit time of the fuel along the out-of-core region τ_e and along the core $\tau_c = 1/\lambda_c$ is finally calculated. These are key parameters used to describe the drift of precursors, as shown in Equation (3.16).

The components included in the modeled primary loop are shown in Figure 4.2. In particular, these components include a reactor core, an expansion vessel, a primary heat exchanger, and connecting pipes, subsequently referred to as the 'Hot Leg (HL)' for the connection from the core to the heat exchanger inlet and the 'Cold Leg (CL)' for the return path. The system

described above is assumed to be thermally isolated from the environment, and structural thermal expansion is not considered in the current model. Although these assumptions facilitate implementation, it is recognised that they may compromise accuracy and that subsequent improvements to the code are necessary.

4.1 Temperature Equation (mass transport, energy balance)

The equation governing the temperature of the salt is established by means of an energy balance on each subvolume. Assuming that the effect due to the movement of the salt is predominant, heat diffusion along the axis is ignored. Specifically, the temperature equation describes the transport of energy within the fuel, taking into account the net convective contribution entering and leaving the control volume, and normalizing with respect to the thermal capacity of the fluid contained in the volume itself. In the case of a subvolume i of the core, the resulting equation takes the following form:

$$\begin{aligned}\frac{dT_{core,i}^{(r)}}{dt} = &\frac{P_i^{(r)}}{c_p \cdot rho_{core,i}^{(r)} \cdot V_{core,i}^{(r)}} \\ &+ \frac{\dot{m}_{core,j}^{(r)} \cdot T_{core,j}^{(r)} - \dot{m}_{core,j+1}^{(r)} \cdot T_{core,j+1}^{(r)}}{rho_{core,i}^{(r)} \cdot V_{core,i}^{(r)}}\end{aligned} \tag{4.2}$$

In Equation (4.2), c_p denotes a constant specific heat capacity of the fuel salt, $V_{core,i}^{(r)}$ is the volume of the discretized cell, and $rho_{core,i}^{(r)}$ is the density of the fuel salt contained in the subvolume. The terms $m_{core,j}^{(r)}$ and $T_{core,j}^{(r)}$ denote the mass flow rate and salt temperature at the interface of the subvolumes, respectively. The subscripts i and j are used to express the i-th finite volume and the j-th interface, respectively. The superscript (r) indicates the discretisation of the core in the radial direction, if used.

The interface temperatures appearing in (4.2) are discretized using a first-order upwind scheme. The first-order upwind method, often referred to as the "donor cell" method, is a numerical discretisation technique widely used in Computational Fluid Dynamics (CFD). The scheme takes into account

the direction of flow in determining the value on a cell face: the conveyed value of the property transported on a cell face is considered equal to the value at the upstream node [28]. Referring to Figure 4.1, the scalar quantity θ_j^{upwind} calculated at interface j is defined as:

$$\theta_j^{\text{upwind}} = \begin{cases} \theta_K & \text{if } u_j > 0 \\ \theta_L & \text{if } u_j < 0 \end{cases} \tag{4.3}$$

where u_j is the velocity at the interface j. This approach reproduces the directional preference of information transport in fluid flows, ensuring monotonicity and preventing non-physical oscillations that could be generated by higher-order linear schemes. According to Godunov's theorem, no linear advection scheme exists that is both higher than first-order accurate and monotone. However, first-order upwind schemes are known to introduce numerical diffusion that can dampen the solution. Despite this limitation, first-order upwind schemes are standard in many nuclear thermal-hydraulic codes [29, 30], such as RELAP5 [31] and CATHARE [32].

With reference to the other components of the primary circuit shown in Figure 4.2, the respective conservation equations are:

$$\frac{dT_{HL,i}}{dt} = \begin{cases} \dfrac{\dot{m}_{HL,j} \cdot T_{HL,j} - \dot{m}_{HL,j+1} \cdot T_{HL,j+1} - ET}{rho_{HL,i} \cdot V_{HL,i}} & \text{if } i = \frac{n}{2} - 1 \\ \dfrac{\dot{m}_{HL,j} \cdot T_{HL,j} - \dot{m}_{HL,j+1} \cdot T_{HL,j+1}}{rho_{HL,i} \cdot V_{HL,i}} & \forall\ i \neq \frac{n}{2} - 1 \end{cases} \tag{4.4}$$

$$\frac{dT_{he,i}}{dt} = \frac{\dot{m}_{he,j} \cdot T_{he,j} - \dot{m}_{he,j+1} \cdot T_{he,j+1}}{rho_{he,i} \cdot V_{he,i}} - \frac{q_i}{c_p \cdot rho_{he,i} \cdot V_{he,i}} \tag{4.5}$$

$$\frac{dT_{CL,i}}{dt} = \frac{\dot{m}_{CL,j} \cdot T_{CL,j} - \dot{m}_{CL,j+1} \cdot T_{CL,j+1}}{rho_{CL,i} \cdot V_{CL,i}} \tag{4.6}$$

In Equation (4.4)-(4.6) *he* denotes the primary heat exchanger.

Particular attention should be paid to Equation (4.4), where the numerator contains a term identified as ET, whose complete expression is the following:

$$ET = (\dot{m}_{HL,j} - \dot{m}_{HL,j+1}) \cdot T_{\text{HL,X}} \tag{4.7}$$

This term is linked to the strategy of modeling and managing the presence of the expansion tank, which is assumed to be a direct expansion of the cell at the middle of the hot leg, as can be seen in Figure 4.2. The expansion tank is considered capable of dampening any disturbance in the upstream flow, while downstream conditions are imposed by a constant mass flow rate dictated by the pump up to the core inlet. In other words, term ET plays a role in the energy balance of the central subvolume of the hot leg by capturing convective transport toward the expansion tank.

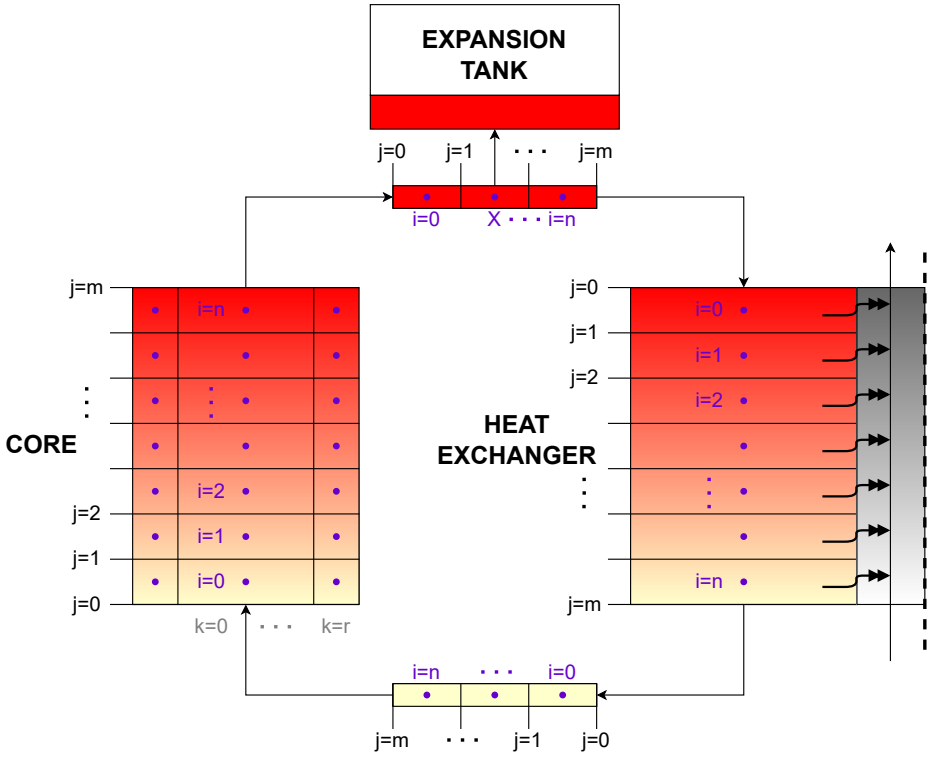

Figure 4.2: Scheme of the model adopted for the analysis.

The cartridges used in Thorizon One feature a unique architecture. Each cartridge consists of an upward flow zone (external) and a downward flow zone (internal), as shown in Figure 2.2. To simplify numerical implementation, the core is modeled with a single preferential flow direction, but divided into two independent parallel channels. Considering that the passage section will therefore be consistent with representing both the upflow and downflow zones, the transit time remains consistent with the physical

one. The thermal-hydraulic behaviour, even in transient conditions, is calculated separately for each channel, while the conditions at the core outlet are obtained as the instantaneous average of the two contributions. The division into two subchannels is consistent with precalculated data on power distribution in subzones of the upflow and downflow regions.

4.2 Coupled Neutronics and Thermal-Hydraulics

The multiphysics approach to capturing the complex dynamics of MSR addresses how heat is generated and then distributed, and how this distribution, in turn, influences heat generation itself. The neutronic module provides the power distribution to the thermal-hydraulic solver, serving as the source term in the energy equation and conditioning the mass flow. The resulting thermal-hydraulic conditions, such as variations in temperature and fuel transit times, are fed back into the neutronic module. A fundamental assumption of the model is that the power fraction distribution at the initial steady-state is known and remains constant throughout the transient.

The governing differential equations of the neutronic and thermal-hydraulic modules are numerically integrated using the fourth-order explicit Runge-Kutta (RK4) scheme [33, 34], with a fixed time step of $\Delta t = 1E-4\ s$. The time step was chosen to ensure numerical stability, ensuring that the Courant–Friedrichs–Lewy (CFL) condition, defined in Equation (4.8), is satisfied in all subvolumes [35].

$$CFL_{conv} = \frac{|u_i|\Delta t}{\Delta x_i} \leq 1 \tag{4.8}$$

In convection dominated flows, the condition expressed by Equation (4.8) ensures that fluid particles do not move more than one mesh distance per time interval [35, 36].

The RK4 method approximates the solution at the next time step (y^{n+1}) as a function of the value at the current time (y^n) according to the following

expression [34]:

$$y^{n+1} = y^n + \frac{1}{6}(k_1 + 2k_2 + 2k_3 + k_4)\Delta t \tag{4.9}$$

where the different k are the derivatives of the quantities to be integrated in four stages over time, calculated in sequence as follows:

1. The slope k_1 is evaluated at the beginning of the interval:

$$k_1 = f(t^n, y^n)$$

2. The slope k_2 is evaluated at the interval midpoint using k_1:

$$k_2 = f\left(t^n + \frac{1}{2}\Delta t, y^n + \frac{1}{2}k_1\Delta t\right)$$

3. The slope k_3 is evaluated again at the interval midpoint, but using k_2 in the calculation:

$$k_3 = f\left(t^n + \frac{1}{2}\Delta t, y^n + \frac{1}{2}k_2\Delta t\right)$$

4. The slope k_4 is evaluated at the end of the interval, using k_3:

$$k_4 = f(t^n + \Delta t, y^n + k_3\Delta t)$$

The expression $\frac{1}{6}(k_1 + 2k_2 + 2k_3 + k_4)$ is a representative slope in the interval, whose graphical representation is shown in Figure 4.3, where h represents the integration step Δt and x_i represents the time.

To ensure mass conservation throughout the computational domain, the continuity equation is applied to each control volume between the core inlet and the expansion tank. Considering a fixed infinitesimal element in space, the partial differential form of continuity equation is [37]:

$$\frac{\partial rho}{\partial t} + \nabla \cdot (rho\vec{U}) = 0 \tag{4.10}$$

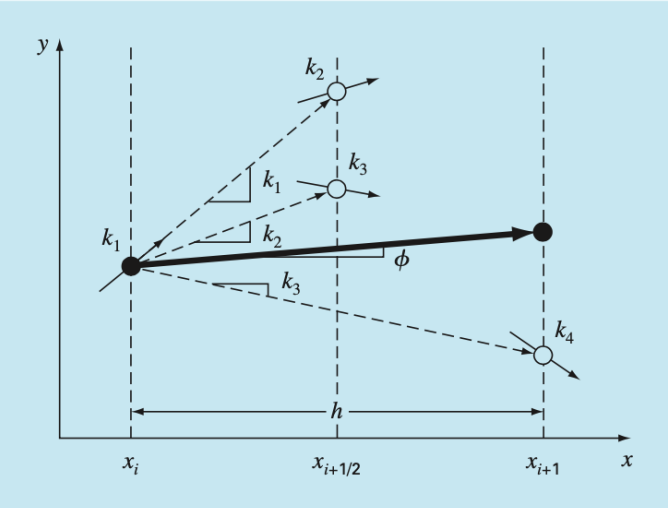

Figure 4.3: Graphical representation of the slope estimates used in the fourth-order Runge-Kutta method [34].

where rho is the fuel salt density, $\nabla \cdot (rho\vec{U})$ is the divergence of the mass flux vector $rho\vec{U}$ and $\vec{U}$ is the velocity vector of the fluid at a given point and time. By integrating over a fixed volume and discretizing the convective flow in one dimension, Equation (4.10) can be rewritten as:

$$\frac{d}{dt}\int_{V_i} rho\, dV + (\dot{m}_{j+1} - \dot{m}_j) = 0 \tag{4.11}$$

Equation (4.11) states that the rate of change of mass within the control volume is balanced by the net mass flow across its boundaries. Approximating the time derivative using a first-order finite difference, Equation (4.11) becomes:

$$\frac{rho_i^{n+1} - rho_i^n}{\Delta t} \cdot V_i + \left(\dot{m}_{j+1}^{n+1} - \dot{m}_j^{n+1}\right) = 0 \tag{4.12}$$

where the superscripts n and $n+1$ are used to denote successive time instants. Rearranging the terms of equation (4.12), the form used to update the mass flow rate at the outlet interface is:

$$\dot{m}_{j+1}^{n+1} = \dot{m}_j^{n+1} - V_i \cdot \frac{rho_i^{n+1} - rho_i^n}{\Delta t} \tag{4.13}$$

Equation (4.13) therefore expresses how the variation in fluid density within a control volume determines a mass flow adjustment between adjacent nodes.

The mass flow rate at the outlet interfaces of each sub-volume is updated sequentially, starting from the first cell of the core and continuing to the cell communicating with the expansion tank. The latter is assumed to dampen any flow disturbance, so that a constant mass flow rate is maintained in the rest of the fuel circuit. It is assumed that fluid motion is primarily influenced by density gradients and the resulting thermal expansion, which indirectly determine mass redistribution. Although this simplification introduces some limitations, it is considered acceptable for the purposes of this analysis, which focuses on the thermal evolution of the fuel salt and DNP transport rather than detailed fluid dynamics.

The model assumes a dilatable and incompressible flow. The density of the fuel salt is expressed as a linear function of temperature, according to the form:

$$rho(T) = rho_0 - a(T - T_0) \tag{4.14}$$

where rho_0 is the reference density at temperature T_0 and a is the slope. This form is assumed to be valid for specific temperature ranges. If the molten salt fuel is assumed to be incompressible, the Doppler effect and density variations act on the same prompt time scale, directly linked to temperature variations within the salt itself [1]. As soon as a temperature change occurs, this translates into reactivity feedback due to the Doppler effect. However, considering that the density of the fluid is solely a function of temperature, any temperature change also triggers density/vacuum reactivity feedback at the same time. Therefore, for analysis purposes, these two mechanisms will be combined and quantified using a total feedback coefficient α_T, expressed in pcm/K.

As regards feedback mechanisms, these are implemented in the present model in a similar way to the LiCore and MOSAICS codes, which use a simplified but physically accurate approach thanks to the introduction of spatial weighting. It has been observed that reactivity and other kinetic parameters defined in Section 3.2.1 depend on the adjoint neutron flux, which represents the importance function. However, calculating the adjoint flux is often impractical due to its high computational costs, as in the case of stochastic methods such as Monte Carlo. To address this issue, a

fundamental simplification is adopted: the adjoint flux ($\varphi^{\dagger}$) is approximated by the direct (unperturbed) neutron flux (φ). Furthermore, the model implements finite volumes that are equal for all cells of the core and of constant size. This ensures consistent weighting and simplifies mathematical operations.

Following the approach used in the LiCore and MOSAICS codes, the contributions of individual cells to reactivity feedback are defined using the local temperature variation and considering the square of the local neutron flux: once for the fission distribution and a second time for the adjoint flux (the importance of these fissions). Based on this approximation—and given that the power distribution is directly proportional to the fission rate and, consequently, to the neutron flux—the square of the normalized power fractions is ultimately adopted as a practical surrogate in the developed model. The temperature-induced reactivity feedback is then evaluated as follow:

1. Spatial weighting map generation: The power fraction for each discretized region (finite volume) of the reactor core is squared. This operation generates a spatial weighting map, which reflects the local importance of each subregion for the overall reactivity.

2. Importance factor normalization: The squared power fractions values are then normalized. This involves scaling them so that their sum across all regions equals one. These step leads to a set of relative importance factors for each region.

3. Global Sensitivity Distribution: A global temperature feedback coefficient (expressed in pcm/K) is then multiplied by these normalized weighting factors. This step allows to obtain local temperature feedback coefficient for each individual region.

4. Calculating the local reactivity change: Each local temperature feedback coefficient is then multiplied by the corresponding temperature deviation (ΔT) from a defined reference value within that specific region, resulting in a reactivity change induced by that region.

5. Summing total reactivity feedback: Finally, the total reactivity feedback

for the entire reactor system is obtained by adding all the individual reactivity contributions of each subregion.

This leads to the following expression for the total reactivity feedback:

$$\rho_{feedback} = \sum_{r=0}^{n_{radial}} \sum_{i=0}^{n_{axial}} \alpha_{r,i} \left(T_{\text{core},i}^{(r)} - T_{\text{ref},i}^{(r)} \right) \tag{4.15}$$

where $\alpha_{r,i}$ represents the local weighted feedback coefficients, computed as:

$$\alpha_{r,i} = \alpha_T \cdot \frac{\left(P_{\text{core},i}^{(r)} \right)^2}{\sum_{r=0}^{n_{radial}} \sum_{i=0}^{n_{axial}} \left(P_{\text{core},i}^{(r)} \right)^2} \tag{4.16}$$

Overall, this methodology provides a computationally efficient and physically motivated approximation of temperature-induced reactivity feedback, preserving spatial fidelity while avoiding the need for periodic flux calculations in perturbed states.

Each time the temperature values of the fuel salt in the core are updated for the next time step, the reactivity feedback calculated according to the Equation (4.15) is used to compute a new reactivity (ρ) value. Reactivity term is assumed to be the sum of:

- Reactivity compensation for steady-state ρ_0
- External provided reactivity ρ_E
- Temperature reactivity feedback $\rho_{feedback}$

$$\rho(t) = \rho_0(t) + \rho_E(t) + \rho_{feedback}(t) \tag{4.17}$$

The update of the reactivity value marks the end of the integrated time step, with all variables being updated and stored. At this point, the algorithm implemented in the code proceeds with the solution of the next time step, unless the transient end time has been reached. This algorithm for time-dependent coupled multiphysics simulation is outlined in Figure 4.4

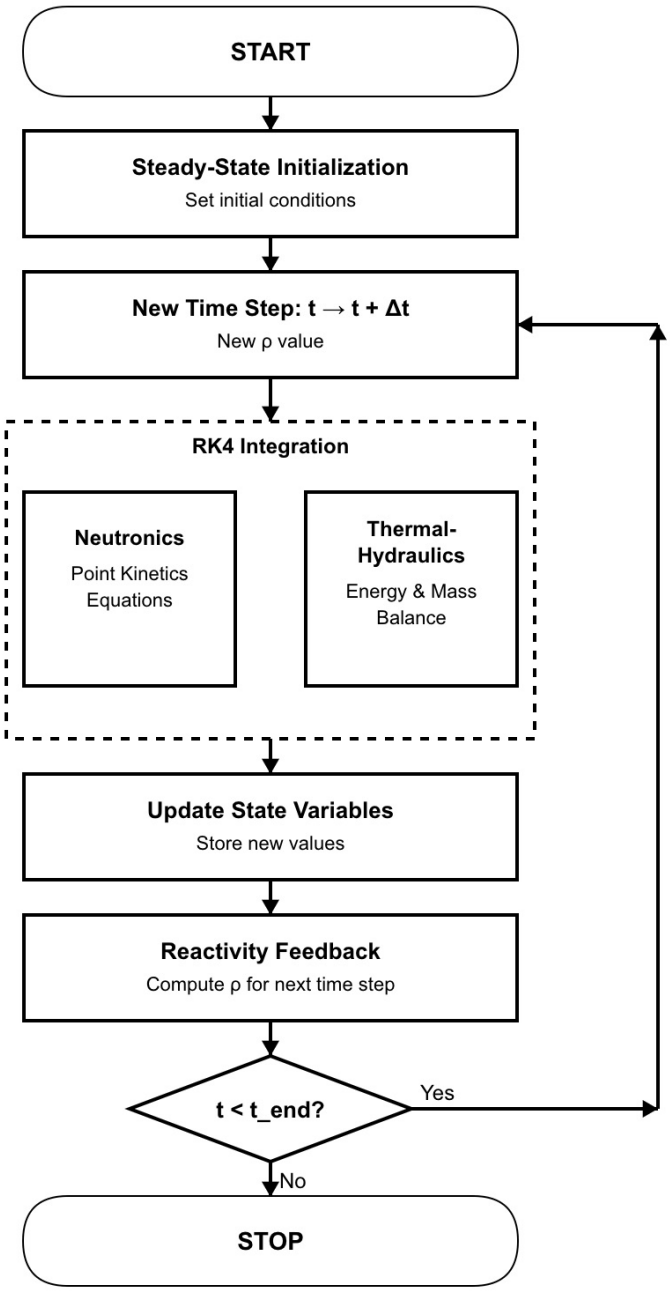

Figure 4.4: Algorithm flowchart for the time-dependent coupled multi-physics simulation.

4.3 Steady-State configuration

In the developed code, several parameters must be set to characterize the reactor steady-state configuration. These parameters include the average fuel temperature, power fractions, salt mass in the system, delayed neutron precursor concentrations, etc.

The approach used to define the reactor at steady-state, is essentially based on solving the equations presented and discussed in Section 3.2.2 and in Section 4.1 for the equilibrium conditions, that is, by setting all time derivatives equal to zero. Thus, the solution lies in solving a system of equations by choosing only a few system variables as inputs. The inputs needed to calculate the temperature distribution in the fuel circuit are the thermal power, the mass flow rate of the salt, and the inlet temperature on the secondary side of the primary heat exchanger, assuming that the heat transfer coefficient, the specific heat of the salt, and the geometry of the fuel circuit are fixed parameters of the reactor.

In the primary heat exchanger for a countercurrent flow configuration, the primary and secondary fluids flow in opposite directions. Heat transfer is calculated by dividing the sides of the heat exchanger into sub-cells, with each sub-cell on the primary side exchanging energy with the corresponding sub-cell on the secondary side. The temperature profile of the secondary fluid is assumed to vary linearly from the inlet (located at the outlet of the primary fluid) to the outlet (located at the inlet of the primary fluid). The temperature of the fuel salt at the inlet of the exchanger is indicated by $T_{he,inlet}$, while the temperature of the salt at the outlet is $T_{he,outlet}$. On the intermediate salt side, the inlet temperature is $T_{cool,inlet}$ and the outlet temperature is $T_{cool,outlet}$. The heat transfer process depends on two global parameters: the overall heat transfer coefficient U_{HX} and the total heat exchange surface area A_{HX}. By imposing an inlet temperature on the secondary side ($T_{cool,inlet}$), the outlet temperature ($T_{cool,outlet}$) is adjusted iteratively until the energy balance condition expressed in equation (4.18) is satisfied. Under steady-state conditions, the operational thermal power is equal to the power exchanged with the intermediate circuit. Let $\dot{m}_f$ denote the mass flow rate of the salt in the fuel circuit and $\dot{m}_{cool}$ the flow rate in

the intermediate cooling circuit. Considering for simplicity that the specific heat c_p of the fuel salt and the intermediate salt are equal, the conditions at the heat exchanger can be written as:

$$\begin{cases} P = \dot{m}_f c_p (T_{he,inlet} - T_{he,outlet}) \\ P = \dot{m}_{cool} c_p (T_{cool,outlet} - T_{cool,inlet}) \\ P = U_{HX} A_{HX} \Delta T_{LM} \end{cases} \tag{4.18}$$

where ΔT_{LM} is the Logarithmic Mean Temperature Difference (LMTD). The LMTD is defined as:

$$\Delta T_{LM} = \frac{(T_{he,inlet} - T_{cool,outlet}) - (T_{he,outlet} - T_{cool,inlet})}{\ln\left(\frac{T_{he,inlet} - T_{cool,outlet}}{T_{he,outlet} - T_{cool,inlet}}\right)} \tag{4.19}$$

Figure 4.5 shows a schematic view of the primary heat exchanger.

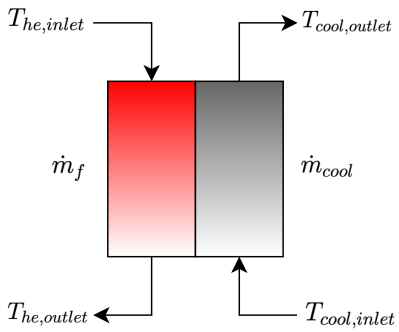

Figure 4.5: Simplified diagram of the primary heat exchanger between the fuel circuit and the intermediate circuit.

The following system of equations is solved iteratively, starting from an initial estimate of the solutions:

- Core equations (energy conservation for each radial channel and axial segment).
- Equations for the heat exchanger (heat balance with the secondary circuit).

- Continuity conditions between the core and the heat exchanger.

The resulting core temperature profile for the reference configuration for the Thorizon One reactor is shown in Figure 4.6, where 2 radial channels were considered (Inner Ch. 1, Outer Ch. 2).

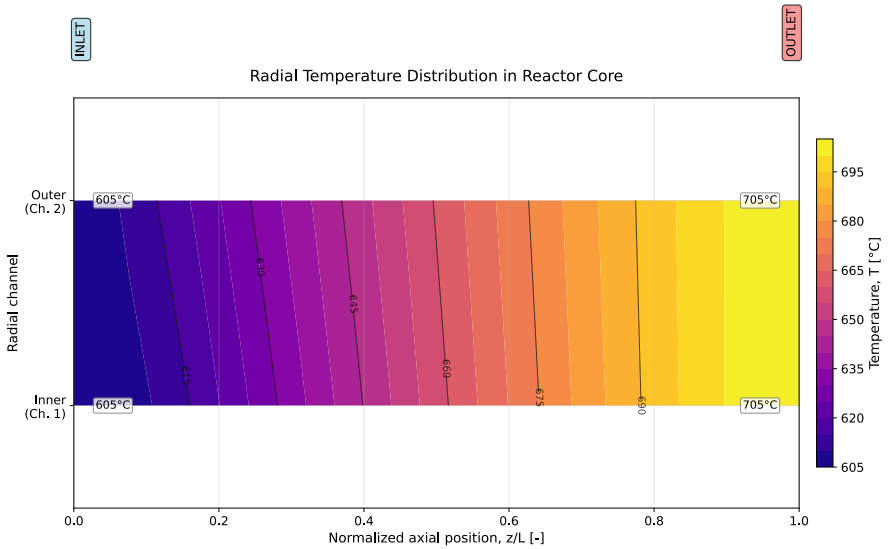

Figure 4.6: Steady-state temperature distribution in the configured core of the Thorizon One reactor.

Since in an MSR some DNP decay in the outer core region, to compensate for this loss it is necessary to introduce an equilibrium reactivity ρ_0. This non-zero positive reactivity is necessary to maintain the reactor in steady-state conditions and is an intrinsic characteristic of circulating-fuel reactors, strongly influenced by the fuel velocity. The expression for ρ_0 comes directly from setting the derivatives of the system of Equations (3.16) of the adopted model (3.16) equal to zero, obtaining:

$$\rho_0 = \tilde{\beta} - \sum_{i=1}^{N} \frac{\tilde{\beta}_i \lambda_i}{\lambda_i + \lambda_c - \lambda_c e^{-\lambda_i \tau_e}} \tag{4.20}$$

This highlights that ρ_0 depends not only on reactor kinetics, but also on the residence times of the fuel in the core ($1/\lambda_c$) and in the external loop (τ_e). It is therefore important to properly define the transit times of the liquid fuel through the different components of the system. These transit times

are calculated using the known temperature distribution and the mass flow rate imposed by the pump, which can be expressed as:

$$\dot{m}_f = rho_i \cdot u_i \cdot A_i$$

where A_i is the cross-sectional area of the i-th cell. Once the density rho_i is computed as a function of temperature, a representing fluid velocity u_i for each sub-cell can be determined. Using the physical length of the sub-cell Δx_i, the corresponding transit time is given by:

$$\tau_i = \frac{\Delta x_i}{u_i}$$

The total transit times for each component of the fluid circuit are then obtained by summing the individual contributions across the respective sub-cells.

Once the geometric parameters, transit times, and instantaneous thermal power are fixed, the delayed neutron precursor concentrations in the critical region is also constrained. For each group of DNP, the following relationship holds:

$$C_i = \frac{\tilde{\beta}}{\Lambda} \frac{P}{(\lambda_c + \lambda_i - \lambda_c e^{-\lambda_i \tau_e})} \quad for \quad i = 1, 2, \ldots, N \tag{4.21}$$

4.4 Transient scenarios

Analyzing different transient scenarios is a crucial aspect for nuclear reactor design and safety. The objective is to investigate the dynamic behaviour of the reactor during the transition from one operating state to another or during an accident scenario.

Reactivity initiated accidents are accidental, rapid increases in reactor power due to an uncontrolled insertion of reactivity. In MSR concepts, such events can be triggered for example by the unexpected withdrawal of neutron absorber rods. RIA can lead to significant, rapid energy deposition and power peaks, which can be dangerous for the structural integrity of the fuel circuit components. In molten salt reactors, the strong negative temperature coefficient of the fuel salt tends to counteract reactivity insertions.

Loss Of Heat Sink (LOHS) accidents involve a sudden degradation or complete loss of primary heat exchanger performance. This leads to a marked temperature increase throughout the fuel circuit. Often it is conservatively assumed that the extracted power drops to zero to assess the most extreme consequences. LOHS events in MSR concepts can originate from various interruptions within the reactor secondary loop.

Load following are considered normal operational transients, where the reactor dynamically adjusts its power output to align with the grid demand. A key advantage of molten salt reactors is their inherent load-following capability, enabling them to meet power demands without the need for active control rod manipulation. In MSR concepts, power can be effectively managed by modulating the fuel salt flow rate.

This work will primarily focus on transients related to RIA. These accidents are of particular interest because they are very rapid events and require in-depth analysis for reactor safety. Specifically, the insertion models currently included are linear ramps and instantaneous insertions such as step or jump. These are represented in Figure 4.7, where ρ_0 is the reactivity compensation in order to guarantee steady-state condition and ρ_E is the external reactivity perturbation.

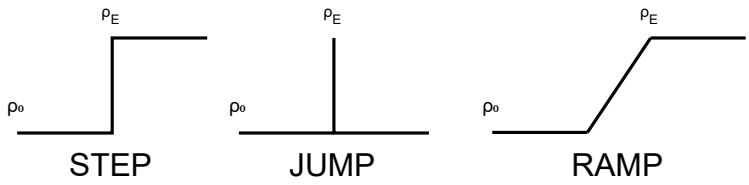

Figure 4.7: Reactivity input models available to drive the simulator.

The initial state from which transient studies begin is a constant-power critical state. This configuration refers to a reactor in steady-state conditions defined as showed in Section 4.3, from which the perturbations start.

Chapter 5

Verification and Benchmarking of the Code

This section summarizes the verification and benchmarking phase of the tool developed during this work and presented in Section 4.2. Benchmarking refers specifically to the comparison of numerical results obtained from different codes that solve the same problem [38]. A code-to-code comparison between the developed code and LiCore, MOSAICS, and TFM-OpenFOAM will be presented. As regards the verification phase, this does not concern the suitability of equations or code to describe a physical problem, as this aspect falls within the scope of validation. The verification phase carried out in this section will refer specifically to the solution verification, with the aim of assessing the numerical accuracy of the simulations through a Grid Convergence Analysis (GCA). The latter is considered one of the most reliable methods for quantifying numerical uncertainty and identifying coding errors [38]. A solution obtained on a single grid, even if fine, does not estimate its accuracy if taken alone. The use of solutions on multiple grids provides a way to estimate the discretisation error and increase the reliability of the solution. The GCA allow to verify the convergence of any quantity of interest and to confirm that the observed order of convergence

(or approximation) is consistent with the theoretical one of the method used.

It is recognised that any validation exercise should be preceded by a rigorous verification [38]. The validation phase involves comparison with experimental data, but this part will not be addressed. Although the experimental results conducted in the past on the MSRE are public, this is a reactor concept that featured square graphite moderator elements in the core, which formed fuel channels [10]. The code developed during this thesis is specific to MSR concepts that do not feature a moderator in the critical region. The energy balance equations presented in Section 4.1 would need to be modified to simulate the MSRE, but this is beyond the scope of this work. The tool developed is designed for the specific analysis of the Thorizon One reactor. The validation part will be replaced by a numerical benchmark with verified codes. In this context, the GCA remains important for characterising and isolating the error introduced by discretisation. Once this aspect has been analysed, it will be easier to identify other possible sources of discrepancy between the numerical results presented in the benchmark analysis.

The benchmarking phase will take as its reference the MSFR, a research-oriented project rather than a commercial design. Research and development efforts on this reactor concept began in 2004 [22]. Over the years, various analyses of reactor dynamics have been carried out using multiphysics codes characterised by different methodologies. The results of complex, high-fidelity codes were subsequently used to verify simpler and computationally faster codes. This was the case for the LiCore, MOSAICS, and TFM-OpenFOAM codes, with the latter constituting the high-fidelity model [11]. The objective of this phase is therefore to test the capabilities of the code developed during this thesis, based on the results of already verified codes. This is of fundamental importance to ensure that the results obtained for the Thorizon One reactor are well-founded. Furthermore, the MSFR does not include a moderator, just like the Throizon One reactor, and this allows to use the developed code for both of these MSR concepts. Before presenting the results of the solution verification and benchmarking phases, the reference MSFR and the corresponding simulation data will be introduced.

5.1 Molten Salt Fast Reactor

Developed by the CNRS as part of the European projects SAMOSAFER, EVOL, and SAMOFAR [3], the MSFR is a circulating fuel reactor characterised by a fast neutron spectrum. Over the years, two versions of the MSFR have been studied. The first, named MSFR-F or 'reference MSFR', is based on a fluoride salt (LiF) and can be used in a thorium fuel cycle. The second, named MSFR-Cl, is based on a chloride salt (NaCl) and can be used in a uranium fuel cycle. Both MSFR versions are breeder reactors designed for a nominal power of 3 GW_{th} and do not use any solid moderator. MSFR design studies should be considered as research and development activities and not as plans for the direct construction of a reactor. The goal is to propose a realistic model based on physics, chemistry, and materials science [5].

The system includes three circuits: the fuel circuit, the intermediate circuit, and the power conversion circuit, as illustrated in Figure 5.1.

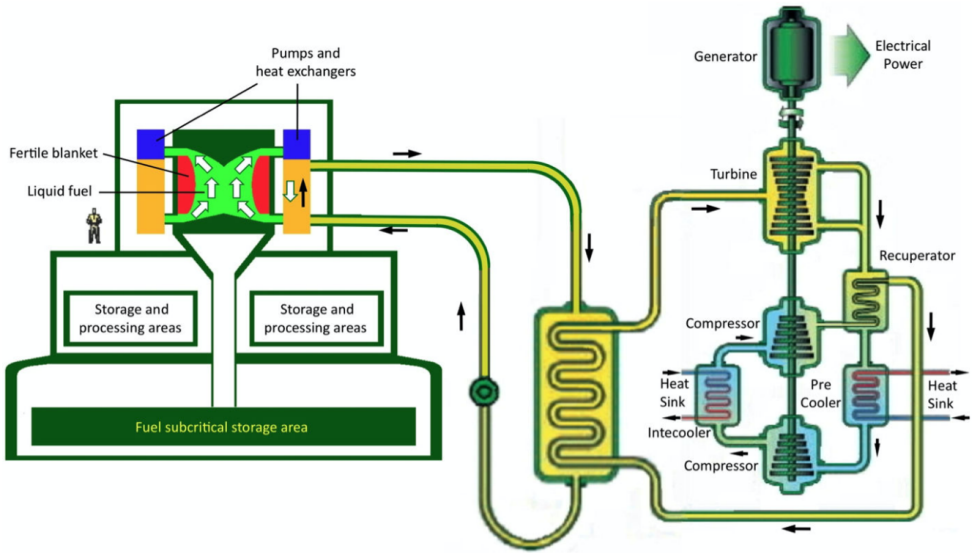

Figure 5.1: Illustration of the MSFR system [5].

The system features a fuel salt drainage system that can be used for planned shutdowns or emergency situations. Drainage occurs by gravity into tanks that maintain a safe reactivity margin and are passively cooled. The fuel

circuit consists of several cooling and recirculation circuits, each equipped with a pump and a heat exchanger. The MSFR-F model has 16 of these circuits, while the MSFR-Cl model has 24. The project involves an on-site reprocessing system to remove most of the fission products without having to interrupt reactor operation [5].

In this thesis, only the MSFR-F concept will be considered for simulations as a benchmarking tool. In the fuel circuit flows a total of 18 m^3 of fuel salt, whose initial composition is LiF-ThF4-(233U or enrU)F4 or LiF-ThF4-(Pu-MA)F3 with 77.5 mol% LiF. Of the 18 m^3 of fuel salt, the MSFR-F design allocates 9 m^3 in the core and 9 m^3 in the region outside the core. The fuel salt flows from the bottom to the top of the core cavity and circulates in the fuel circuit in approximately 3-4 s [5].

The core cavity is surrounded by upper, lower, and radial neutron reflectors made of nickel alloy. The radial reflectors include a fertile blanket to increase the breeding ratio. Figure 5.2 shows a schematic representation of the core and the components inside the reactor vessel. In the initial design phase of the MSFR-F reactor, the core was considered to have a simplified cylindrical geometry, mainly for neutronic studies [39].

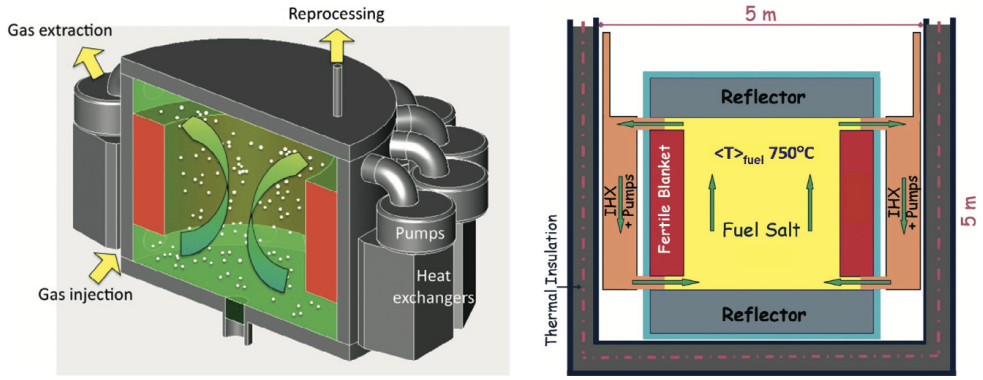

Figure 5.2: Reference Molten Salt Fast Reactor [39]. Left: schematic layout of the reactor; Right: neutronic model layout

Over the years, the geometry of the core has been optimized through thermal-hydraulic studies for turbulence modeling, such as those conducted as part of the EVOL project. Using RANS models, these studies have shown that a core cavity with curved walls and inlet/outlet legs allows for

relatively uniform temperature distribution without the use of flow mixing components [39]. Figures 5.3 and 5.4 show the optimized core geometry and the results of CFD simulations, respectively.

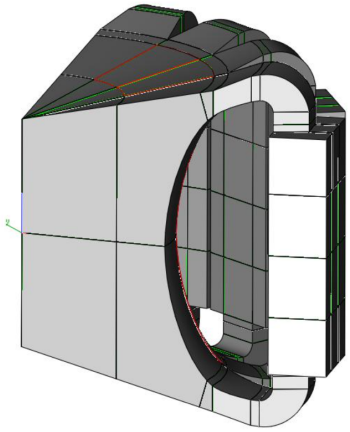

Figure 5.3: MSFR optimized core geometry [5].

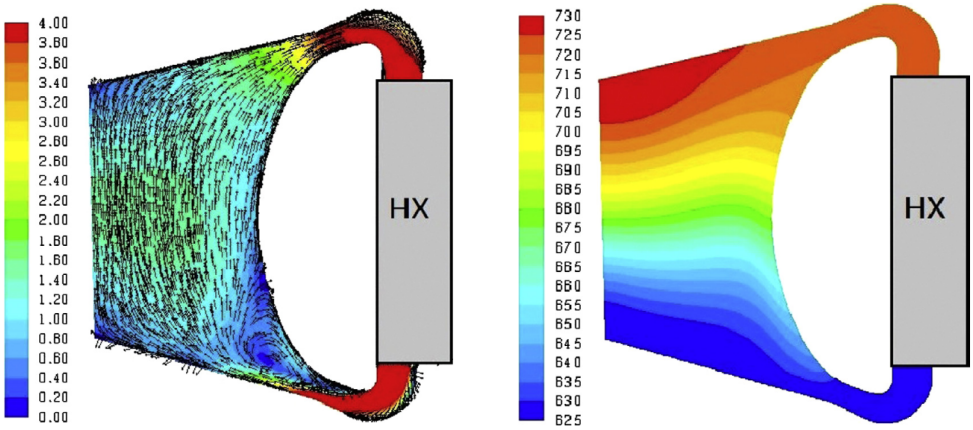

(a) Fuel salt velocity field [m/s] **(b)** Fuel salt temperature field [C]

Figure 5.4: CFD predictions for the 3D core model [39].

5.1.1 Calculation Setup

The comparison system is based on the insertion of reactivity into a reactor similar to the reference MSFR. The code developed in this study, like the LiCore and MOSAICS models, approximates the core as a 2.25 m high and 2.25 m diameter cylinder, with a single inlet and outlet section. In contrast,

the TFM-OpenFOAM tool includes a detailed 3D description of the toroidal core [11]. The LiCore model uses 20 discretisations along the radius and 40 along the height [11], while the code developed during this work uses 5 radial discretisations and 80 axial discretisations, a choice guided by the Grid Convergence Analysis shown in Section 5.2. As regards the comparison with the MOSAICS code, the dimensions of the meshes used are unknown.

The initial conditions of the transients are obtained as described in section 4.3, setting the nominal design power to 3 GW_{th} and the average temperature of the salt in the primary circuit to 700 C. The reference temperature used for calculating the reactivity feedbacks refers to that of the initial state, with the critical reactor in nominal operating conditions. In the model developed for MSFR, the power distribution within the finite volumes of the critical zone is represented by a cosine profile in the axial direction and a Bessel function in the radial direction, with the neutron flux set to zero at the radial boundary and at the top and bottom of the cylinder. In the high-fidelity TFM-OpenFOAM model, the power distribution is calculated taking into account the actual effects of fuel transport using the Transient Fission Matrix approach, then loaded into OpenFOAM [11].

The fuel salt considered in the simulations is a binary fluorinated salt melt with 78%mol LiF-22%mol ThF4. Its density varies linearly with temperature according to [22]:

$$rho(T) = 4094 - 0.882(T[C] - 734.85)$$

Linked to the temperature of the fuel salt, the model assumes a total feedback coefficient of $\alpha_T = -\,8\ pcm/K$, in line with the value adopted in the LiCore and TFM-OpenFOAM models [22]. The values of the thermodynamic and neutronic parameters used in the model are summarized in Tables 5.1 and 5.2, respectively.

Table 5.1: MSFR reactor design parameters [11].

Parameter	Value	Units
P	3000	$\mathrm{MW_{th}}$
$\dot{m}_f$	18562	kg/s
$\dot{m}_{cool}$	22274	kg/s
$T_{\mathrm{cool,inlet}}$	550	C
$\bar{T}_{\mathrm{core}}$	706	C
c_p	1602.3	J/(kg· C)
$rho(T)$	$4094 - 0.882(T[C] - 734.85)$	$\mathrm{kg/m^3}$
α_T	-8	pcm/K
U_{HX}	7100	$\mathrm{W/(m^2{\cdot}K)}$
A_{HX}	3240	$\mathrm{m^2}$
L_{core}	2.255	m
L_{HX}	2	m
L_{legs}	1.78	m
A_{core}	3.99	$\mathrm{m^2}$
A_{HX}	1.62	$\mathrm{m^2}$
A_{legs}	1.62	$\mathrm{m^2}$

Table 5.2: MSFR neutron kinetics parameters [11].

Group	$\tilde{\beta}_i$ $[pcm]$	λ_i $[\mathrm{s^{-1}}]$
1	22.4	0.0125
2	44.8	0.0283
3	39.6	0.0425
4	61.4	0.1330
5	96.7	0.2925
6	15.2	0.6665
7	20.9	1.6348
8	4.5	3.5546

Summary parameters:

- $\tilde{\beta} = 305.5\ pcm$
- $\beta_{circ} = 122.37\ pcm$
- $\rho_0 = 183.13\ pcm$
- $\Lambda = 1.1\ \mu\mathrm{s}$

In Table 5.2 the total effective fraction of delayed neutrons $\tilde{\beta}$ does not take into account DNP drift. The fraction of delayed neutrons that actually remains useful for the chain reaction after losses due to circulation have occurred is indicated by the symbol β_{circ}, whose numerical value satisfies the relationship:

$$\tilde{\beta} = \rho_0 + \beta_{circ}$$

5.2 Grid Independence Study

In general, the greater the number of cells in the computational grid, the better the accuracy of the model solution. The fineness of the grid also directly influences the computation time of the solution [28].

In this section, we focus on the discretisation error. To minimise errors arising from grid coarseness, it is useful to perform a grid dependency (or grid convergence) study. This procedure involves progressively refining an initially coarse mesh until the key parameters remain essentially unchanged. The convergence of these parameters indicates that all other quantities should also converge. Once the results no longer change with grid refinement, the simulation is considered grid-independent [28]. The analysis is based on the solution of a reactivity ramp insertion of 1000 pcm in 0.1 s, starting from the MSFR reactor in steady-state and nominal operating conditions.

To be more representative, the uncertainty of the solution estimated through this analysis requires quantities of interest that are integrated, averaged, or involve a sufficiently large part of the computational mesh [40]. In order to base the study on significant quantities for reactor dynamics, the analysis will focus on the following three variables:

1. Integrated power during the reactivity insertion time interval: Q.

2. Maximum value of the average core temperature during the reactivity insertion time interval: $\bar{T}_{core,max}$.

3. Minimum reactivity value during the reactivity insertion time interval: ρ_{min}.

Instead of simply using the power value derived from the neutronic module,

the parameter Q estimates the energy released during the 0.1 s transient. The other two quantities are functions of the entire mesh that discretises the core, where $\bar{T}_{core,max}$ is the average of the temperature values of each sub-cell in the critical region and ρ_{min} depends on the reactivity feedback, the latter calculated from the contribution of each sub-cell of the core.

The ASME standardized approach is used to perform the GCA, which is based on the Grid Convergence Index (GCI) method [41]. The first step of the analysis consists in generating a refinement sequence of at least 3 different grids, with the aim of demonstrating the monotonic reduction of the discretisation error on successive levels of mesh refinement. Three different grids are used in this analysis, referred to as fine, medium, and coarse, and indexed as 1, 2, and 3, respectively. Each grid includes 5 radial discretisations and 160, 80, and 40 axial discretisations for the fine, medium, and coarse cases, respectively.

For each of the meshes used in the refinement sequence, a representative grid size h must be defined. For 3D simulations and nonstructured grids, the representative grid size is defined as [41, 42]:

$$h = \left[\frac{1}{N}\sum_{i}^{N}(V_i)\right]^{1/3} \tag{5.1}$$

where V_i is the area of the i-th cell, and N is the total number of cells used for the computations.

The one-dimensional computational grid used in the present model is non-uniform. A non-uniform grid allows for finer spacing in areas where greater accuracy is required, such as the core and heat exchanger, and coarser spacing for the hot leg and cold leg regions. Generalizing the definition of h in Equation (5.1) for a one-dimensional case, it is possible to compute the representative grid size as [41, 40, 42]:

$$h = \frac{1}{N}\sum_{i=1}^{N}\Delta x_i \tag{5.2}$$

where Δx_i denotes the length of the i-th cell.

Once the characteristic dimensions of the grid for each mesh have been defined, the refinement ratios are calculated between the medium and fine grids, expressed as r_{21}, and between the coarse and medium grids, expressed as r_{32}:

$$r_{21} = \frac{h_2}{h_1}, \quad r_{32} = \frac{h_3}{h_2} \tag{5.3}$$

The grid refinement ratios (or factors) must be greater than a threshold of 1.3. This threshold value is based on practical experience rather than a formal derivation [42]. In this study, values of 2.00719 and 2.00358 were obtained for r_{32} and r_{21}, respectively.

Using the refinement ratios and solutions Γ obtained for the key parameters on the respective grids, the observed order of approximation b is estimated using the following expression [41, 40, 42]:

$$b = \frac{1}{\ln(r_{21})} \left| \ln \left| \frac{\Gamma_3 - \Gamma_2}{\Gamma_2 - \Gamma_1} \right| + q(b) \right| \tag{5.4}$$

where

$$q(b) = \ln \left(\frac{r_{21}^b - s}{r_{32}^b - s} \right) \tag{5.5}$$

and

$$s = 1 \cdot \text{sign} \left(\frac{\Gamma_3 - \Gamma_2}{\Gamma_2 - \Gamma_1} \right) \tag{5.6}$$

Equations (5.4)-(5.6) can be solved iteratively and the value of b is updated until it no longer changes significantly. The initial estimate for the iteration is set to $b = 2$. The correspondence between the observed order of approximation and the order of the scheme used is considered a good indication that the grids are in the asymptotic range [42]. In this case, values very close to one, consistent with the first-order upwind scheme, were found for all key parameters studied, as shown in Table 5.3.

Before calculating the GCI, it is still possible to provide an optimal estimate of what the solution would be on a grid without mesh-induced uncertainties. This is done using Richardson extrapolation, a functional approach in cases where monotonic convergence occurs [41, 40, 42, 38]. The type of

convergence is verified using the Convergence Ratio CR [40]:

$$CR = \frac{\Gamma_2 - \Gamma_1}{\Gamma_3 - \Gamma_2} \tag{5.7}$$

The analysis reveals CR values between 0 and 1, thus converging monotonically. The Richardson's extrapolation to estimate the grid-independent asymptotic value of the solutions is then performed as follows [41, 40, 42]:

$$\Gamma_{\text{ext}} = \frac{r_{21}^b \Gamma_1 - \Gamma_2}{r_{21}^b - 1} \tag{5.8}$$

Finally, the grid convergence index can be calculated. First, the relative errors ϵ between the solutions Γ are defined. The errors are simply the difference in the quantity of interest for the various grid levels:

$$\epsilon_{32} = \left| \frac{\Gamma_2 - \Gamma_3}{\Gamma_2} \right|, \quad \epsilon_{21} = \left| \frac{\Gamma_1 - \Gamma_2}{\Gamma_1} \right| \tag{5.9}$$

Then, introducing a safety factor F_s, which is usually taken equal to 1.25 when using three grids, the convergence index between the different grids is determined using the following expression [41, 42]:

$$GCI_{32} = \frac{F_s \, \epsilon_{32}}{r_{32}^b - 1}, \quad GCI_{21} = \frac{F_s \, \epsilon_{21}}{r_{21}^b - 1} \tag{5.10}$$

Multiplying the values obtained from Equation (5.10) by 100 converts the different GCI into percentages. These values represent the numerical uncertainty when moving from the coarse grid to the medium grid and from the medium grid to the fine grid. In the case study, all GCI obtained values are lower than 1%, indicating that the grids used introduce negligible uncertainties related to the mesh.

To verify that the grids used fall within the Asymptotic Range AR, the ratio of the grid convergence indices is taken into account, scaled to the observed order of approximation according to the expression:

$$AR = \frac{r_{21}^b \, GCI_{21}}{GCI_{32}} \tag{5.11}$$

In the analysis performed, this parameter was always close to unity, indicating that a low level of uncertainty was achieved at the finest grid level [40].

The results of the grid convergence analysis are summarized in Table 5.3. The results of the GCA guide the choice of the optimal mesh, which guarantees low discretisation uncertainty while remaining computationally accessible. Based on this analysis, the medium grid was chosen for the benchmarking phase with other codes, as it offers both minimal discretisation uncertainty and moderate computational cost.

Table 5.3: Summary of GCA

	$\Gamma = Q\ [GJ]$	$\Gamma = \bar{T}_{core,max}\ [C]$	$\Gamma = \rho_{min}\ [pcm]$
Γ_3	4.2896	765.5884	184.1901
Γ_2	4.2846	765.8608	184.1770
Γ_1	4.2823	766.0056	184.1704
b	1.0920	0.9038	0.9915
CR	0.46	0.53	0.50
Γ_{ext}	4.2802	766.1714	184.1638
ϵ_{32} [%]	0.1173	0.0356	0.0071
ϵ_{21} [%]	0.0547	0.0189	0.0036
GCI_{32} [%]	0.1286	0.0507	0.00895
GCI_{21} [%]	0.0602	0.0270	0.0045
AR	0.999	0.998	1.001

5.3 Numerical Benchmarking with existing codes

The objective now is to test the capabilities of the code developed during this thesis and to understand its limitations and strengths. The numerical benchmark in this section evaluates the consistency of the developed model with verified codes such as LiCore, MOSAICS, and TFM-OpenFOAM in the same transient scenarios. Since the grid convergence analysis has shown that the solutions of the present model are not affected by discretisation errors, the attention now shifts to identifying possible sources of discrepancy with the results obtained by these other codes.

The results used for comparison were collected by digitising graphs related to various RIA analyzed for the MSFR. Specifically, Lemeute et al. [43] presents results obtained using MOSAICS and collected in a CEA presentation, while Axel Laureau's doctoral thesis [11] presents results relating to different codes, including TFM-OpenFOAM, a Corrected Point Kinetic model, and Licore [11, 26]. The last two codes are presented in the results with the labels CP and CPZ, respectively, as originally named in the thesis [11].

It is important to note that the codes mentioned above adopt different mathematical models and approaches, some more simplified than others. A first substantial difference between the codes is represented by the geometric description of the fuel circuit. The complex geometries of the MSFR, used as a reference reactor in this analysis, can only be represented in the high-fidelity TFM-OpenFOAM code. The other codes implement a 1D description of the primary circuit, with a cylindrical core geometry. Concerning neutronic and hydraulic input parameters used in the analysis, it is crucial that they remain consistent across all models. The present model is adapted to the MSFR concept using the input data reported in the reference works [43, 11]. These parameters are those already reported in Section 5.1.1 and used for the GCA.

Ramp reactivity insertion of 1000 pcm in 0.1 s

The first transient to be discussed corresponds to a reactivity insertion of 1000 *pcm* in 0.1 *s*. During the transient, the intermediate salt temperature distribution in the heat exchanger is fixed. The power extracted will therefore be proportional to the evolution of the temperature difference between the fuel salt and the intermediate salt. This is the same strategy used in Axel Laureau's doctoral thesis, where the TFM-OpenFOAM, CP, and CPZ codes were compared [11].

The results obtained are shown in Figure 5.5. Before discussing the comparisons between the codes, let's focus on the evolution of the physical quantities. The rapid increase in reactivity immediately leads to a sharp increase in power. As a result, the fuel salt core temperature also increases, which in turn causes a drop in reactivity and, consequently, in power. As

reactivity insertion continues, reactivity and power increase again, creating the oscillations in both quantities seen in the top and middle panel of Figure 5.5. To improve understanding of the temporal order of these oscillations, Figure 5.6 shows the evolution of power and reactivity during the insertion time interval with a linear time scale. The oscillations observed can be attributed to the thermal inertia of the fuel salt, which introduces a time delay between changes in power and changes in fuel temperature. Note that the temperature shown in the bottom panel of Figure 5.5 is relative to the average temperature of the fuel salt throughout the fuel circuit. The CP model does not take into account the fuel salt outside the core, which distorts the comparison value.

When the reactivity insertion stops at $t = 0.1\ s$, the power decreases rapidly, as the fuel temperature increase in the critical region has generated strong reactivity feedback. When colder salt subsequently enters the core at $t \sim 1\ s$, there is an increase in reactivity and a corresponding increase in power. Reactivity decreases again as the heated salt re-enter the core at $t \sim 4\ s$, in line with the circulation time of the salt through the fuel circuit.

The developed code reproduces the evolution of the main physical parameters closely matching that obtained with CPZ in the reactivity insertion time interval. This is due to the very similar approach to the treatment and implementation of neutronics between CPZ (or LiCore) and the present model. However, the evolution of reactivity at time $t \sim 1\ s$ is reproduced differently. The oscillation seen here is due to the circulation of molten salt. The simplest CP model, in which the reactor is reduced to a single point, is unable to reproduce any circulation and, therefore, capture the related oscillation. In contrast, all other models capture this behaviour, although with some differences resulting from the different geometric configurations and flow distributions.

Agreement with the CPZ (or LiCore) code is generally strong, and the various phenomena related to fuel motion are reproduced, even if their amplitude is not entirely correct.

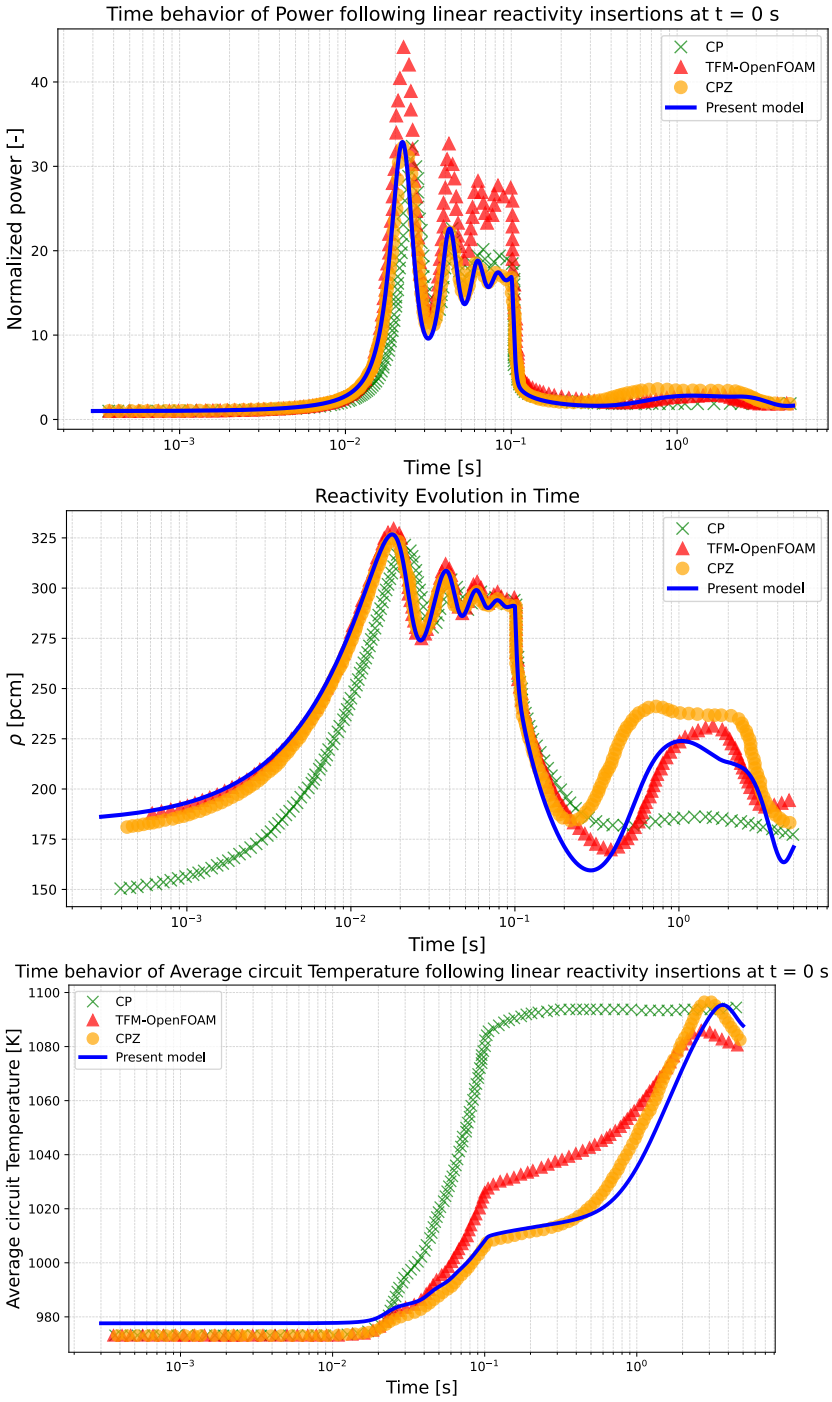

Figure 5.5: Transient behaviour for 1000 *pcm* in 0.1 *s* ramp reactivity in MSFR model. Top panel: normalized power; Middle panel: reactivity; Bottom panel: average fuel circuit temperature.

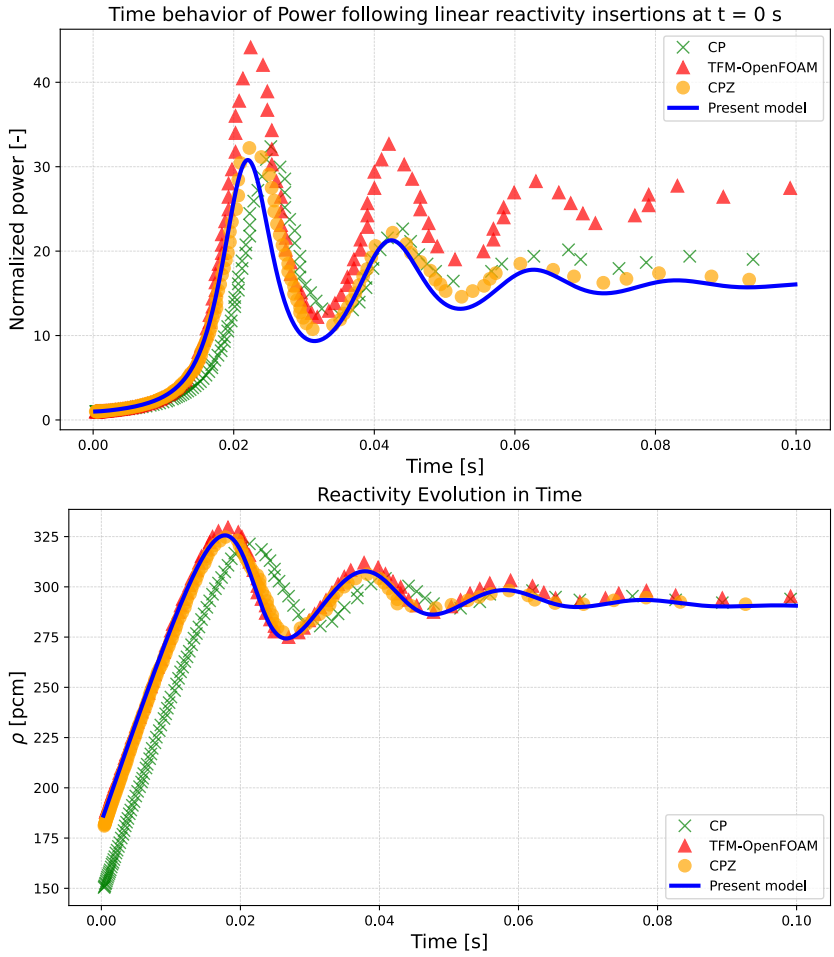

Figure 5.6: Transient behaviour for 1000 *pcm* in 0.1 *s* ramp reactivity in MSFR model (linear time scale). Top panel: normalized power; Bottom panel: reactivity.

Ramp reactivity insertion of 6000 pcm in 1 s

The second transient corresponds to a reactivity insertion of 6000 *pcm* in 1 *s*. With a longer insertion duration in this transient, the effect of fuel salt transport is highlighted. In this simulation, the distribution of the intermediate temperature of the salt in the heat exchanger is fixed. The results are shown in Figure 5.7.

For the simulated scenario, the models capture the effect of hot salt fuel movement on neutronics differently, reflecting differences in geometry and flow description. Furthermore, in order to improve the agreement of the present model with the high-fidelity TFM-OpenFOAM model, the description of the neutron flux shape should be improved. The code developed considers a constant neutron flux, which is also used to describe the weighting for the adjoint flux (for importance). In contrast, the TFM approach allows the shape of the neutron flux, the adjoint flux, and the counter-reactions to be calculated accurately. These are areas for improvement that still need to be implemented in order to better calibrate the simplified tool developed.

However, the present code remains consistent with the CPZ tool, with discrepancies becoming more pronounced when behaviour is no longer governed solely by neutronics. These discrepancies probably also stem from the numerical diffusion of the first-order upwind scheme used in this code. In contrast, CPZ (or LiCore) uses a Lagrangian method for fluid motion, which allows for zero numerical diffusion.

An interesting aspect of the results of this transient is that, despite the very pronounced reactivity insertion in magnitude, the power fluctuates by about 15 times the nominal power. When compared with the results obtained for the insertion of 1000 *pcm* in 0.1 *s* in Figure 5.5, where the power fluctuated at values of over 20 times the nominal power, it therefore appears that the maximum calculated power does not depend on the total reactivity inserted, but on the reactivity insertion ramp. In any case, it should be noted that reactivity insertions of 6000 *pcm* are considered unrealistic. The maximum reactivity reserve, obtained by compacting the fuel salt into a spherical core, would result in a reactivity insertion of approximately 2000 *pcm* [44].

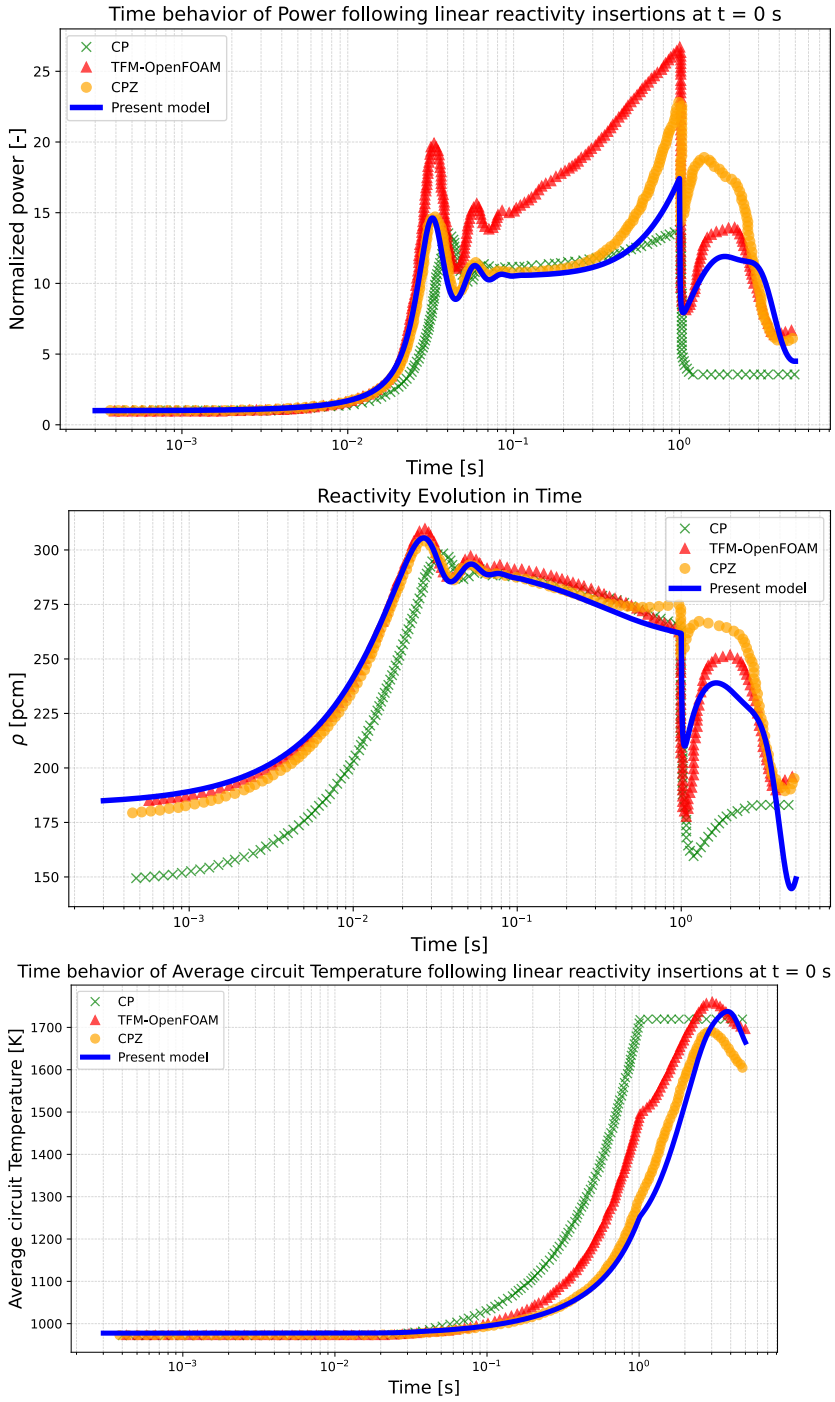

Figure 5.7: Transient behaviour for 6000 *pcm* in 1 *s* ramp reactivity in MSFR model. Top panel: normalized power; Middle panel: reactivity; Bottom panel: average fuel circuit temperature.

Step reactivity insertion of 400 pcm

The last useful transient for the numerical benchmark is related to a step reactivity insertion of 400 *pcm*. This is not a very physical transient, but it is useful for testing the capabilities of the developed code. An instantaneous insertion of reactivity, such as a step, is a limiting case, since in reality reactivity changes occur gradually and irregularly due to the limited speed of movement of the control elements and of the redistribution of fuel [11, 45]. During the transient, the heat extraction in the primary heat exchanger is set at 3 GW_{th}. Since this transient was modeled with MOSAICS [43], the comparison will be made with the corresponding results of this code.

The results are showed in Figure 5.8. The analysis of this limiting case focuses on the initial phase of the transient ($t < 0.1\ s$), when neutron physics plays a dominant role. Following the insertion of reactivity, the power increases exponentially, as does the temperature. The increase in temperature quickly generates a strong reactivity feedback, causing a very sharp drop in power.

The results obtained with the present model show excellent agreement with those produced by MOSAICS, with consistent amplitude values. This increases confidence in the proper performance of the neutronic module.

Overall, the comparisons between the developed code and LiCore, TFM-OpenFOAM, and MOSAICS are quite satisfactory and suggest that the tool can be used for the Thorizon One reactor. Although the results obtained are not as accurate as in the case of the TFM approach coupled with OpenFOAM, the orders of magnitude of the results are good and provide useful insights. The present model is simplified but allows for rapid simulations, sensitivity studies, and analysis of long transients. This provides a basic understanding of the safety characteristics of MSR and enables preliminary physical assessments.

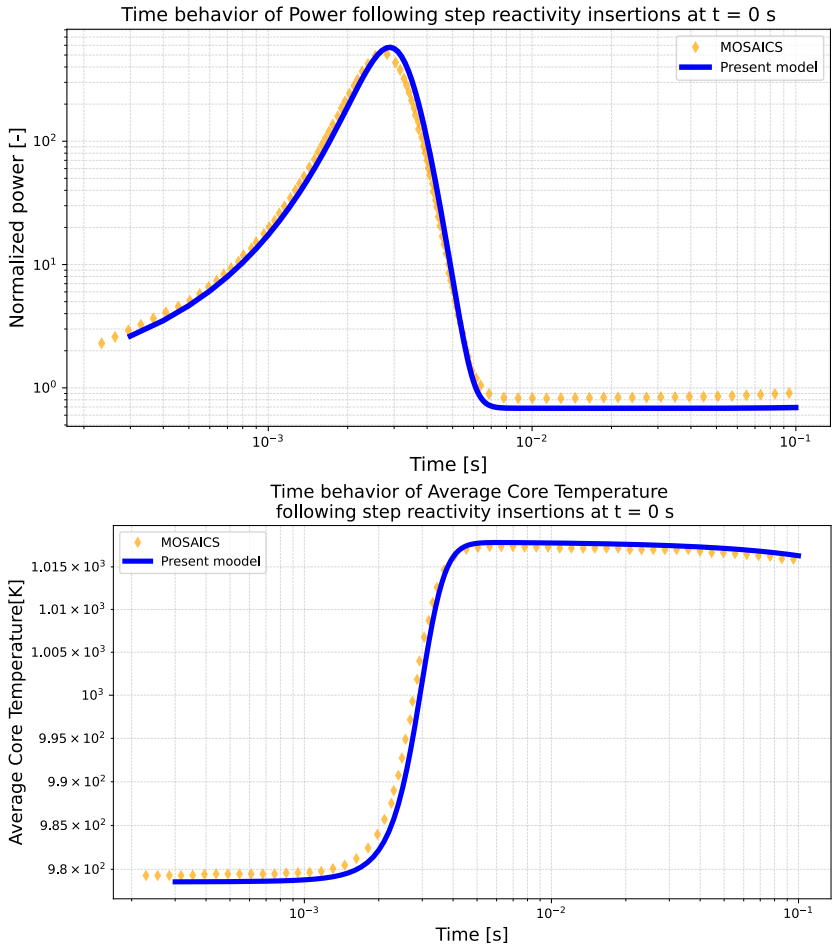

Figure 5.8: Transient behaviour for 400 *pcm* step reactivity in MSFR model. Top panel: normalized power; Bottom panel: average core temperature.

Chapter 6

Transient Analyses for the Thorizon One reactor

The model verified through the analysis conducted in Chapter 5 is now used to better understand the dynamics of the Thorizon One reactor. To characterise the reactor more comprehensively, the code is further improved to implement several driving events relevant to reactor safety. These include some of the design basic accidents, unprotected accidents that can reveal the influence of phenomena specific to circulating fuel reactors. The adjective 'unprotected' refers to the fact that no protective action is triggered in the fuel and intermediate circuits during the transients, which is crucial in assessing intrinsic safety characteristics. The events analysed are specifically:

1. Reactivity initiated accidents.

2. Loss of heat sink.

3. Fuel-pump driven transients.

The focus on developing different scenarios is also important in order to provide Thorizon with the most comprehensive tool possible, capable of estimating the orders of magnitude of the evolution of the physical quantities of interest and providing design insights. To this end, the following section also presents a preliminary sensitivity study on two characteristic parameters of the reactor: core length and nominal mass flow rate.

6.1 Thorizon One Model

The reactor core will be considered as a single region with geometric dimensions consistent with the sum of volumes of fuel salt occupying the upper active part of the cartridges. The same criterion has been used for the other components shared by each cartridge, with the aim of inserting a single primary heat exchanger, an expansion chamber simulating an overall gas plenum and, finally, a hot and a cold leg representing the sections of the circuit in which the hot and cold salt flow respectively. The conversion of the power fractions of the individual cartridges into a total power fraction for a single cylindrical core results in power fractions that add up to 0.9964, thus representing 99.64 % of the nominal power. In order not to alter the distribution of power fractions, a nominal power level of 249.1 MW_{th} will be used instead of the specified design value of 250 MW_{th}.

In the reference operating conditions, the core inlet temperature is approximately 600 C, while the core outlet temperature is around 700 C. The core will be defined as a cylinder containing a homogeneous isotopic composition of fuel and approximately 42 % of the total salt present in the fuel circuit. Of the 23 m^3 of fuel salt present in the circuit, 9.9 m^3 are in the core region and 13.1 m^3 are in the external (out-of-core) region. Considering a fuel chloride salt composition of NaCl 55%, UCl_3 40.5% and $PuCl_3$ 4.5%, the total feedback coefficient is assumed to be $\alpha_T = -11.1$ pcm/K, consistent with the value reported in the CEA study [46].

Following a grid convergence analysis carried out on the Thorizon One reactor concept, the optimal grid that will be used in the following simulations involves axial discretizations of 78 sub-volumes and radial discretizations of 2 sub-channels for the core. The use of 2 sub-channels directly represents the upflow and downflow regions of the cartridges, schematically represented in Figure 2.2.

The values of the thermodynamic and neutronic parameters used in the model for the Thorizon One reactor are summarized in Tables 6.1 and 6.2, respectively. The model employed eight groups of delayed neutron precursors, with the effective delayed neutron fraction ($\tilde{\beta}$) chosen to match the value calculated for the MSFR initiated with transuranic elements [47].

Table 6.1: Thorizon One reactor design parameters.

Parameter	**Value**	**Units**
P	249.1	$\mathrm{MW_{th}}$
$\dot{m}_f$	4151	kg/s
$\dot{m}_{cool}$	4981	kg/s
$T_{\mathrm{cool,inlet}}$	530	C
$\bar{T}_{\mathrm{core}}$	650	C
c_p [43]	630.7	J/(kg·C)
$rho(T)$	$rho_0 - a(T - T_0)$	$\mathrm{kg/m^3}$
α_T [46]	-11.1	pcm/K
U_{HX}	2000	$\mathrm{W/(m^2{\cdot}K)}$
A_{HX}	1200	$\mathrm{m^2}$
L_{core}	1.8	m
L_{HX}	1.8	m
L_{legs}	0.8	m
A_{core}	5.5	$\mathrm{m^2}$
A_{HX}	5.5	$\mathrm{m^2}$
A_{legs}	2	$\mathrm{m^2}$

Table 6.2: Thorizon One neutron kinetics parameters.

Summary parameters:
• $\tilde{\beta} = 294.6\ pcm$ [47]
• $\beta_{circ} = 193.98\ pcm$
• $\rho_0 = 100.62\ pcm$

6.2 Reactivity initiated accident

Reactivity initiated accidents are modeled by directly modifying the reactivity input in the neutronic module. The effect of reactivity insertions depends greatly on the type of insertion being simulated, as already observed during the code benchmarking phase in Section 5.3. This section analyses the response of the Thorizon One reactor to better understand its sensitivity to reactivity insertion and estimate the insertion required to bring the reactor into prompt supercriticality. In all simulations in this section, the extracted power in the primary heat exchanger is fixed at the steady-state nominal value.

In general, when the total reactivity of the system is greater than zero but less than the effective fraction of delayed neutrons ($0 < \rho < \tilde{\beta}$), the system is said to be delayed supercritical, and the neutron population increases on a timescale essentially governed by precursors. If the condition $\rho > \tilde{\beta}$ occurs, the system is said to be prompt supercritical and the neutron population will evolve on a timescale related to the mean lifetime of prompt neutrons Λ, thus much faster than the typical time scale of precursors. When liquid fuel is circulating, the DNP drift reduces the total effective fraction of delayed neutrons in β_{circ} compared to that with static fuel $\tilde{\beta}$. This characteristic reduces the margin for prompt supercriticality compared to solid-fuel reactors. Circulating fuel systems are maintained in a critical state by introducing a compensating reactivity ρ_0 corresponding to the loss of reactivity due to fuel circulation. This means that, although the condition of prompt supercriticality always applies for $\rho > \tilde{\beta}$, in circulating fuel reactors this can be achieved by an insertion of external reactivity of $\rho_0 + \rho_E > \tilde{\beta} = \rho_E > \beta_{circ}$.

Ramp reactivity insertions in 0.1 s

The following analysis focus on ramp reactivity insertions in 0.1 s, with different values of inserted reactivity ranging from 500 *pcm* to 3000 *pcm*. These cases involve rapid and high-magnitude reactivity insertions. Although larger insertions may exceed physically achievable values, they are useful for studying the neutron behaviour of the Thorizon One reactor. The

results of these simulations are shown in Figure 6.1.

In all cases, during the reactivity insertions, the reactor enters a prompt supercritical state, as the instantaneous reactivity is greater than $\tilde{\beta}$, which is equal to 294.6 *pcm* as reported in Table 6.2. An interesting aspect is that the transition from delayed supercriticality to prompt supercriticality occurs gradually, without any sudden change in the behaviour of the reactor.

When switching from an insertion of 500 to 1000 *pcm* in 0.1 *s*, it can be seen how oscillations begin to develop in the first moments of transient for reactivity and power. This is due to the thermal inertia of the fuel salt and strong reactivity feedback that occur during the reactivity insertion ramp. These oscillations gradually increase in depth when considering the events with insertions of 2000 and 3000 *pcm*, respectively. However, the overall behaviour is not significantly different between the different cases.

Another general behaviour that can be observed is that increasing the reactivity inserted results in an earlier and higher initial power peak. Once the ramp insertion ends, the power level drops sharply, then increases slightly and stabilizes for a short period (between ∼2 *s* and ∼10 *s* after the start of the transient) as colder salt replaces the heated salt during the reactivity insertion. The latter subsequently returns to the critical region after circulating through the external circuit in approximately 10 seconds, causing a large negative reactivity feedback and a corresponding decrease in power, as can be seen in the top and middle panels of Figure 6.1. This phenomenon causes a power undershoot, where the power temporarily drops below its initial value. The oscillations caused by the circulation of the fuel salt continue and decrease in amplitude during the simulation. Gradually, the reactor would return to equilibrium conditions, with a power level equal to 249.1 MW_{th} set by power exchange in the primary heat exchanger, and the salt temperature tending to stabilise at a higher value for greater reactivity insertions.

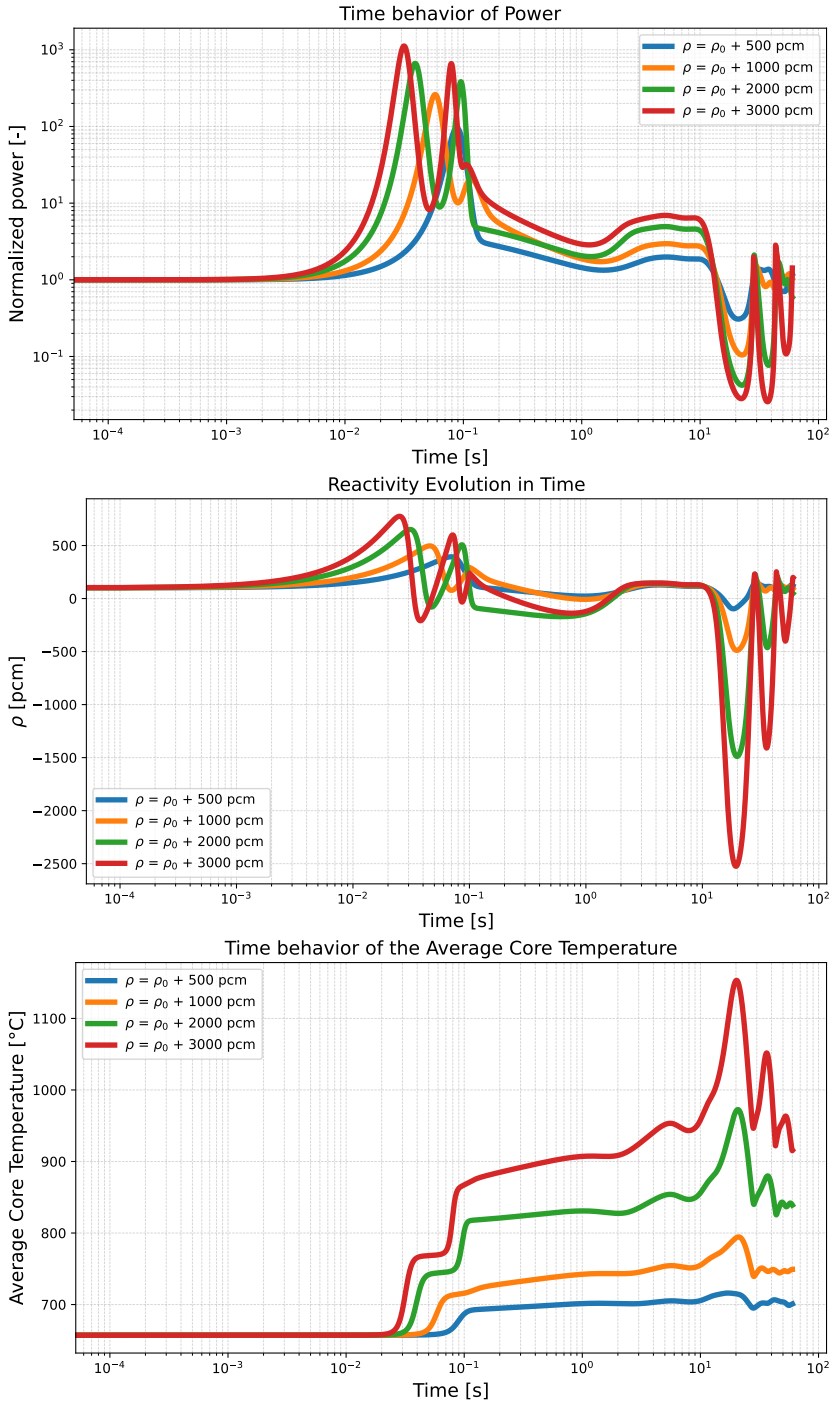

Figure 6.1: Transient behaviour for ramp reactivity insertions in 0.1 s in Thorizon One model. Top panel: normalized power; Middle panel: reactivity; Bottom panel: average core temperature.

Ramp reactivity insertions in 1 s

The study now focuses on the same reactivity insertions as in the previous case, ranging from 500 *pcm* to 3000 *pcm*, but with a longer insertion ramp of 1 *s*, in order to analyse how the reactor behaviour varies. The results for these scenarios are shown in Figure 6.2.

This analysis shows how the same reactivity insertions over a longer period of time lead to less violent behaviour. The power and reactivity peaks are lower in amplitude and occur later compared to the case of ramp insertions in 0.1 *s* shown in Figure 6.1. Moreover, the oscillations in reactivity and power observed during the ramp are less pronounced compared to the previous case. It can therefore be seen that it is not the magnitude of reactivity inserted that distinguishes the behaviour of the reactor, but rather the insertion time of this reactivity. A further distinction concerns the fact that higher total reactivity values than $\tilde{\beta}$ are only achieved when 2000 and 3000 *pcm* are inserted in 1 *s*, while 1000 *pcm* in this case are no longer sufficient to lead the reactor to prompt supercriticality. This occurs because, during a longer ramp, thermal feedback has time to reduce the total reactivity relatively quickly, even with a high reactivity insertion. The transition from delayed supercritical to prompt supercritical conditions remains continuous, and the overall response of the reactor does not vary significantly in the different cases. In relation to the circulation time of the fuel salt initially heated during the ramp, oscillations with power undershoot occur also in this case.

Regarding the evolution of the fuel salt temperature, its final change toward the new steady-state condition matches that observed in the 0.1 *s* ramp cases. For the reactor to return to its initial power level, the total net reactivity must return to the DNP-drift reactivity compensating value ρ_0. This requires that the externally introduced reactivity be exactly balanced by the increase in the average core temperature, with the relationship defined by the total feedback reactivity coefficient. If the reactivity insertion is the same, the average core temperature change will be the same, regardless of how quickly the reactivity was introduced.

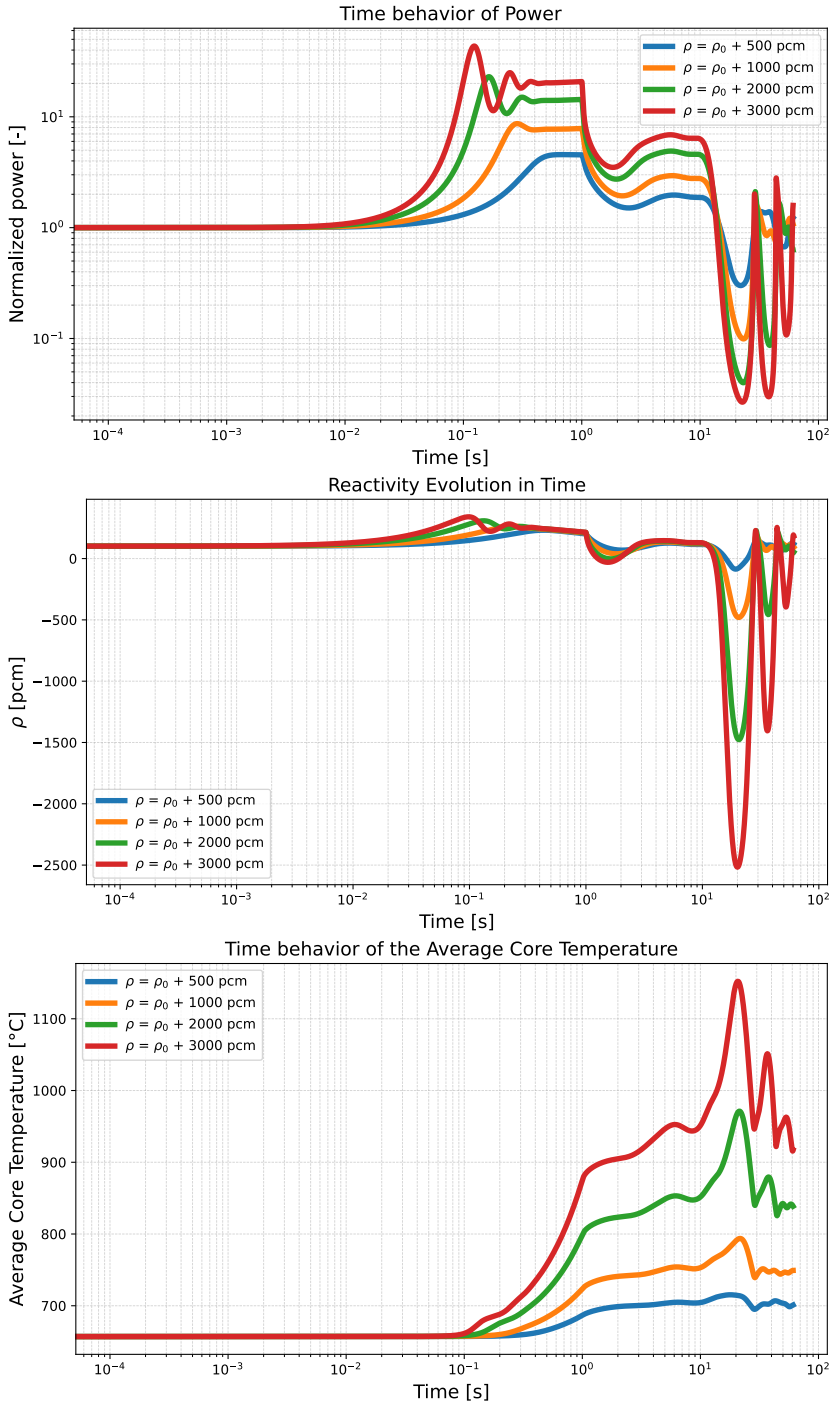

Figure 6.2: Transient behaviour for ramp reactivity insertions in 1 s in Thorizon One model. Top panel: normalized power; Middle panel: reactivity; Bottom panel: average core temperature.

Step reactivity insertion

The analysis now focuses on step reactivity insertions, which represents the worst-case scenario, even if not very physical. Since the external reactivity is inserted instantaneously, thermal feedback cannot immediately play a role in decreasing the reactivity and therefore the power. The reactor's response depends heavily on the ratio between the external inserted reactivity (ρ_E) and the fraction of DNP decaying in the core (β_{circ}); if ρ_E is greater than β_{circ}, the reactor enters a prompt supercritical state. It would make no sense to simulate reactivity insertions ranging from 500 to 3000 *pcm*, since, in addition to being unrealistic, they would all reflect the reactor's response in a prompt supercriticality regime. Reactivity steps ranging from 100 (delayed supercritical) to 1000 *pcm* (prompt supercritical) are simulated, the results of which are shown in Figure 6.3.

In the cases of 500 and 1000 *pcm* reactivity insertions, the reactor is in a prompt supercritical state and the initial power peaks reached during the transient are much more marked than in the cases of 100 and 200 *pcm* insertions. Compared to a ramp insertion of 500 and 1000 *pcm*, even a rapid insertion like in 0.1 *s* shown in Figure 6.1, step reactivity insertions result in a faster and higher initial power peak. Since the insertion does not continue over time, there are no oscillations during the first instants of the transient, unlike what happened in scenarios with ramp insertions. For larger reactivity insertions, the temperature increase is greater, leading to stronger negative reactivity feedback that rapidly brings the reactor power close to its initial value.

Subsequently, the power tends to stabilise for a short time interval, creating a plateau. Once again, after the plateau, oscillations in power and reactivity begin to occur in relation to the circulation time of the salt in the fuel circuit. The final temperature evolution toward the new steady state reflects the principle introduced in the previous case, where the average salt temperature in the critical region increase proportionally to the external reactivity insertion and do not depend on the insertion rate. Therefore, the values observed with the 500 and 1000 *pcm* reactivity insertions are consistent with those observed in the previous analised ramp scenarios.

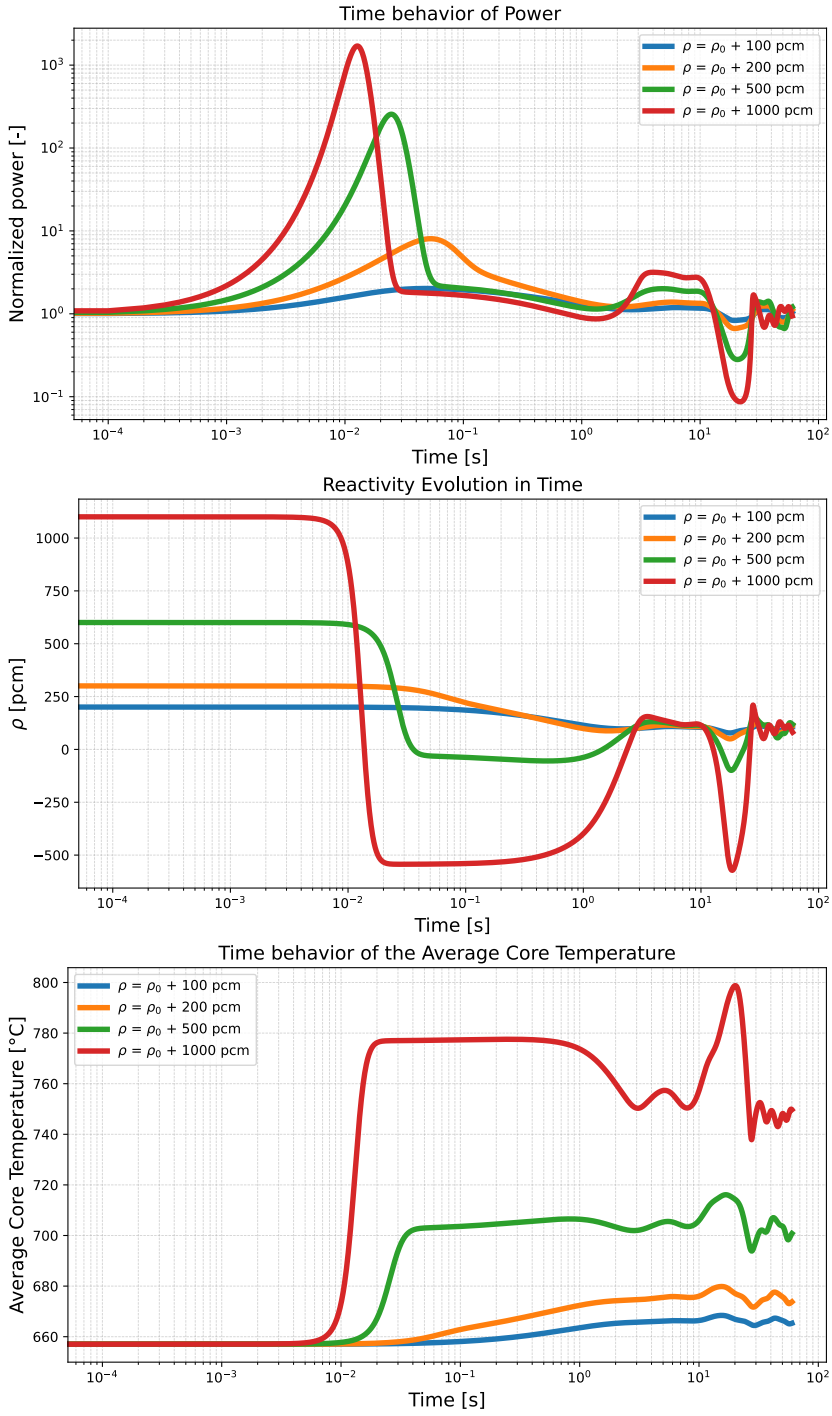

Figure 6.3: Transient behaviour for step reactivity insertions in Thorizon One model. Top panel: normalized power; Middle panel: reactivity; Bottom panel: average core temperature.

Reactor stability at zero-power

A zero-power reactor refers to the operating condition of the reactor in which nuclear heat generation is negligible. This condition is characterised by a very low power level $P(t)$, which ensures that temperature perturbations, which would normally lead to reactivity feedback, are irrelevant. Simulating a reactor at zero-power is important because it allows the study of its fundamental neutronic and dynamic behaviour isolating them from thermal-hydraulic feedback effects.

The analysis now focuses on evaluating the stability of the perturbed reactor starting from two different initial power levels:

- Nominal power of 249.1 $\mathrm{MW_{th}}$
- Zero-power of 249 $\mathrm{kW_{th}}$

The zero-power reactor corresponds to 0.1% of the nominal power. The transient on which the analysis is based is a reactivity initiated accident, specifically a reactivity insertion ranging from 500 to 3000 *pcm* occurring over a 0.1 *s* ramp.

The variation in reactor response at zero-power and nominal power is illustrated in Figure 6.4. Whether the reactor was at nominal power or zero-power condition, the overall heat transfer coefficient of the primary heat exchanger was always considered constant and equal to the nominal value. A more in-depth study should consider how this coefficient varies with load, but this is beyond the scope of this work.

The behaviour to be highlighted is that with the reactor starting at zero-power, it will take longer for the deposited power to be sufficient to cause a temperature change and and therefore trigger the corresponding reactivity feedback mechanism. Conversely, if the initial power level is higher, the increase in power causes a rapid increase in the temperature of the fuel salt, and the resulting feedback mechanisms act to limit the power peaks. This difference explains the shift between the power peaks shown in Figure 6.4.

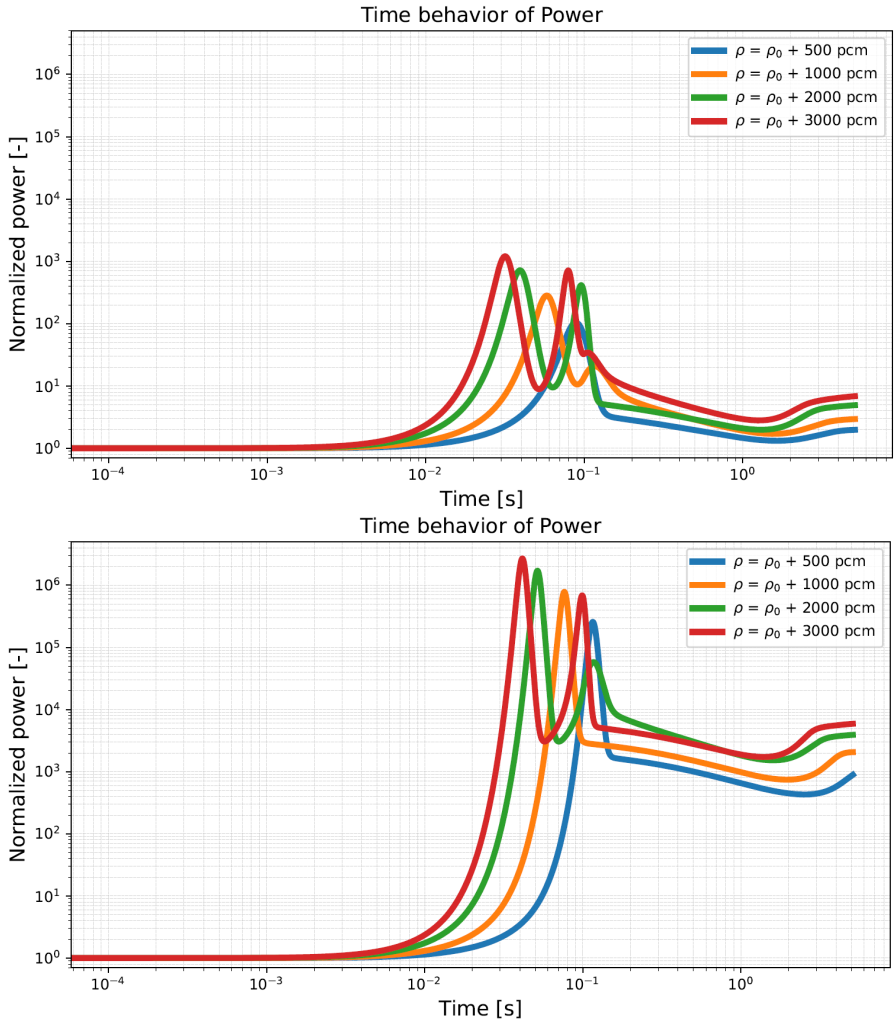

Figure 6.4: Evolution of normalised power for ramp reactivity insertions in 0.1 s in Thorizon One model at different power levels. Top panel: reactor initially at 249.1 MW_{th}; Bottom panel: reactor initially at 249 kW_{th}.

6.2.1 Fuel salt compressibility analysis

The model developed assumes that the fuel salt is incompressible, with the density law directly dependent only on the temperature variable, as shown in Section 4.2. Although all real fluids are compressible, liquid flows are generally considered incompressible because the density of liquids varies minimally with pressure, and because pressure waves travel through the system at very high speed. The latter is the speed of sound in the fluid, which for the fuel salt mixture is approximately equal to 1500 m/s [43]. The time required for pressure waves to propagate is often negligible compared to the characteristic time of the transient event, and propagation is therefore assumed to be instantaneous. However, when very rapid transients occur, such as those leading to prompt supercriticality, the characteristic times of the event become comparable to the pressure wave propagation time. In these specific scenarios, approaches that neglect fuel compressibility can underestimate power excursions [48], due to a delay in the density/void reactivity feedback mechanism. This is due to the fact that the density/void feedback mechanism would act with a certain delay related to wave propagations, and no longer at the same time scale of the Doppler effect.

In Section 3.1.2, it has been introduced how the Doppler effect and density/void feedback are the main feedback mechanisms in MSR concepts. The Doppler effect acts promptly with every change in fuel temperature, while density/void feedback acts according to the finite time that pressure waves take to propagate through the reactor core [48]. Only if the fluid is treated as incompressible the density of the salt is instantly correlated to its temperature, as if the speed of sound in the fluid were infinite.

The aim now is to assess whether the incompressibility assumption is valid or not at every moment of the scenarios analysed. The flow will be considered incompressible if:

$$\delta rho \ll rho \rightarrow \frac{\delta rho}{rho} \ll 1 \tag{6.1}$$

Assuming that changes along a pressure wave occur in an isentropic manner (adiabatic and internally reversible), the speed of sound in a continuous

substance can be defined as [49]:

$$c^2 = \left.\frac{\partial p}{\partial rho}\right|_s \tag{6.2}$$

where c is the speed of sound and p is the pressure. This relationship remains valid if we assume that the velocity and temperature gradients across the wave are very small, so that the wave can be considered an internally reversible process. Furthermore, since the temperature gradient at the sides of the wave is minimal, the process can be considered adiabatic [49].

Equation (6.1) can be rewritten by explicitly defining δrho in relation to Equation (6.2). Therefore, the criterion according to which the fluid can be considered incompressible becomes [43]:

$$\frac{\delta p}{rho \cdot c^2} \ll 1 \tag{6.3}$$

The code developed does not resolve the pressure in the individual finite volumes, so it is necessary to estimate the pressure variation δp. This is done in relation to the highest temperature derivative calculated in the entire core at each time step, according to the following expression [43]:

$$\delta p = \frac{\alpha}{\kappa_T}\frac{dT}{dt}t_c \tag{6.4}$$

where α is the fuel salt thermal expansion coefficient $[K^{-1}]$, κ_T is the isothermal compressibility of the fuel salt $[Pa^{-1}]$, and t_c is the characteristic time of the physical phenomenon. For the composition of the chloride salt hypothesised for Thorizon One, the thermal expansion coefficient is assumed to be $\alpha = -2.8E-4\ K^{-1}$ [43], while the isothermal compressibility, for a temperature of approximately 1000 K and a fraction of UCl_3 of 40%, is assumed to be $\kappa_T = 1.47E-10\ Pa^{-1}$ [50]. The characteristic time t_c is related to the expansion phenomena in the core, and is therefore calculated based on the axial length of the core and the speed of sound as $t_c = L_{core}/c$.

The approach used to test under which conditions the incompressible fluid assumption no longer holds focused on reactivity ramp insertions rather

than step insertions, as the former are more realistic. Specifically, several transients were implemented, all characterised by a reactivity insertion of 2000 *pcm*, but with different insertion times. It is assumed that the compressible phase must be modeled when the calculation of the criterion exceeds the arbitrary threshold value of 0.01. What has been noted is that the criterion is not met only when the ramp insertion time becomes so low that it is similar to a step and physically unrealistic. This is shown in the bottom panel of Figure 6.5, which refers to a reactivity ramp in 0.04 *s*. The results obtained suggests that the assumption of incompressible fluid adopted in the model is reasonable.

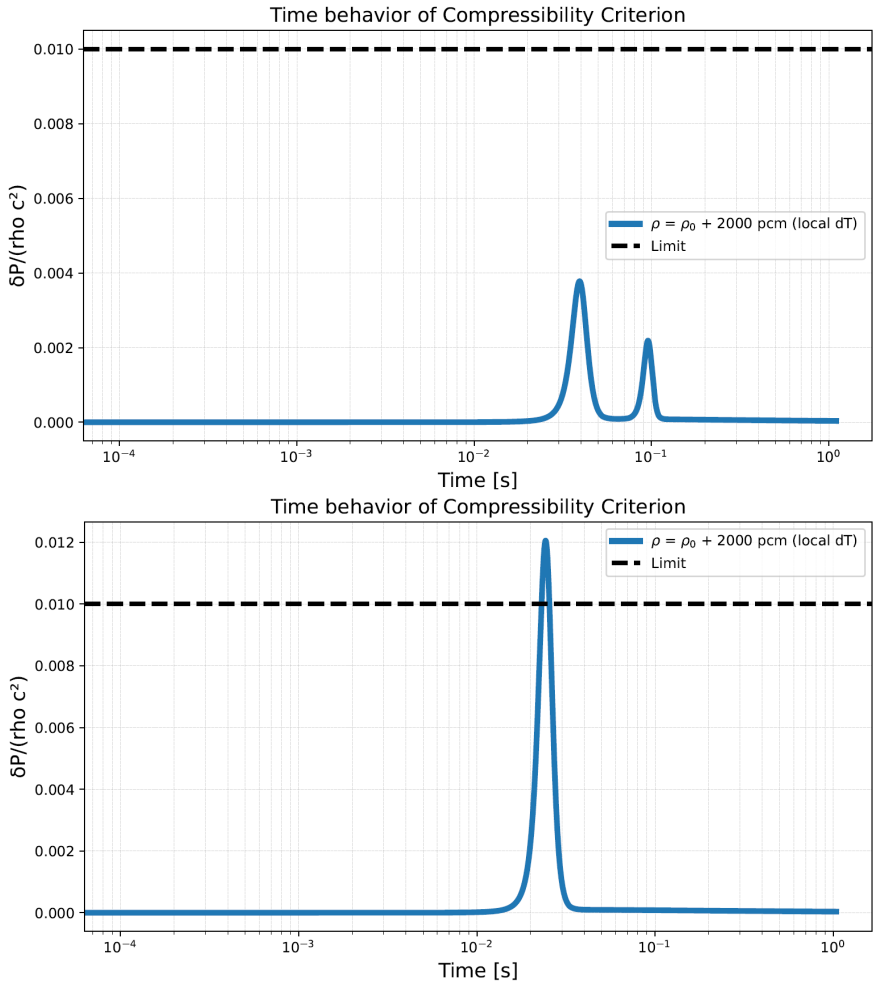

Figure 6.5: Verification of the compressibility criterion during a reactivity initiated accident in Thorizon One model. Top panel: insertion of 2000 *pcm* in 0.1 *s*; Bottom panel: insertion of 2000 *pcm* in 0.04 *s*.

6.3 Loss of heat sink

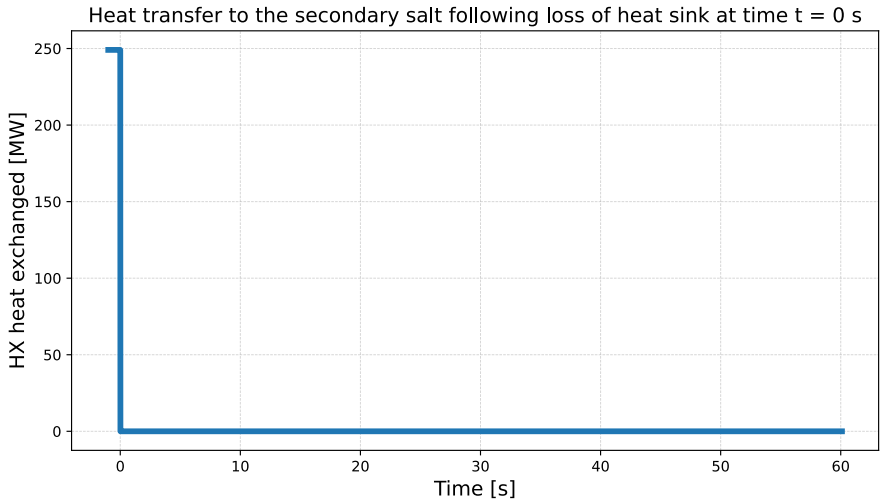

Figure 6.6: Evolution of heat removal capacity during a loss of heat sink transient in Thorizon One model under nominal conditions.

This scenario may occur due to failures in the secondary cooling system that compromise its ability to effectively remove heat, for example following a loss of secondary cooling salt.

To simulate the worst-case scenario, the loss of cooling capacity in the heat exchanger is assumed to be total and instantaneous, occuring at time $t = 0\ s$, as shown in Figure 6.6. Time $t = 0\ s$ marks the start of the transient, while at the previous instants the system was in nominal steady-state conditions. The results obtained using the developed code are shown in Figures 6.7 and 6.8.

Following the loss of heat removal, there is a gradual increase in the temperature of the primary salt leaving the heat exchanger, indicated as $T_{hx,out}$ in the lower panel of Figure 6.8. The hottest salt leaving the primary exchanger reaches the inlet of the core after a transit time of ~ 1 second along the cold leg. At this point, the average core temperature begins to rise, and negative reactivity feedback occurs. Following the decrease in total reactivity, the power level decreases and, consequently, the outlet core temperature ($T_{core,out}$) decreases compared to the steady-state value. At

time $t \sim 10\ s$ (consistent with the transit time through the out-of-core region), the temperature of the fuel salt at the inlet of the core becomes equal to the steady-state outlet core temperature. However, at the same instant $T_{core,out}$ is lower as a result of the decrease in power level. After the hotter fuel salt at the inlet had flowed through the core, the core outlet temperature rises again, while the inlet core temperature ($T_{core,in}$) decreases consistently with the decrease that $T_{core,out}$ had undergone as a result of the decrease in power.

The temperature in the primary circuit increases gradually over time, approaching a new equilibrium with a homogeneous temperature distribution. Due to the circulation of fuel salt, this progression occurs with the average temperature of the salt in the core oscillating, as shown in the top panel of Figure 6.8, causing the reactivity to oscillate towards more or less net negative values, illustrated in the bottom panel of Figure 6.7. The power level also fluctuates as a result, but its overall trend is decreasing, reaching approximately 2% of the initial steady-state power level one minute after the start of the transient. It should also be noted that the model considers all the walls of the circuit to be adiabatic and the current model does not consider the effect of decay heat. The latter refers to the heat generated by the decay of fission products and actinides in the fuel salt, which would further increase the temperature of the fuel salt in the transient and lead to a more rapid and marked drop in power.

In general, it can be seen that, in the event of unprotected loss of heat sink, the behaviour of the reactor demonstrates its intrinsic stability. The primary safety feature derives from the strong reactivity feedback linked to the fuel salt temperature.

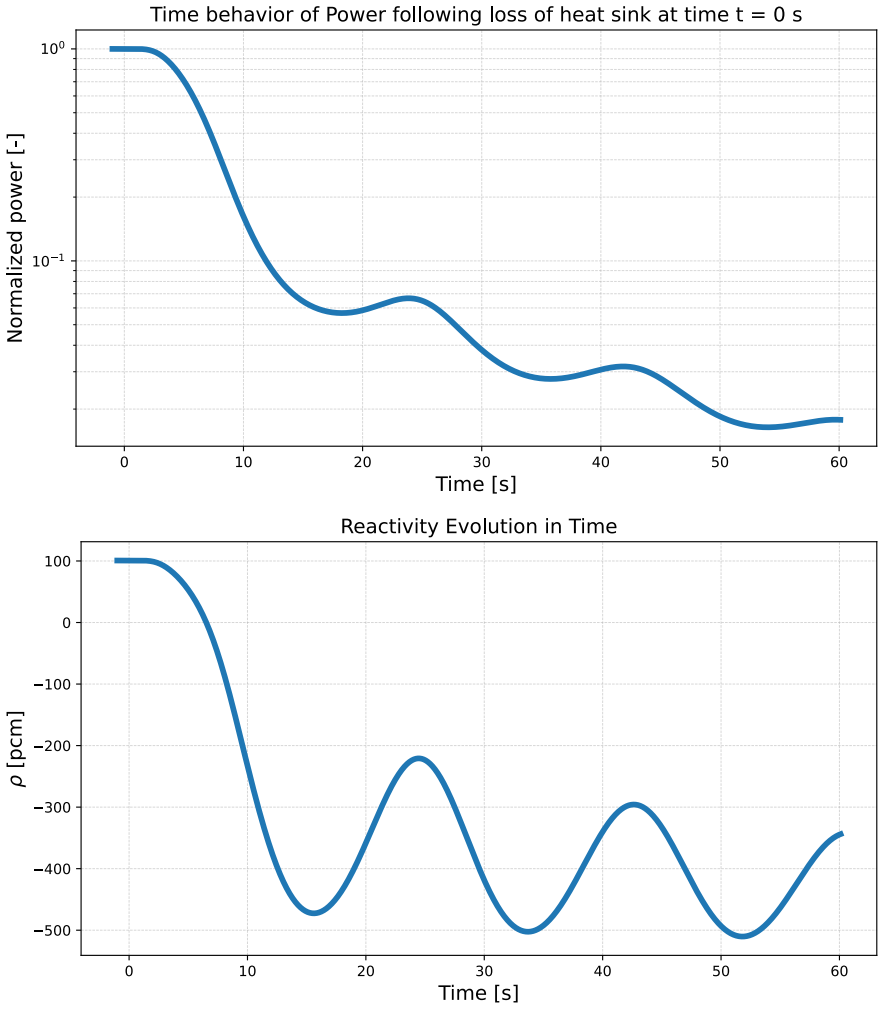

Figure 6.7: Evolution of normalised power and reactivity following an unprotected loss of heat sink in Thorizon One model. Top panel: normalized power; Bottom panel: reactivity.

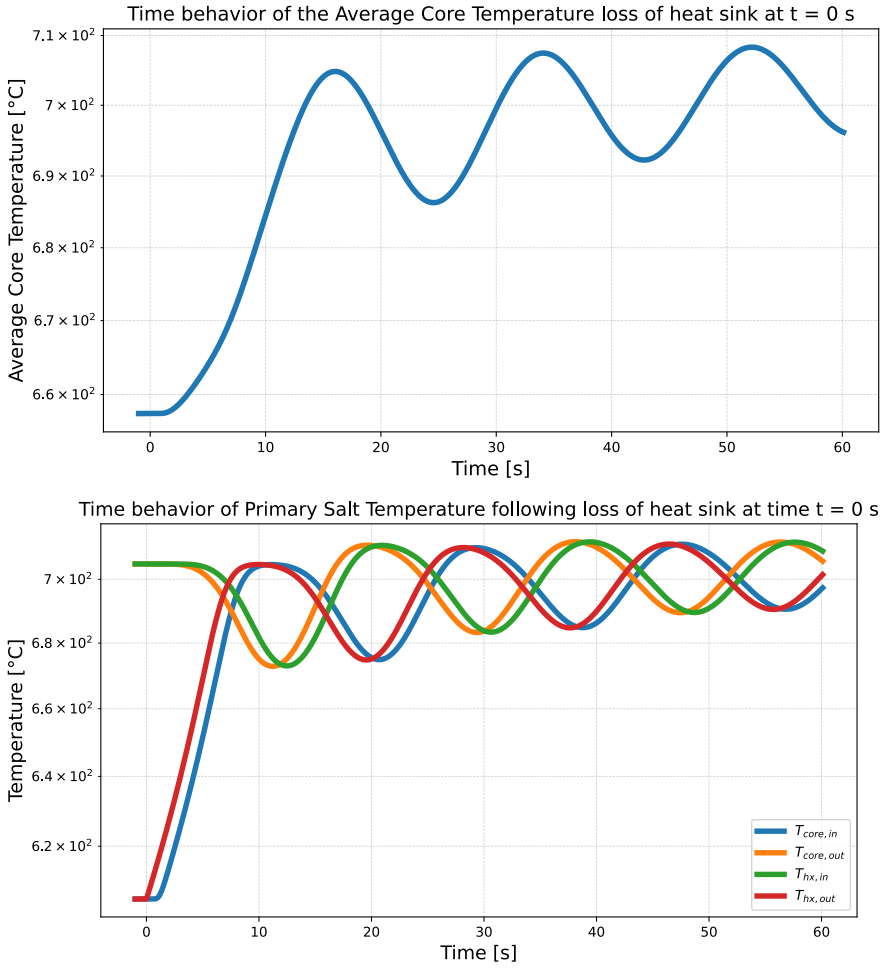

Figure 6.8: Evolution of fuel salt temperature following an unprotected loss of heat sink in Thorizon One model. Top panel: average core temperature; Bottom panel: fuel salt temperatures in the circuit (core and heat exchanger inlet/outlet temperatures).

6.4 Fuel-pump driven transients

This section studies and simulates pump-driven transients to understand the consequences of fuel flow variations on reactor power. Two types of transients are investigated:

- Pump startup: occurs when the speed of the fuel pumps is increased to the nominal speed.

- Pump coast-down: occurs when, starting from steady-state flow conditions, each pump is switched off.

The model developed implements these transients assuming that the total fuel flow rate is regulated by a single pump, located upstream of the core. The mass flow rate entering the core varies, depending on the selected scenario, following a sigmoid start-up profile or an exponential coast-down. The perturbation begins at the inlet interface of the core, and the mass flow rates at the subsequent interfaces are adjusted according to the continuity law shown in Section 4.2.

The transients are conducted with the reactor at zero-power (249.1 kW_{th}), where temperature and reactivity feedback effects do not play a role. The fuel salt temperature in the initial configuration is approximately 650 C throughout the whole primary circuit. Since the characteristic curves of the actual pumps are not available, the study will consider a short pump time constant and focus on the behaviour of the reactor's key parameters over a interval of 25 s. The aim is to highlight and emphasise the phenomena that affect the behaviour of circulating fuel reactors and Thorizon One, while recognising the need for further analysis.

The physical reason why flow variations affect the reactor response is related to the liquid fuel in circulation. The reactor dynamics in these scenarios are mainly determined by the evolution of the DNP concentration in the core during the flow transient.

Unprotected fuel-pump coast-down at zero-power

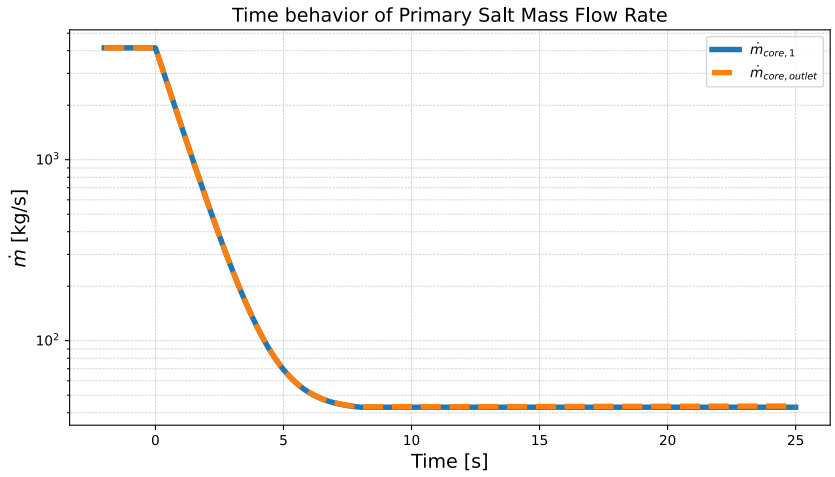

Figure 6.9: Evolution of the fuel mass flow rate in the core during the pump coast-down transient in Thorizon One model at zero-power.

The mass flow rate begins to vary at $t = 0$ s and drops rapidly with an exponential profile and a characteristic time constant of $\sim$1 s. Approximately 8 seconds after the start of the perturbation, the fuel salt flow drops to 1% of the nominal value, as shown in Figure 6.9, where $\dot{m}_{core,1}$ represents the mass flow rate at the first interface after the core inlet and $\dot{m}_{core,outlet}$ represents the mass flow rate at the core outlet interface. The results of this transient scenario are shown in Figures 6.10 and 6.11.

As the flow rate decreases, the DNP-drift effect decreases and therefore the concentration for each of the eight precursor groups in the core increases, as shown in the lower panel of Figure 6.11. The increase in DNP concentration in the critical region results in an increase in the power level. The latter, combined with the increase in salt transit time through the core, causes a gradual and slight increase in the average salt temperature in the core, which introduces negative feedback on reactivity and causes it to decrease. However, since the reactor is at zero-power, the power increase is not strong enough to cause a significant increase in temperatures in the short term, and the reactivity feedback is not strong enough to stabilise the reactor in the time interval analysed.

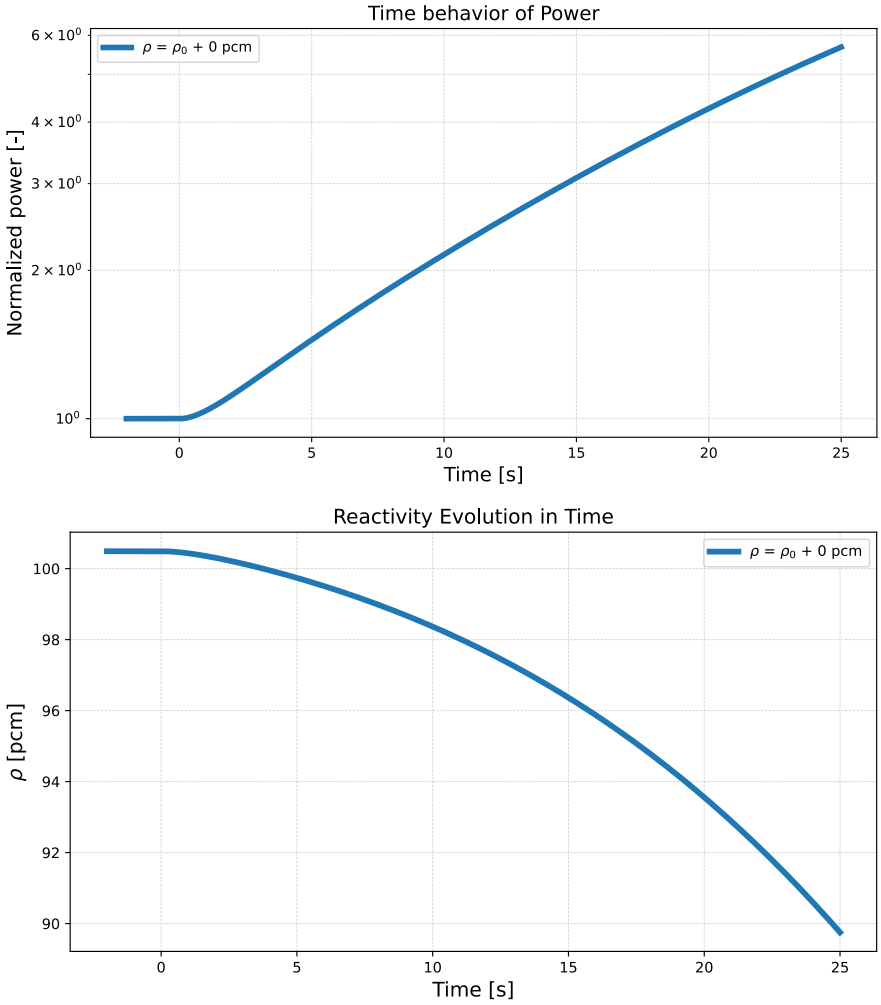

Figure 6.10: Evolution of normalised power and reactivity following an unprotected pump coast-down in Thorizon One model at zero-power. Top panel: normalized power; Bottom panel: reactivity.

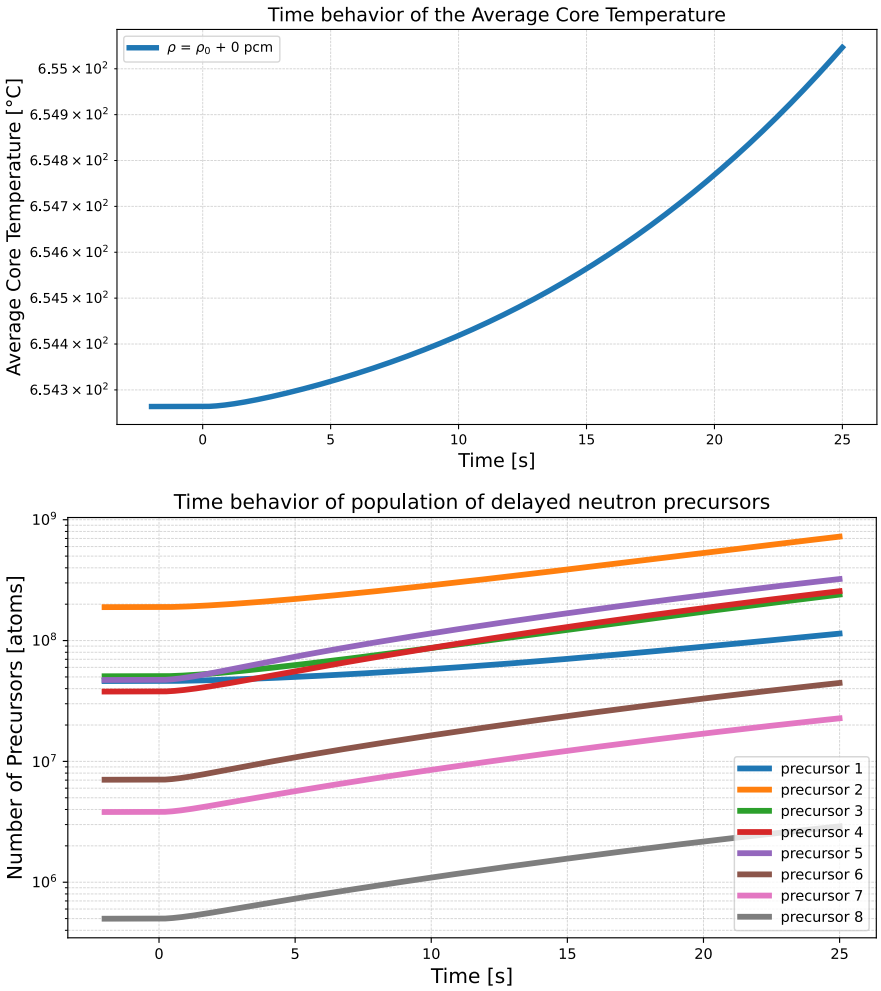

Figure 6.11: Evolution of average salt temperature and precursors concentration in the core following an unprotected pump coast-down in Thorizon One model at zero-power. Top panel: average core temperature; Bottom panel: delayed neutron precursors concentration.

Unprotected fuel-pump startup at zero-power

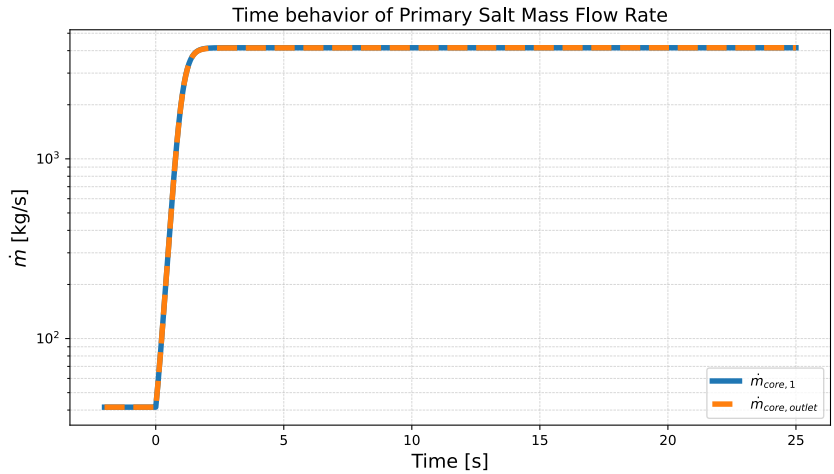

Figure 6.12: Evolution of the fuel mass flow rate in the core during the pump startup transient in Thorizon One model at zero-power.

The flow rate increases starting from $t = 0$ s and following a sigmoid profile, with a characteristic time constant of $\sim$1 s. The trend is illustrated in Figure 6.12, where it can be seen that the increase from the initial flow rate, equal to 1% of the nominal value, to the nominal flow rate takes place in approximately 3 seconds. The response of the Thorizon One reactor estimated by the code developed is shown in Figures 6.13 and 6.14.

As the flow rate increases, the flow of delayed neutron precursors out of the core increases. This causes a decrease in the power and average temperature of the salt in the core. The decrease in salt temperature relative to the steady-state reference value causes a positive reactivity insertion. The reactivity of the system increases accordingly, but since the temperature variation is very limited with the reactor at zero-power, it is the loss of precursors that plays the main role in determining the evolution of the power level. In the bottom panel of Figure 6.13, note that the steady-state reactivity was approximately 4.7 *pcm*, much lower than the 100.62 *pcm* obtained under nominal flow conditions. This is due to the fact that, with a low initial mass flow rate, the transit time of the salt through the core is very high, with minimal DNP-drift. As a result, the compensation reactivity to ensure steady-state conditions ρ_0 is very low.

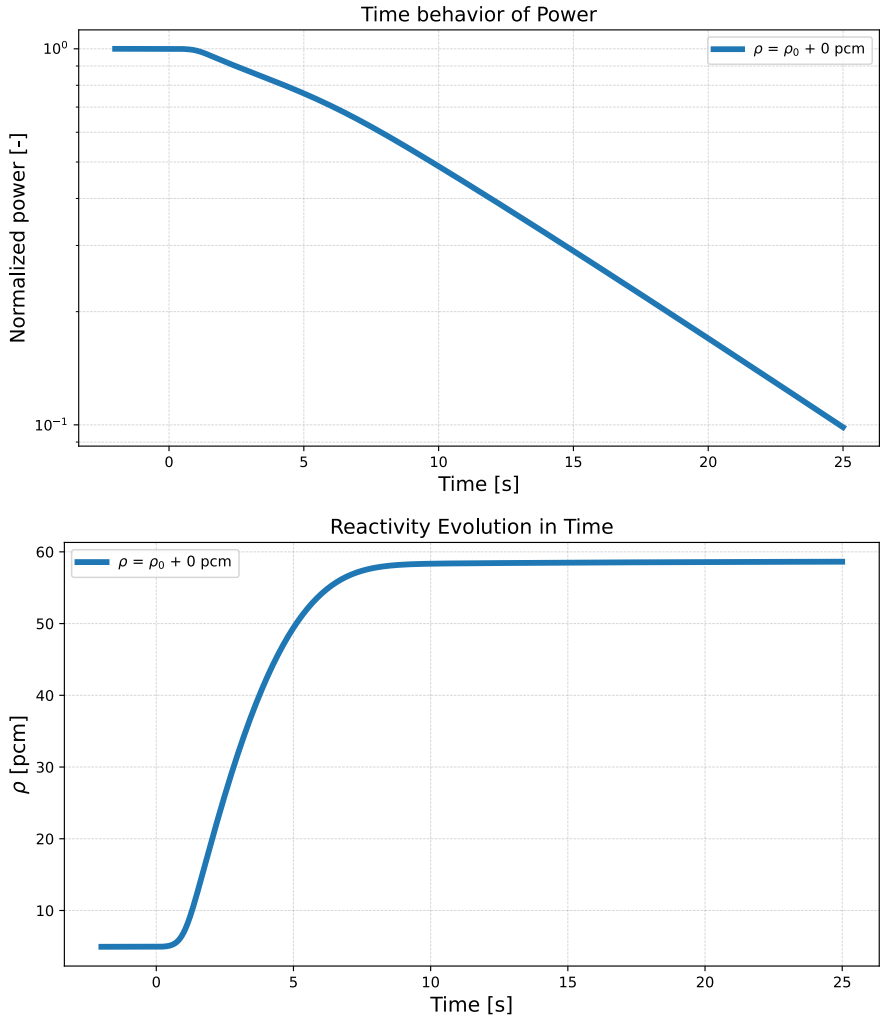

Figure 6.13: Evolution of normalised power and reactivity following an unprotected pump startup in Thorizon One model at zero-power. Top panel: normalized power; Bottom panel: reactivity.

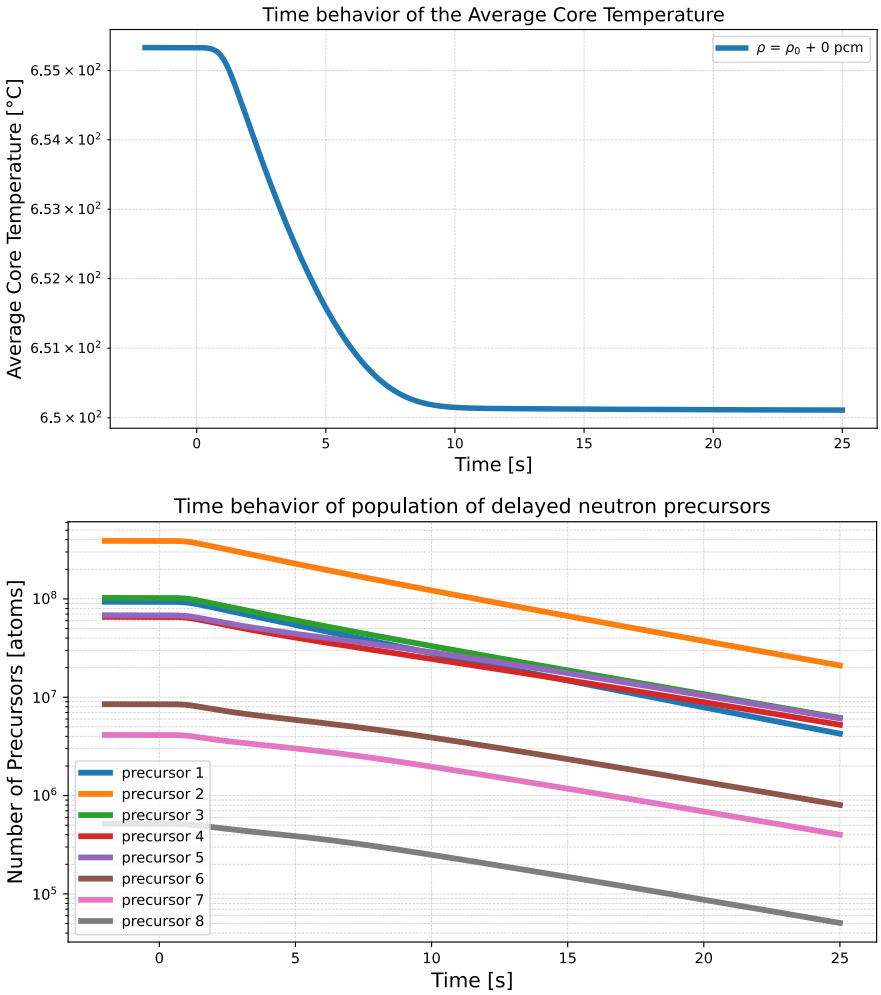

Figure 6.14: Evolution of average salt temperature and precursors concentration in the core following an unprotected pump startup in Thorizon One model at zero-power. Top panel: average core temperature; Bottom panel: delayed neutron precursors concentration.

6.5 Preliminary Sensitivity Analysis

This section presents a preliminary sensitivity analysis aimed at identifying the parameters that most influence the behaviour of the reactor. Simplified models, such as the one developed during this thesis, are well-suited to performing this type of analysis while keeping computation times low.

The approach used involves varying only one parameter at a time between consecutive simulations of the same transient, while all other parameters remain equal to the nominal conditions. The transient used for the analysis consists of discrete ramp reactivity insertions from 500 to 3000 pcm in 0.1 s. The parameters investigated are design parameters, which reflect the design choices and the initial operating conditions.

Mass flow rate sensitivity analysis

A change in the nominal fuel salt flow rate leads to a change in the temperature difference between the core inlet and outlet ΔT_{core}. The different values of ΔT_{core} that characterise the different operating conditions are chosen in advance and, based on the relationship with the thermal power generated shown in equation 6.5, the different mass flow rates are defined. These are summarised in Table 6.3.

$$\dot{m} c_p \Delta T_{core} = P \tag{6.5}$$

The results of the analysis are shown in Figure 6.15. Since different mass flow rates imply different transit times, these translate into different compensation reactivity ρ_0 according to Equation 4.20 for each operating configuration. To better understand how operating conditions affect the reactor's response to perturbations, the total reactivity ρ, shown in the lower panel of Figure 6.15, is normalised with respect to ρ_0. From this analysis, it can be seen that the design mass flow rate seems to have a marginal effect on the dynamic behaviour of the reactor. All markers relating to the various parameter values overlap, apart from a few minor discrepancies. The steady-state average core temperature varies with the design mass flow rate, but the transient behaviour following the perturbation is comparable in all cases.

Table 6.3: Mass flow rates $\dot{m}$ values for each ΔT_{core} analyzed

$\dot{m}$ [kg/s]	ΔT_{core} [C]	P [MW_{th}]
3321	125	249.1
4152	100	249.1
4613	90	249.1

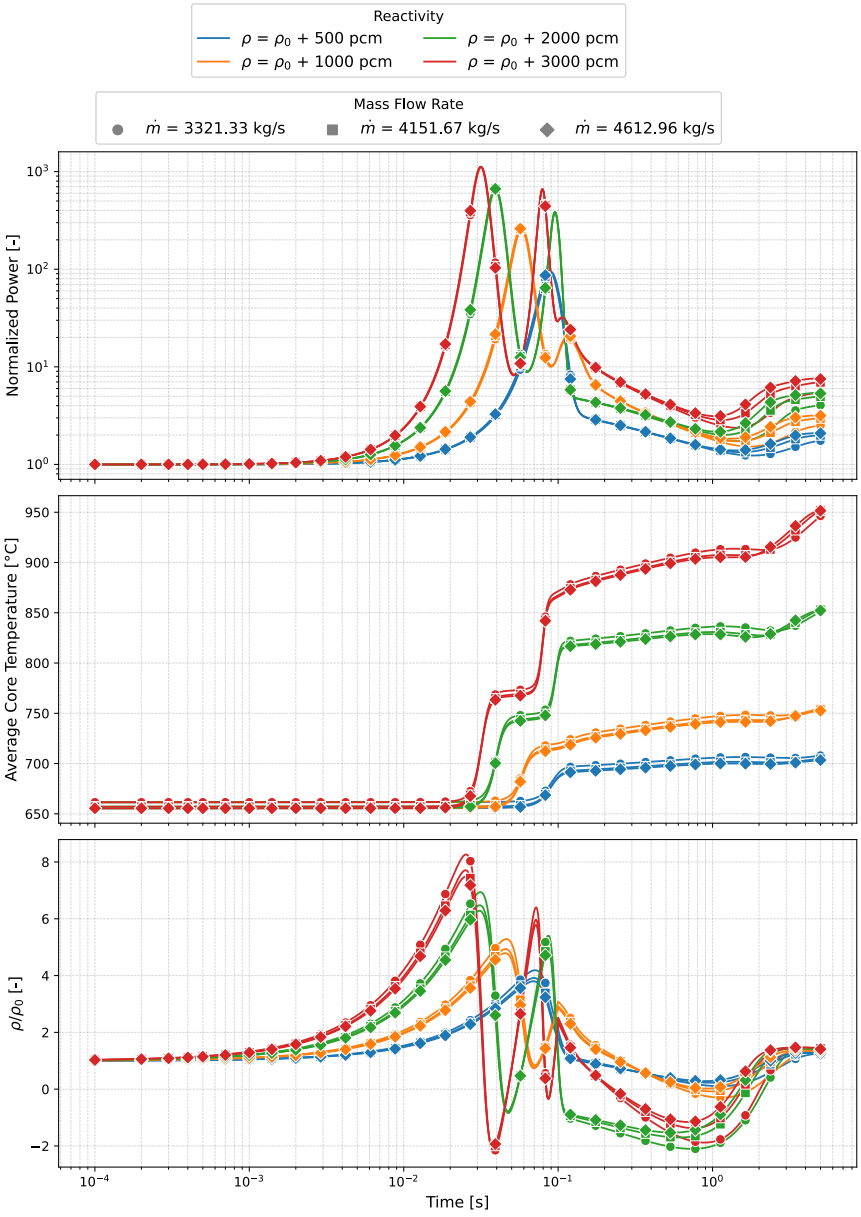

Figure 6.15: Transient behaviour in Thorizon One model for ramp reactivity insertions over 0.1 s: effect of nominal mass flow rate.

Core length sensitivity analysis

Figure 6.16 shows the main results obtained by simulating different reactivity insertion ramps in 0.1 s in a model that assumes a different core size each time. Five core lengths are considered, ranging from 1 m to 2.6 m, with increments of 0.4 m. This parameter reveals the role of the size of active regions during accidents.

In this case, the behaviour of the reactor varies quite significantly with a different core size. The evolution curves of the main reactor parameters now appear less clustered than in the previous analysis. The first clarification to be made is that the variation in length of the core with a constant cross-section results in a different transit time through this component for each configuration. The variation in transit time has the direct consequence that the compensation reactivity for DNP loss and to allow steady-state condition ρ_0 is different for each configuration, where a larger core requires less compensation reactivity. To facilitate comparison between the different cases, the lower panel of Figure 6.16 shows the evolution over time of reactivity ρ, normalised with respect to ρ_0. The graph shows that, although a larger core results in a lower ρ_0, a larger active region size still produces the highest reactivity peak during the transient. This indicates that the severity of the event does not simply depend on the sum of the externally inserted reactivity ρ_E and steady-state compensation reactivity ρ_0. Since feedback effects come into play during the transient, these are what strongly influence the behaviour of the reactor.

A larger core means that the mass of fuel salt contained within it increases in relation to the greater volume of the component. Following the reactivity insertion, the power of the reactor increases, causing a corresponding increase in the temperature of the fuel salt. However, the power required to heat the volume of salt contained in the core will be greater for a larger core size. As the core size increases, reactivity feedback comes into play with some additional delay due to the thermal inertia of the salt, and higher power peaks occur with the same reactivity insertions.

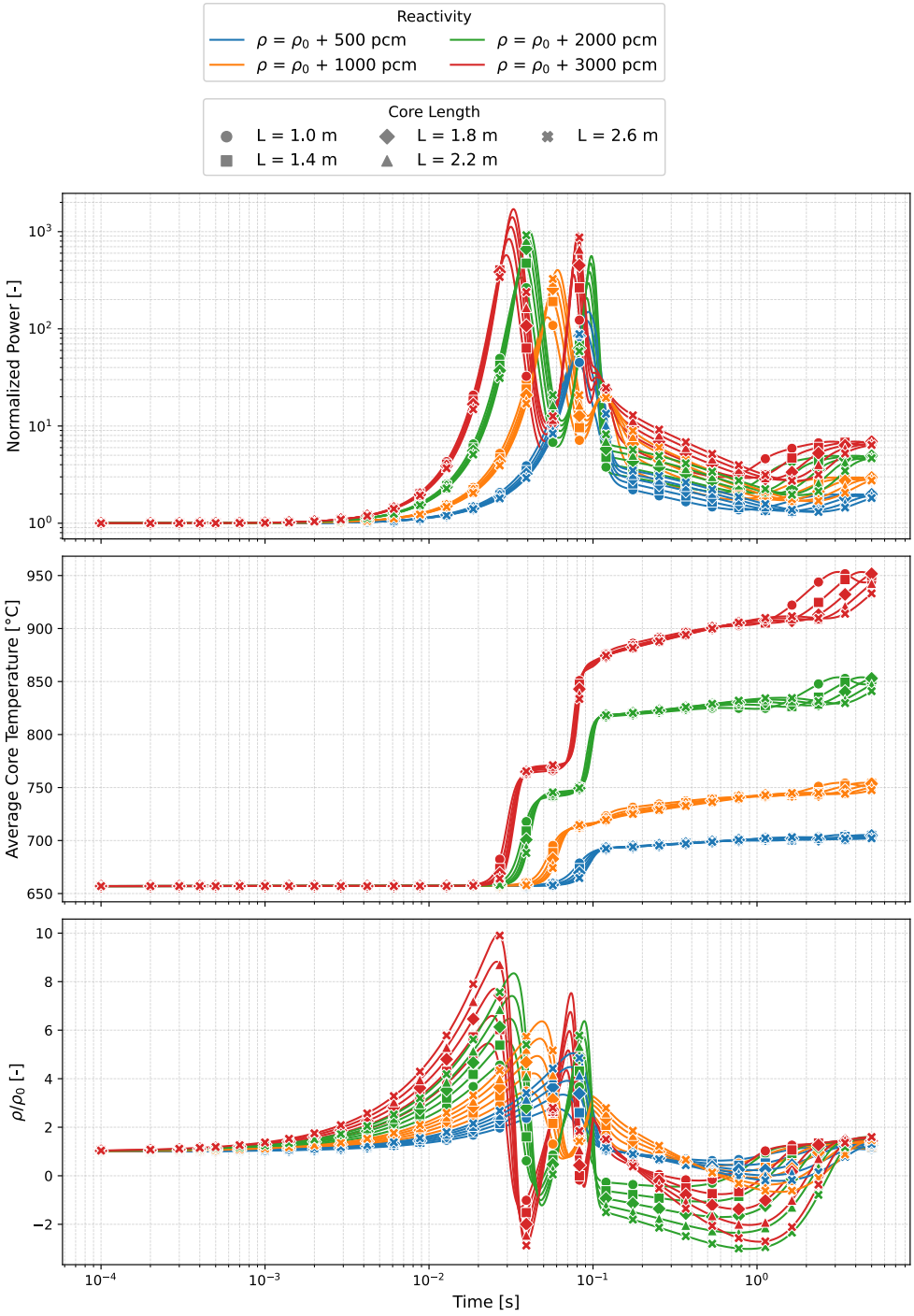

Figure 6.16: Transient behaviour in Thorizon One model for ramp reactivity insertions over 0.1 s: effect of core length.

Chapter 7

Conclusions and Future Work

The modeling of liquid-fuel molten salt reactors involves the simulation of specific phenomena, in particular the effects related to the drift of delayed neutron precursors. This thesis described the development of a parametric and multiphysics code in Python. The model combines a modified and improved point kinetic module with a simplified 1D thermal-hydraulic description of the primary circuit to study the phenomena associated with fuel circulation.

The code was verified through a grid convergence analysis and a numerical benchmark. The MSFR, developed in the Euratom EVOL and SAMOFAR projects, was selected for the verification phase. The TFM-OpenFOAM multiphysics tool has demonstrated that simplified models, such as LiCore, can reasonably reproduce the order of magnitude of transients in MSFR. Comparison with these models and with MOSAICS has confirmed that the code developed in this thesis is suitable for characterizing the dynamic behaviour of the Thorizon One reactor.

Several accidental transients were simulated and analyzed to study the dynamics of the Thorizon One concept. The model allows to observe oscillations related to thermal salt inertia, feedback mechanisms and fuel salt circulation time. It can be concluded that the reactor exhibits excellent

transient behaviour in terms of stability, as the strong reactivity feedback linked to the salt temperature rapidly reduces significant power excursions. Inherent safety and stability is one of the main advantages of molten salt reactors. However, the high final temperatures reached during severe transients must be carefully monitored, as they may affect the reactor's safe operation over time.

The model assumes that the fluid is dilatable but incompressible, which implies that the density/vacuum feedback mechanism acts on reactivity on the same time scale as the Doppler effect. This assumption was verified for the entire duration of critical transients by estimating the pressure variation based on the maximum salt temperature variation in the core and applying the criterion that the incompressibility assumption is no longer valid if $\frac{\delta p}{rho \cdot c^2} > 0.01$.

The model allows relatively rapid estimates of reactor's transient responses, which can be particularly useful during the design phase. The computational cost is relatively low, requiring approximately one minute to simulate several seconds of a reactivity insertion. A preliminary sensitivity analysis of key reactor design parameters revealed the significant role of core size. Larger cores result in higher power peaks in any reactivity insertion transients, with reactivity feedback coming into play with a certain delay due to the thermal inertia of the salt.

Further development and analysis will be necessary in the future to improve the model in order to describe coupled transients and make it suitable for new sensitivity studies. The thermal-hydraulic module can be extended to include heat transfer by radiation and the effects of decay heat.

In conclusion, the tool developed during this thesis can provide valuable insights into the complex interactions that drive the dynamics of the Thorizon One reactor and circulating fuel reactor concepts in general. The important aspect is that the code developed provides the Thorizon startup with a verified, low-computational-cost tool capable of reliably estimating the evolution of key reactor parameters under transient conditions.

Bibliography

[1] Thomas J. Dolan, ed. *Molten Salt Reactors and Thorium Energy*. Cambridge, UK: Woodhead Publishing, 2017. DOI: 10.1016/B978-0-08-101126-3.00001-4. URL: https://www.sciencedirect.com/book/9780081011263/molten-salt-reactors-and-thorium-energy (cit. on pp. 1, 2, 16–18, 23, 47).

[2] Generation IV International Forum (GIF) / OECD Nuclear Energy Agency. *Technology Roadmap Update for Generation IV Nuclear Energy Systems*. https://www.gen-4.org/gif/upload/docs/application/pdf/2014-03/gif-tru2014.pdf. 2014 (cit. on p. 1).

[3] Elsa Merle-Lucotte, Michel Allibert, Delphine Gérardin, Daniel Heuer, Axel Laureau, et al. *Design and Safety Studies of the Molten Salt Fast Reactor Concept within the SAMOFAR Project*. https://lpsc.in2p3.fr/wp-content/uploads/2025/01/EMerle-MSFR-SAMOFAR-WP1_GIF2018_Article-final.pdf. 2018 (cit. on pp. 2, 59).

[4] Stellaria. *TheStellarium Reactor*. URL: https://www.stellaria.fr/en/ (cit. on p. 2).

[5] Elsa Merle et al. *Review of the EU MSR designs*. https://www.endurance-msr-project.eu/wp-content/uploads/2025/05/ENDURANCE_101164896_D1.1_Review-of-the-EU-MSR-designs_v2.1.pdf. 2025 (cit. on pp. 3–6, 9, 11–13, 59–61).

[6] NAAREA. *XAMR (eXtrasmall Advanced Modular Reactor)*. URL: https://www.naarea.fr/en/naarea-technology (cit. on p. 4).

[7] Thorizon. *Our Solution*. URL: https://thorizon.com/solution (cit. on pp. 5, 9).

[8] Thorizon. *Technology - Our Design*. URL: https://thorizon.com/technology (cit. on pp. 5, 9).

[9] Thorizon. *Development of the Thorizon One Molten Salt Reactor*. Presentation at Topsector Energie – Energy Talks. 2024. URL: https://topsectorenergie.nl/documents/1346/Sessie_2_Thorizon_Company_Presentatie.pdf (cit. on p. 10).

[10] Jiri Krepel. «Dynamics of Molten Salt Reactors». PhD thesis. Technical University of Prague, 2006. DOI: 10.13140/RG.2.1.4079.6326 (cit. on pp. 12, 58).

[11] Axel Laureau. *Développement de modèles neutroniques pour le couplage thermohydraulique du MSFR et le calcul de paramètres cinétiques effectifs*. https://tel.archives-ouvertes.fr/tel-01255350. 2015 (cit. on pp. 12, 35, 36, 58, 62, 63, 69, 75).

[12] G. I. Bell and S. Glasstone. *Nuclear Reactor Theory*. New York, NY: Van Nostrand Reinhold Company, 1970, pp. 465–466. URL: https://digital.library.unt.edu/ark:/67531/metadc870144/m2/1/high_res_d/4074688.pdf (cit. on pp. 15, 21–23).

[13] James J. Duderstadt and Louis J. Hamilton. *Nuclear Reactor Analysis*. John Wiley & Sons, 1976. URL: http://deepblue.lib.umich.edu/bitstream/2027.42/89079/1/1976_Nuclear_Reactor_Analysis.pdf (cit. on p. 16).

[14] John R. Lamarsh. *Introduction to Nuclear Reactor Theory*. Ithaca, NY: Addison-Wesley (for Cornell University Press), 1966. URL: https://bayanbox.ir/view/8512326620447390511/Introduction-to-Nuc-Reactor-Theory-John-R.-Lamarsh.pdf (cit. on pp. 16, 17).

[15] Nuclear-Power.com. *Mean Generation Time with Delayed Neutrons*. URL: https://www.nuclear-power.com/nuclear-power/fission/delayed-neutrons/mean-generation-time-with-delayed-neutrons/ (cit. on p. 17).

[16] U.S. Department of Energy. *DOE Fundamentals Handbook: Nuclear Physics and Reactor Theory, Volume 2 of 2*. 1993. URL: https://www.standards.doe.gov/standards-documents/1000/1019-bhdbk-1993-v2 (cit. on p. 18).

[17] Y. Oka and K. Suzuki. *Nuclear Reactor Kinetics and Plant Control*. Springer, 2013, pp. 4–7. DOI: 10.1007/978-4-431-54195-0. URL: https://doi.org/10.1007/978-4-431-54195-0 (cit. on pp. 18–20, 22).

[18] Daniel Rozon. *Introduction to Nuclear Reactor Kinetics*. CANTEACH / Canadian Nuclear, 1996, pp. 47–48. URL: https://canteach.candu.org/Content%20Library/20041802.pdf (cit. on p. 19).

[19] Daniel Rozon. *Introduction to Nuclear Reactor Kinetics*. CANTEACH / Canadian Nuclear, 1996, p. 77. URL: https://canteach.candu.org/Content%20Library/20041803.pdf (cit. on p. 23).

[20] A. F. Henry. «The Application of Reactor Kinetics to the Analysis of Experiments». In: *Nuclear Science and Engineering* 3 (1958), pp. 52–70 (cit. on p. 25).

[21] D. Wooten. «A Review of Molten Salt Reactor Kinetics Models». In: *Nuclear Science and Engineering* 191.3 (2018). DOI: 10.1080/00295639.2018.1479811. URL: https://www.osti.gov/servlets/purl/1479811 (cit. on pp. 32, 34).

[22] Elsa Merle-Lucotte, Daniel Heuer, Axel Laureau, Mariya Brovchenko, Michel Allibert, Manuele Aufiero, Véronique Ghetta, and Pablo Rubiolo. *Physical Assessment of the Load Following and Starting Procedures for the Molten Salt Fast Reactor*. 2015. URL: https://lpsc.in2p3.fr/wp-content/uploads/2025/01/ICAPP2015-15450-MSFR-final.pdf (cit. on pp. 32, 58, 62).

[23] C. Guerrieri, A. Cammi, and L. Luzzi. «An approach to the MSR dynamics and stability analysis». In: *Progress in Nuclear Energy* 67 (2013), pp. 56–73. DOI: 10.1016/j.pnucene.2013.03.020 (cit. on p. 33).

[24] David Lecarpentier and Vincent Carpentier. «Neutronic Program for Critical and Nonequilibrium Study of Mobile Fuel Reactors: The Cinsf1D Code». In: *Nuclear Science and Engineering* 142 (2002), pp. 1–14. DOI: 10.13182/NSE03-A2316 (cit. on p. 34).

[25] M. Mascaron, J. Martinet, V. Pascal, E. Merle, and F. Bertrand. «An approach to Molten Salt Reactor operation and control and its application to the ARAMIS actinide burner». In: *Annals of Nuclear Energy* 210 (2024), p. 110888. DOI: 10.1016/j.anucene.2024.110888 (cit. on p. 35).

[26] A. Laureau et al. «The LiCore Power Plant Simulator of the Molten Salt Fast Reactor». In: *EPJ Web of Conferences* 247 (2021), p. 06030. DOI: 10.1051/epjconf/202124706030 (cit. on pp. 35, 69).

[27] J. Křepel, U. Rohde, U. Grundmann, and F. Weiss. «DYN3D-MSR spatial dynamics code for molten salt reactors». In: *Annals of Nuclear Energy* 34.6 (2007), pp. 449–462. DOI: 10.1016/j.anucene.2006.12.011 (cit. on p. 36).

[28] H. K. Versteeg and W. Malalasekera. *An Introduction to Computational Fluid Dynamics: The Finite Volume Method*. Pearson Education, 2007, pp. 66–109, 146–149, 180–186. ISBN: 9780131274983. URL: https://lib.ugent.be/en/catalog/rug01:001266618 (cit. on pp. 36, 40, 42, 64).

[29] R. A. A. Saleem, T. Kozlowski, and R. Shrestha. «A solver for the two-phase two-fluid model based on high-resolution total variation diminishing scheme». In: *Nuclear Engineering and Design* 301 (2016), pp. 255–263. DOI: 10.1016/j.nucengdes.2016.03.015 (cit. on p. 42).

[30] P. Wu, F. Chao, D. Wu, J. Shan, and J. Gou. «Implementation and Comparison of High-Resolution Spatial Discretization Schemes for Solving Two-Fluid Seven-Equation Two-Pressure Model». In: *Science and Technology of Nuclear Installations* 2017 (2017), pp. 1–14. DOI: 10.1155/2017/4252975 (cit. on p. 42).

[31] *RELAP5/MOD3 Code Manual: Code Structure, System Models, and Solution Methods. Volume 1*. Idaho National Engineering Laboratory, U.S. Department of Energy, 1995. DOI: 10.2172/105079. URL: https://doi.org/10.2172/105079 (cit. on p. 42).

[32] G. Lavialle. *CATHARE V2.5_1 User's Manual*. SSTH/LDAS/EM. 2005 (cit. on p. 42).

[33] B. B. Koren. *A Robust Upwind Discretization Method for Advection, Diffusion and Source Terms*. Tech. rep. Department of Numerical Mathematics, CWI, 1993, pp. 1–21. URL: http://oai.cwi.nl/oai/asset/5293/05293D.pdf (cit. on p. 44).

[34] Steven C. Chapra and Raymond P. Canale. *Numerical Methods for Engineers*. 7th ed. New York, NY: McGraw-Hill Education, 2015, pp. 735–737. ISBN: 9780073397924 (cit. on pp. 44–46).

[35] F. Moukalled, L. Mangani, and M. Darwish. *The Finite Volume Method in Computational Fluid Dynamics*. Fluid Mechanics and its Applications. Springer, 2015. DOI: 10.1007/978-3-319-16874-6. URL: https://doi.org/10.1007/978-3-319-16874-6 (cit. on p. 44).

[36] M. A. Storti and J. Ferreri. *Numerical Methods in Nuclear Thermal Hydraulics*. Elsevier, 2024, pp. 83–138. DOI: 10.1016/b978-0-323-85608-9.00001-1. URL: https://doi.org/10.1016/b978-0-323-85608-9.00001-1 (cit. on p. 44).

[37] Jr. John D. Anderson. *Computational Fluid Dynamics: The Basics with Applications*. McGraw-Hill, 1995. ISBN: 0-07-113210-4 (cit. on p. 45).

[38] Patrick J. Roache. *Fundamentals of Verification and Validation*. Socorro, NM: Hermosa Publishers, 2009, pp. 46–52. ISBN: 9780913478127 (cit. on pp. 57, 58, 66).

[39] H. Rouch, O. Geoffroy, P. Rubiolo, A. Laureau, M. Brovchenko, D. Heuer, and E. Merle-Lucotte. «Preliminary thermal–hydraulic core design of the Molten Salt Fast Reactor (MSFR)». In: *Annals of Nuclear Energy* 64 (2013), pp. 449–456. DOI: 10.1016/j.anucene.2013.09.012 (cit. on pp. 60, 61).

[40] CFD University. *How to manage uncertainty in CFD: the grid convergence index*. 2025. URL: https://cfd.university/blog/how-to-manage-uncertainty-in-cfd-the-grid-convergence-index/ (cit. on pp. 64–68).

[41] Coleman HUGH & Committee Members. *ASME V&V 20-2009 Standard for Verification and Validation in Computational Fluid Dynamics and Heat Transfer*. ASME, 2009 (cit. on pp. 65–67).

[42] Ismail B. Celik, Urmila Ghia, Patrick J. Roache, and Christopher J. Freitas. «Procedure for Estimation and Reporting of Uncertainty Due to Discretization in CFD Applications». In: *Journal of Fluids Engineering* 130.7 (2008). DOI: 10.1115/1.2960953 (cit. on pp. 65–67).

[43] Thibault Le Meute, Frédéric Bertrand, Elsa Merle, Nathalie Marie, and Daniel Heuer. *Calculation of reactivity insertion in a generation IV Molten Salt Reactor*. https://www.samosafer.eu/wp-content/uploads/2022/06/LeMeute_Study-of-the-impact-of-compressibility-modelling-during-reactivity-inserti.pdf. 2020 (cit. on pp. 69, 75, 79, 89, 90).

[44] David Gerardin. «Développement de méthodes et d'outils numériques pour l'étude de la sûreté du réacteur à sels fondus MSFR». PhD thesis. Université Grenoble Alpes, 2018. URL: https://tel.archives-ouvertes.fr/tel-01971983 (cit. on p. 73).

[45] D. Zhang, S. Qiu, and G. Su. «Development of a Safety Analysis Code for Molten Salt Reactors». In: *Nuclear Engineering and Design* 239.12 (2009), pp. 2778–2785. DOI: 10.1016/j.nucengdes.2009.08.020. URL: https://doi.org/10.1016/j.nucengdes.2009.08.020 (cit. on p. 75).

[46] Thibault Le Meute, Frédéric Bertrand, Elsa Merle, Nathalie Marie, and Daniel Heuer. *Modélisation d'insertions de réactivité dans un réacteur de génération IV à sels fondus*. https://lpsc-indico.in2p3.fr/event/2667/attachments/4134/5647/Presentation_LeMeuteThibault.pdf. 2020 (cit. on pp. 78, 79).

[47] Mohammad Jaradat, Geun-Ho Yang, Hyeonseo Park, Won Sik Yang, Changho Lee, and Yoonsang Jung. *Multiphysics coupling of PROTEUS-NODAL and SAM for molten salt reactor simulation*. https://publications.anl.gov/anlpubs/2020/08/158813.pdf. 2020 (cit. on pp. 78, 79).

[48] E. Cervi, S. Lorenzi, A. Cammi, and L. Luzzi. «Development of a multiphysics model for the study of fuel compressibility effects in the Molten Salt Fast Reactor». In: *Chemical Engineering Science* 193

(2018), pp. 379–393. DOI: 10.1016/j.ces.2018.09.025 (cit. on p. 89).

[49] Steven S. Wassgren. *Notes on Thermodynamics, Fluid Mechanics and Gas Dynamics*. https://engineering.purdue.edu/~wassgren/notes/NotesOnThermodynamicsFluidMechanicsAndGasDynamics_Wassgren.pdf. 2021 (cit. on p. 90).

[50] D. A. Andersson and B. W. Beeler. «Ab initio molecular dynamics (AIMD) simulations of NaCl, UCl_3 and NaCl–UCl_3 molten salts». In: *Journal of Nuclear Materials* (2022). DOI: 10.1016/j.jnucmat.2022.153836. URL: https://www.sciencedirect.com/science/article/pii/S0022311522003221?via%3Dihub (cit. on p. 90).

Acknowledgements

I would like to express my deepest gratitude to Giulia for introducing me to this project opportunity, for allowing me to discover the stimulating environment of a startup, and for guiding me with patience and commitment towards all our goals. During these months, Giulia has been a reference point for me, always available to give me valuable advice.

I would like to thank the entire Thorizon team for welcoming me and giving me countless memories of such an incredible experience.

I would like to thank my supervisor, Prof. Sandra Dulla, first of all because, thanks to her inspiring lessons, I discovered my passion for the subject, and in addition for supporting my choice for this thesis.

Special thanks go to Marta for always being there when I needed her, even when I didn't deserve it and when distance was not on our side. I want to thank you, Marta, for your love and trust in me. I think it is mainly due to you that I never gave up in the face of difficulties and was able to achieve this goal.

I would like to express my sincere gratitude to my family for their continued support. I am immensely grateful to my parents for their unconditional support in every choice I made and for all their sacrifices, which I cannot repay. They are the ones who made my studies possible and have always been the ones who push me to improve every day.

Finally, I would like to thank all my friends, especially Cristian and Davide, for all their advice, experiences, and laughter shared over the years. I consider myself lucky to have friends like them, whom I know I can always count on in times of need.

Voglio esprimere la mia più profonda gratitudine a Giulia, per avermi presentato questa opportunità di progetto, per avermi fatto scoprire l'ambiente stimolante di una startup, e per avermi guidato con pazienza e impegno verso tutti i nostri obiettivi. Durante questi mesi, Giulia è stata per me una figura di riferimento fondamentale, sempre disponibile a darmi preziosi consigli.

Ringrazio tutto il team di Thorizon, per avermi accolto e fatto regalo di innumerevoli ricordi di una esperienza così incredibile.

Voglio ringraziare la mia relatrice, la Prof.ssa Sandra Dulla, innanzitutto perché grazie alle sue lezioni ispiranti ho scoperto la mia passione per la materia, e inoltre per aver appoggiato la mia scelta di tesi.

Un ringraziamento speciale va a Marta per esserci stata sempre quando ne avevo bisogno, anche quando non lo meritavo e quando la distanza non era dalla nostra parte. Ti voglio dire grazie Marta per l'amore e la fiducia nei miei confronti, penso sia soprattutto grazie a te che io non abbia mai ceduto di fronte alle difficoltà e che abbia saputo raggiungere questo traguardo.

Desidero ringraziare vivamente la mia famiglia per il continuo supporto. Sono immensamente grato ai miei genitori per il loro sostegno incondizionato in ogni mia scelta fatta e per tutti i loro sacrifici che non potrò mai ripagare. Sono loro ad aver reso possibile i miei studi e sono da sempre le figure che mi spingono a migliorare ogni giorno.

Infine voglio ringraziare tutti i miei amici, in particolare Cristian e Davide, per ogni consiglio, esperienza e risata condivisa in questi anni. Mi ritengo davvero fortunato ad avere amici del genere, sui quali so di poter sempre contare in caso di necessità.